# Site U1575[1]

W. Sager, K. Hoernle, T.W. Höfig, A.J. Avery, R. Bhutani, D.M. Buchs, C.A. Carvallo, C. Class, Y. Dai, G. Dalla Valle, A.V. Del Gaudio, S. Fielding, K.M. Gaastra, S. Han, S. Homrighausen, Y. Kubota, C.-F. Li, W.R. Nelson, E. Petrou, K.E. Potter, S. Pujatti, J. Scholpp, J.W. Shervais, S. Thoram, S.M. Tikoo-Schantz, M. Tshiningayamwe, X.-J. Wang, and M. Widdowson[2]

Contents

Keywords

Core descriptions

Supplementary material

References (RIS)

1. Background and objectives

The strategy for International Ocean Discovery Program (IODP) Expedition 391 (Walvis Ridge Hotspot) was to drill at three general locations on Walvis Ridge and one in Guyot Province, providing an age transect along the Tristan-Gough-Walvis (TGW) hotspot track. Site U1575 (proposed Site FR-1B), located on the lower Walvis Ridge between Valdivia Bank and Frio Ridge (Figure **F1**), is the easternmost and presumably the oldest site. Both hotspot models and the age progression of Homrighausen et al. (2019) predict an age of ~100 Ma (Figures **F2**, **F3**). Site U1575 is thus an important sample of the early TGW track shortly after it transitioned from the continental flood basalt to the submarine hotspot track setting.
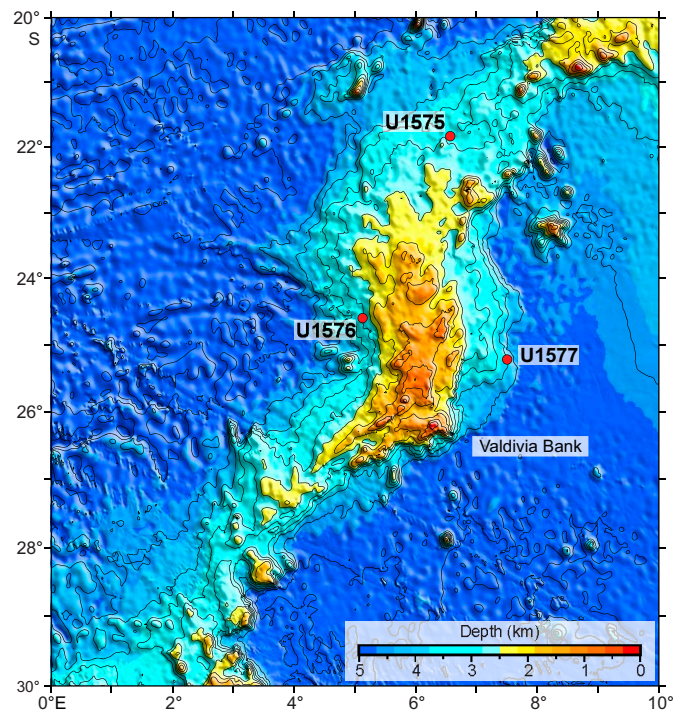
Figure F1. Bathymetry map of Valdivia Bank, showing the location of Sites U1575–U1577. Bathymetry data are from the satellite-altimetry based SRTM15+ predicted depth grid (Tozer et al., 2019). Contour interval = 500 m.

1.1. Operational strategy

Planning for Expedition 391 included using only the rotary core barrel (RCB) bit for all holes to save time. Unfortunately, this choice meant that soft-sediment cores underwent significant drilling disturbance. Site U1575 was originally planned as a two-bit hole, meaning that after the first bit had undergone ~40–50 h of basement drilling, it would be replaced with a new bit and drilling
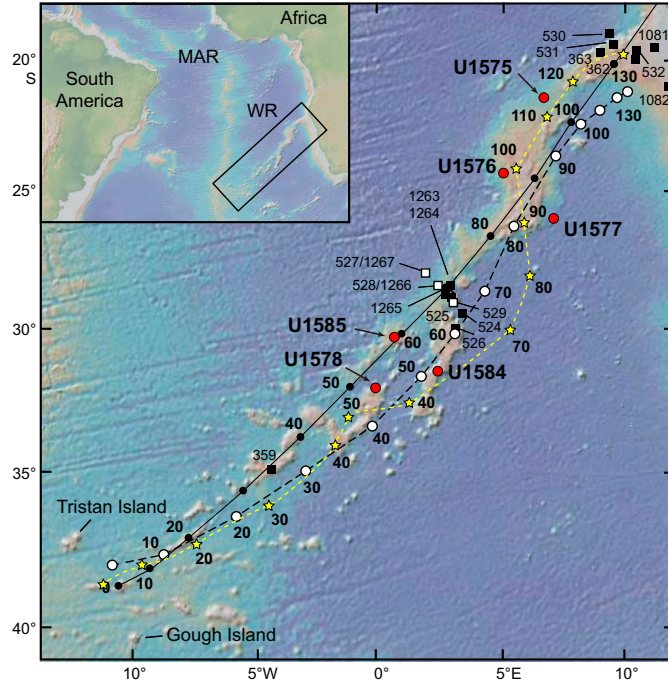
Figure F2. Walvis Ridge bathymetry (Smith and Sandwell, 1997), fixed hotspot age models, previous DSDP and Ocean Drilling Program (ODP) drill sites (squares), and Expedition 391 proposed sites and drilled sit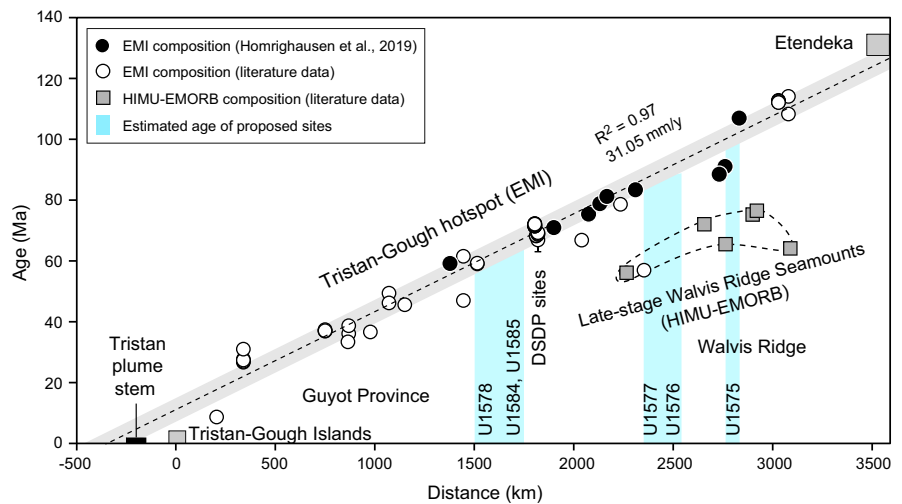es (red dots). Solid line = central plume track of the O'Connor and Le Roex (1992) hotspot model with dots every 10 Ma. Dashed line = Torsvik et al. (2008) fixed hotspot model with dots every 10 Ma. Yellow dashed line and yellow stars = moving hotspot model of Doubrovine et al. (2012). Small bold numbers = ages in Ma. MAR = Mid-Atlantic Ridge, WR = Walvis Ridge.

Figure F3. Walvis Ridge age progression from radiometrically dated igneous rocks. Samples with EMI-type composition follow a tight linear trend. Most exceptions are samples with HIMU-type composition that yield ages ~30–40 My younger than the underlying basement with an EMI-type geochemical composition. Expedition 391 sites have estimated ages of 55–65 (Site U1578), 80–85 (Sites U1576 and U1577), and 100–105 Ma (Site U1575) (see Homrighausen et al., 2019, for sources of age data).

would continue. Owing to the loss of time caused by the late start, the Expedition 391 operational plan was truncated. Site U1575 was reduced to a single-bit hole, and logging plans were dropped.

1.2. Objectives

1.2.1. Geochemical objectives

Site U1575 has the potential to provide important constraints on the geochemical evolution of TGW track volcanism. Beginning at Deep Sea Drilling Project (DSDP) Leg 74 Sites 527, 528, and 525A and going to the Tristan and Gough Islands, the track volcanism shows geochemical zonation with enriched mantle one (EMI)-type compositions that can be divided into Tristan-type (low $^{207}Pb/^{204}Pb$ for a given $^{206}Pb/^{204}Pb$) and Gough-type (high $^{207}Pb/^{204}Pb$ for a given $^{206}Pb/^{204}Pb$) compositions (Rohde et al., 2013; Hoernle et al., 2015). Dredge samples from Walvis Ridge north of the DSDP sites are dominated by the Gough-type geochemical composition (Hoernle et al., 2015). Nevertheless, a sample from the eastern side of Valdivia Bank, near Site U1575, has Tristan-type composition (Homrighausen et al., 2019). Is this an anomaly? Or are Tristan-type compositions mixed with Gough-type compositions but poorly represented by dredge sampling? Could there be an age difference between the two types, such as Gough type overlying Tristan type, thus requiring drilling to detect the Tristan type?

Another important question concerns the presence of two distinct flavors of the Gough type in the Etendeka flood basalts in northwest Namibia, which are believed to represent lavas from the starting plume head of the TGW hotspot (Zhou et al., 2020). The Gough-type basalts on Walvis Ridge are characterized by high-Ti contents. High-Ti basalts also dominate in northern Etendeka, where Walvis Ridge connects to the African continental margin (e.g., Zhou et al., 2020). On the other hand, low-Ti Gough-type basalts dominate in southern Etendeka. The low-Ti Gough type is also common in the Paraná flood basalts in South America, which formed contemporaneously with the Etendeka flood basalts before the continents separated. This component, however, has not been found on Walvis Ridge thus far. This discrepancy may be due to the limited number of samples available from the northeastern part of Walvis Ridge.

In conclusion, Site U1575 provides the best sampling thus far of the poorly sampled northeastern part of Walvis Ridge, allowing us to evaluate whether the aforementioned geochemical components are present.

1.2.2. Geochronologic objectives

Because Site U1575 is located on a lower part of Walvis Ridge with no exposed basement outcrops, it represents a portion of the ridge that is unsampled by dredging. Ages from elsewhere on the eastern part of Walvis Ridge are younger than expected, owing to capping of the ridge by seamounts constructed by late-stage high μ (HIMU)–type eruptions (Homrighausen et al., 2018, 2020). Reliable ages from older basement will help in defining and understanding the contribution of different eruption stages to the TGW age progression. To this end, geochronologic studies will seek to determine reliable ages for igneous rocks cored at Site U1575.

1.2.3. Paleomagnetic objectives

According to global paleomagnetic data, Site U1575 samples the TGW track at a time when the paleolatitude was ~6°–8° farther north than the present hotspot latitude band (Figure **F4**). This is a period of rapid paleolatitude change for the African plate, during which the paleolatitudes shifted from ~15° farther north than at present around the time of Etendeka emplacement (Ernesto et al., 1990, 1999) to ~5° south than at present around 50–60 Ma. Thus, samples from Site U1575 can provide important constraints on the rapidly shifting Late Cretaceous paleolatitude. Mantle flow models indicate that the TGW hotspot moved ~8° south (Doubrovine et al., 2012) since ~100 Ma, but it is unclear how reliable these models are. Paleomagnetic studies of basal sedimentary rock and igneous rock will be used to determine paleolatitudes that will help unravel the contributions of hotspot drift, plate motion, and true polar wander.

1.2.4. Volcanologic objectives

Site U1575 is located on a low part of Walvis Ridge between the more voluminous Frio Ridge and Valdivia Bank. It may thus represent a period of low TGW volcanic output or greater distance from the mid-Atlantic spreading center at the time of formation. Was volcanism during this period fundamentally different than at Valdivia Bank or other high-effusion parts of the ridge? Cores from Site U1575 have the potential to illustrate the style of volcanism on the TGW track to determine whether the volcanologic aspects are different compared to areas where the ridge reaches shallower depths. Studies of igneous rock types will seek to understand the volcanic development of this low spot on Walvis Ridge.
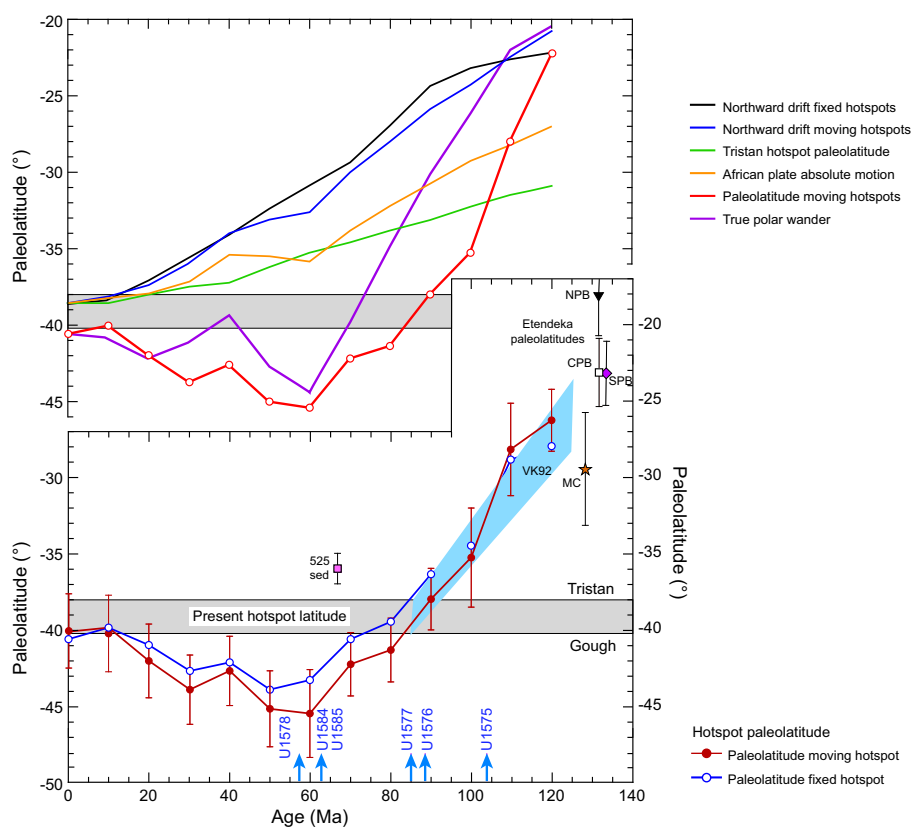
Figure F4. Predicted paleolatitude drift of the TGW hotspot, hotspot models, and true polar wander. Expedition 391 sites are shown. Bottom: paleolatitude estimates. Red line with filled red dots = estimated paleolatitudes calculated from the global average African plate apparent polar wander path (Torsvik et al., 2008) based on a plate motion model with moving hotspots (Doubrovine et al., 2012). Thin vertical lines = 95% confidence limits based on paleomagnetic data scatter only. This polar wander path was constructed with a 20 My window length averaged every 10 Ma. Blue line with open blue circles = same paleolatitude curve for a fixed hotspot model (Torsvik et al., 2008). Pink square = paleolatitude determined for 60–75 Ma sediments from Site 525 (Chave, 1984). Its departure from the paleolatitude curve may be a result of inclination shallowing that is common for sediments (Verosub, 1977). Inverted black triangle (NPB), open square (CPB), and purple diamond (SPB) = paleolatitudes from the north, central, and south Paraná flood basalts (Ernesto et al., 1990, 1999), respectively. Red star (MC) = paleolatitude of Messum Gabbros (MC) in the Etendeka province (Renne et al., 2002). Blue band (VK92) = hotspot drift estimated by Van Fossen and Kent (1992). Blue arrows = estimated ages of proposed drill sites from an age progression model (Homrighausen et al., 2019, 2020). Top: northward drift and true polar wander. Red line with open circles = paleolatitudes estimated from paleomagnetic data (same as lower plot). Black line = northward drift of a seamount over time if formed at the Tristan hotspot location, assuming fixed hotspot model (Torsvik et al., 2008). Blue line = same as black line but for a moving hotspot model (Doubrovine et al., 2012). Green line = paleolatitudes of the Tristan hotspot from a mantle flow model (Doubrovine et al., 2012), indicating ~7° southward motion in 120 Ma. Orange line = northward drift of the African plate in the moving hotspot model (Doubrovine et al., 2012). It is less than the fixed hotspot model because the Tristan hotspot is modeled as moving south. Adding the hotspot motion to the moving hotspot model absolute motion equals the total northward motion indicated by the morphology of the TGW chain and the fixed hotspot model. All absolute motion models indicate that the African plate moved nearly monotonically northward, so they do not explain the rapid southward shift in paleolatitudes during the Late Cretaceous or the northward offset of paleolatitudes during the early Cenozoic. The difference between modeled and observed paleolatitudes implies significant true polar wander (purple curve) (Doubrovine et al., 2012).

1.2.5. Sedimentologic objectives

Site U1575 is at an important location for understanding the sedimentation off the west coast of southern Africa. Sedimentation rates are high near shore, with a large influx of terrigenous sediment building a thick wedge. Offshore, carbonate sediments prevail and lower sedimentation rates yield a thin drape. The thin sediment package at Site U1575 suggests it was in an area of low sedimentation rate, but it may show fluctuations in deposition. The Benguela Current runs northward off the west African coast, so Site U1575 is in a position to show variations in the position and strength of this current. Although Site U1575 is west of the main Benguela Current (e.g., Summerhayes et al., 1995), it may still show temporal changes of the location of this current. As environmental conditions change, the site could alternately find itself affected by the Benguela Current or by waters of the gyre interior. Layering in the seismic section and in the recovered cores suggests that coring through the Site U1575 sediment column offers clues to shifting conditions offshore of Namibia since the Cretaceous. Biostratigraphic and sedimentologic studies will focus on reconstructing the sedimentary history.

1.3. Site geophysics

Site U1575 is located on Walvis Ridge between Valdivia Bank and Frio Ridge at a water depth of 3233 m (Figure **F1**). The drill site was picked on Seismic Line GeoB01-25, collected in 2001 by the research vessel (R/V) *Meteor*. In 2019, a second seismic line (TN373-VB13), collected by the R/V *Thomas G. Thompson*, was shot crossing the site at nearly right angles to the previous line (Figure **F5**). Bathymetric data show that the site is in a swale between low rises to the southwest and northeast. The area of the site itself is relatively flat. Ridge-like features south of the drill site have the appearance of sedimentary erosional remnants, suggesting that downslope sediment movement and erosion may have affected the area.

The GeoB01-25 profile shows a relatively thin sediment layer, ~171 m thick, overlying a strong and undulating basement horizon (Figure **F6**). Sediment thickness increases to the northeast and southwest, showing that the hills are thicker piles of sediments and implying laterally differential sedimentation and/or erosion. Seismic Line GeoB01-25 shows reflectors at ~50 and 110 ms below the seafloor, implying unit boundaries at ~40 and 88 meters below seafloor (mbsf) (assuming seismic velocity = 1600 m/s). On the GeoB01-25 profile, a reverberant layer is seen near basement, implying a different basal sedimentary layer. Line TN373-VB13 indicates three horizons dividing
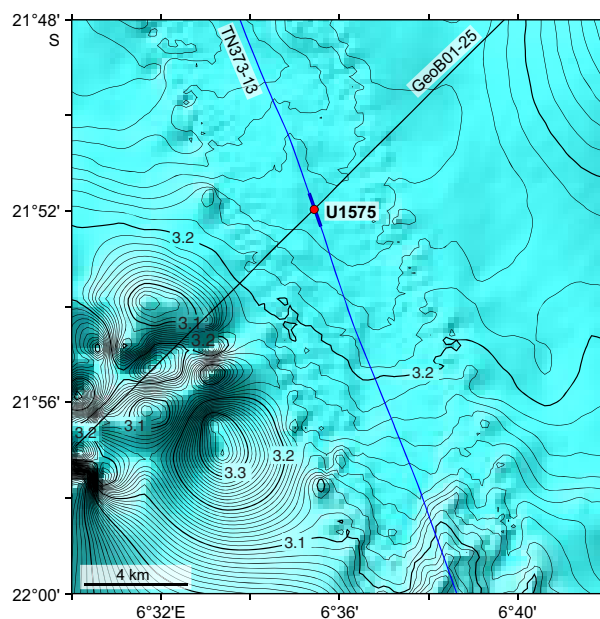
Figure F5. Bathymetry map, Site U1575. Detailed multibeam bathymetry around Seismic Line TN373-13 is merged with the SRTM15+ bathymetry grid (Tozer et al., 2019). Contours are plotted at 10 m intervals and are labeled in kilometers. Black line = Seismic Line GeoB01-25, blue line = Seismic Line TN373-13. Heavy blue line = portion of the line shown in Figure F7.
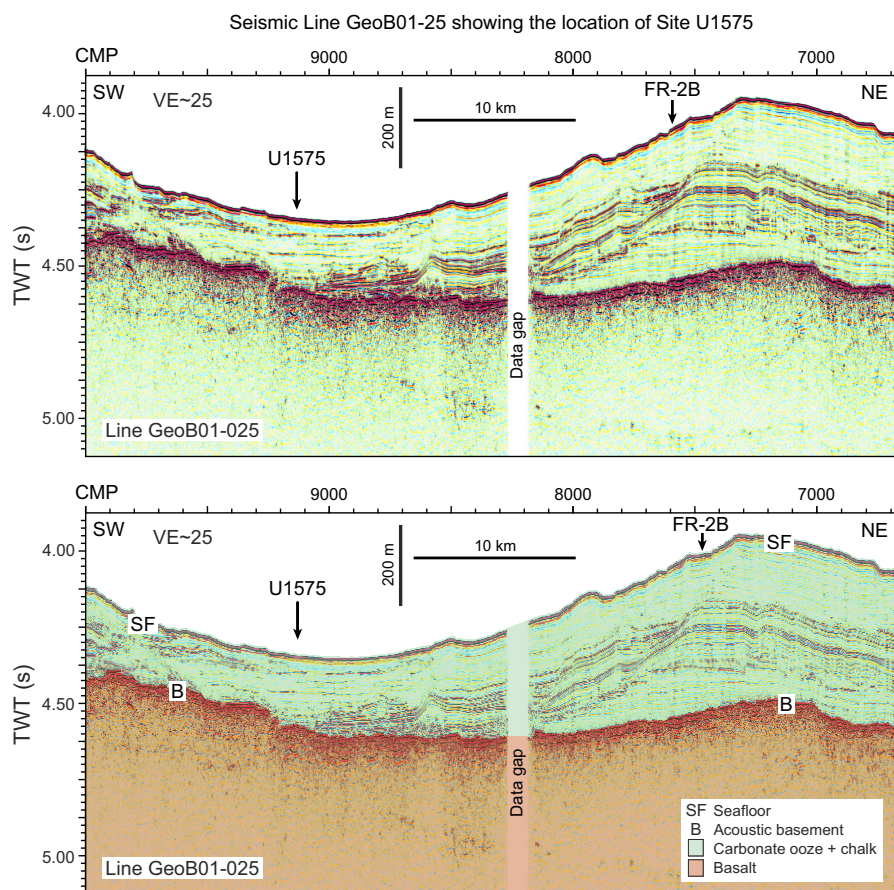
Figure F6. Portion of Seismic Line GeoB01-25. Top: uninterpreted data. Bottom: interpretation. TWT = two-way traveltime, CMP = common midpoint, VE = vertical exaggeration.

the section into four layers (Figure **F7**). Horizons R1 and R2 appear to correlate with the two horizons noted in the GeoB01-25 profile, whereas Horizon R3 appears to be the basal sediment layer noted on the GeoB01-25 profile. This layering suggests that the sedimentary history took place over at least four different periods.

Basement on the TN373-VB13 profile (Figure **F7**) is interpreted to be igneous rock at the top of Walvis Ridge basement. This surface is undulatory, as is expected for a lava flow surface. Vertical offsets on Line GeoB01-25 imply normal faults, but at distances >2 km from the site (Figure **F6**). The seismic source for the TN373-VB13 profile was small and does not penetrate deeply into basement, but it apparently shows 2–3 semicontinuous reflectors in the upper ~50 ms (~100 m assuming velocity = 4000 m/s). These reflections likely indicate lava flow packages (Inoue et al., 2018; Sager et al., 2013).
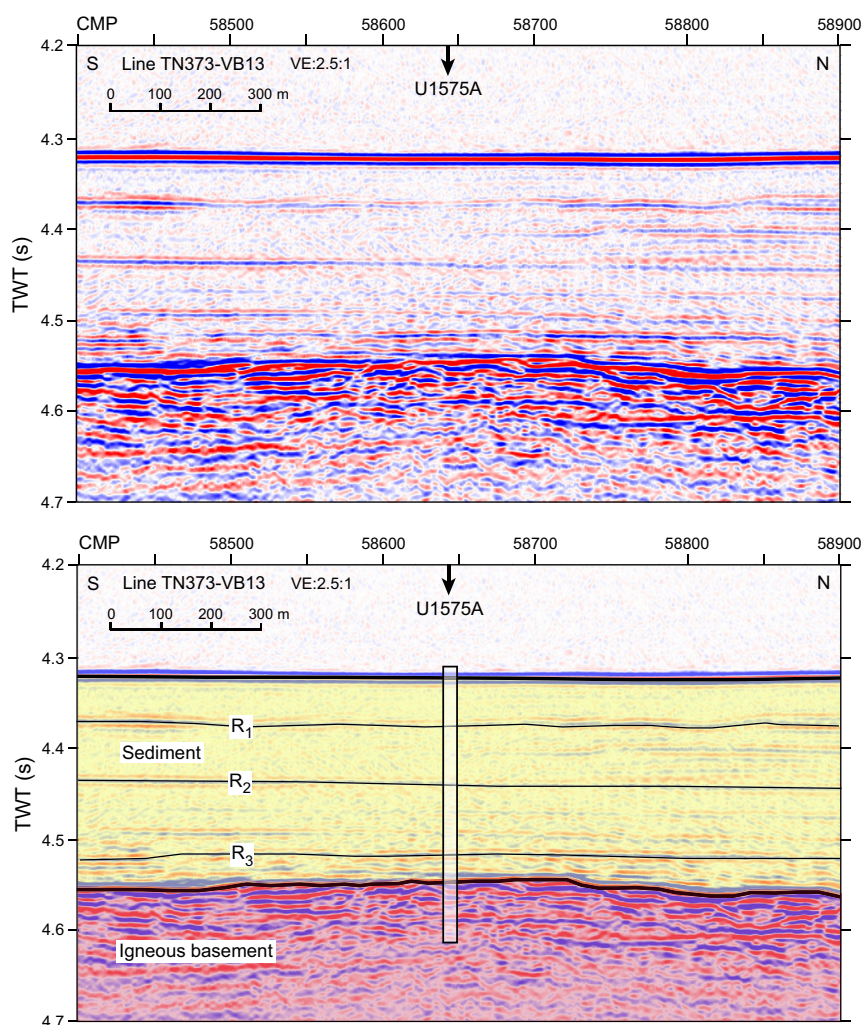
Figure F7. Seismic Line TN373-VB13. Top: uninterpreted section. Bottom: interpretation. Vertical column shows approximate cored section. TWT = two-way traveltime, CMP = common midpoint, VE = vertical exaggeration. R₁, R₂, R₃ = seismic reflectors.

2. Operations

2.1. Cape Town port call

Expedition 391 officially began at 0800 h (UTC + 2 h) on 6 December 2021. The R/V *JOIDES Resolution* had just completed IODP Expedition 396T, a transit and subsequent tie-up period at Repair Quay 3 in the port of Cape Town, South Africa. On the first day of the port call, incoming IODP *JOIDES Resolution* Science Operator (JRSO) air freight was loaded on board, including a new 50 kVA uninterruptible power supply unit. All oncoming Expedition 391 personnel, including a reduced JRSO technical staff and science party contingent, arrived in Cape Town 5 days prior to the official start of the expedition to complete a 7 day quarantine period in a local hotel as part of the COVID Mitigation Protocols Established for Safe JR Operations (COPE). On 7 December, six pallets of food stores were loaded and shipboard antigen/polymerase chain reaction (PCR) Coronavirus Disease 2019 (COVID-19) testing was performed on offgoing personnel. After clearing immigration on 8 December, the Siem Offshore staff, JRSO technical staff, and science party boarded the vessel following the 7 day quarantine period. There were no positive COVID-19 cases detected from either of the two tests administered during the quarantine period. On 9 December, the crew loaded frozen and dry catering stores and the ship bunkered 500.2 mt of fuel. A second barge load of 508.3 mt of fuel was bunkered on 10 December. Other port call activities that day

included loading four flats containing a mud motor, casing, knobby drilling joints, and core liner and loading a shipment of fresh fruits and vegetables.

After a late urgent air freight shipment required by Siem Offshore was delivered at 1310 h on 11 December, the vessel was secured for transit. In anticipation of this late shipment delivery, a passage plan and arrangements made with the port agent, tugboats, and harbor pilot slated the ship for departure at 1400 h. However, just prior to the scheduled departure, the captain was notified that because of early morning fog and the resulting backlog of other ships waiting to depart, the departure would be delayed. The pilot came on board at 1642 h. Two harbor tugboats arrived, and the mooring lines were released and pulled back on board. The last line was released from Repair Quay 3 at 1709 h. The vessel proceeded to the pilot station, and the pilot departed the vessel at 1738 h after a 5 nmi transit. The vessel began its sea passage at 1800 h on 11 December 2021.

2.2. Transit to proposed Site CT-04A

After the 973 nmi transit from Cape Town, South Africa, averaging 11.1 kt, the vessel arrived at proposed Site CT-04A at 0818 h on 15 December 2021. The thrusters were lowered at 0822 h, and the vessel was switched to full dynamic positioning (DP) mode at 0845 h. The rig floor was then cleared for operations.

2.3. Proposed Site CT-04A

The drilling crew started assembling the RCB bottom-hole assembly (BHA) by making up the outer core barrel. Components on the inner core barrels were inspected and replaced, and both core barrels were spaced out in the outer core barrel. At 1215 h on 15 December 2021, the captain informed the rig floor that operations were being suspended because of an emergent medical issue. During the last day of sea passage to proposed Site CT-04A, suspected cases of COVID-19 were identified among the ship's crew. With several personnel isolated, which limited our ability to continue operations, the decision was made to return to Cape Town. We then rigged down, the core barrels were secured, and the components of the outer core barrel were laid out and secured. All staged drill collars were moved back to the drill collar racks. At 1300 h, the drill floor was secured for transit. In the meantime, the engine department had started the replacement of one of the propulsion motor cooling fans. This was completed at 1445 h. The thrusters were raised and secured, and the switch from DP to cruise mode was implemented.

2.4. Return to Cape Town

The vessel was underway to Cape Town, South Africa, at 1506 h on 15 December 2021. Antigen testing for COVID-19 continued during the transit, and by 2400 h on 18 December, there were several additional cases recorded among the crew, requiring us to make shore-based isolation arrangements to limit the spread of the virus on board. None of the scientists or JRSO personnel tested positive during the transit. Upon completing the 977 nmi sea passage to Cape Town, averaging 8.8 kt, the vessel arrived at an anchorage location outside of Cape Town harbor at 0649 h on 20 December. The anchor was dropped at 0650 h. The personnel who had tested positive for COVID-19 through rapid (antigen) testing disembarked by water taxis and were taken to a Cape Town hotel for isolation. The harbor pilot boarded the vessel at 1114 h, and the anchor was raised and off bottom at 1120 h. Directed by the harbor pilot, the vessel proceeded to Landing Wharf 2. Two harbor tugboats joined the vessel at 1142 h and assisted in its mooring. The first line ashore was at 1224 h, ending the 1.75 nmi pilotage passage from the anchorage to the berth site. All lines were secured by 1307 h, and the pilot departed the vessel.

PCR testing for all remaining shipboard personnel was performed shortly after arrival. Personnel who were close contacts of those who tested positive disembarked from the vessel and were transferred to a hotel to quarantine. An additional positive test was recorded from the first round of shipboard PCR testing. On 21 December, antigen testing continued for crew members who were close associates of the infected personnel, revealing another positive test. These additional infected crew members disembarked and went to a hotel to isolate. On 22 December, antigen testing continued for close contacts with the crew. Another positive test was recorded, and the individual was transferred to isolation in a hotel. A protocol of alternating daily PCR and antigen

testing was established for all shipboard personnel, starting with a round of PCR testing on 22 December that returned only negative results. On 23 December, another complete round of antigen testing was performed, and no positive results were recorded. On 24 December, the first two crew members returned to the ship from hotel isolation. Another round of PCR testing was completed for all vessel personnel. No positive tests were recorded from continued close contact antigen testing. However, one crew member who tested negative was isolated on board with a suspected COVID-19-related symptom. On 25 December, the results from the previous day's PCR testing were received and antigen tests were performed on all personnel aboard the ship. The symptomatic crew member isolated on board was confirmed as a positive COVID-19 case by not only the PCR testing but also the antigen test administered, representing the only positive result on that day. The infected person departed the ship to isolate in a hotel. On 26 December, PCR tests were administered for all personnel on the vessel, and all results were negative. One crew member returned to the ship upon completion of the hotel isolation period. On 27 December, an additional 16 crew members returned after their isolation period was completed. All 16 individuals tested negative for COVID-19 prior to their return. Antigen testing was performed on all vessel personnel, yielding solely negative results. On 28 December, PCR tests were administered for all personnel on the vessel. Three personnel returned to the ship upon completion of their hotel isolation period. Surface freight was loaded, consisting of laboratory supplies. Pending COVID-19 testing results, the ship was scheduled to depart Cape Town the following day.

On 29 December, antigen tests were administered for all personnel on the vessel and results from the previous PCR testing were received. All tests were negative for COVID-19, initiating the preparation for departure. Three personnel returned to the ship upon completion of their hotel isolation period. Also, fresh fruit and vegetables were loaded on board. The ship was secured for transit, and the harbor pilot came aboard at 1301 h. Two harbor tugboats were made fast by 1318 h, and the vessel departed Landing Wharf 2 with the last line released at 1330 h, proceeding to the pilot station. The pilot disembarked at 1354 h, and our sea passage to Site U1575 started at 1400 h on 29 December. During the transit, antigen testing was implemented for all vessel personnel daily, and all results were negative.

2.5. Transit to Site U1575

After the 967 nmi transit from Cape Town, South Africa, averaging 12.2 kt, the vessel arrived at Site U1575 at 2100 h (UTC + 2 h) on 1 January 2022. The thrusters were lowered and secured, and at 2140 h, the drill floor was cleared for operations, beginning Hole U1575A.

2.6. Site U1575

Site U1575 consists of a single hole to 332.3 mbsf. The original plan called for a two-bit hole. The total planned depth for the hole was determined by the desire to core through ~250 m of basement. The plan was changed after our operating time was cut short by the COVID-19 outbreak earlier in the expedition. Both logging and our free-fall funnel reentry system were dropped from the plan. Instead, Hole U1575A was a single-bit hole drilled to bit destruction or until available time for the site expired. Hole U1575A was cored to 332.3 mbsf. A total of 41 cores were recorded for the site. The RCB coring system was used exclusively. It cored 332.3 m and recovered 185.15 m of sediment and igneous rock (average = 55.7%).

2.6.1. Hole U1575A

Cleared for operations at 2140 h on 1 January 2022, the rig crew began to make up the RCB BHA, and by 2400 h, the 172.1 m long BHA was assembled with the C-4 RCB bit. A mechanical bit release was installed above the bit during our extended stay in Cape Town prior to the cancellation of logging. A precision depth recorder (PDR) for the site indicated an estimated water depth of 3242.4 meters below rig floor (mbrf). The rig crew lowered the drill string, attaching the circulating head to the top of the drill string and filling the drill pipe with surface seawater after 50 stands of pipe (each stand measures ~28.5 m). The stands of 5 inch drill pipe were drifted and measured while lowering the drill string to just above the seafloor. At 0745 h on 2 January, the top drive was picked up, and circulation through the drill pipe was established when the drill bit reached 3193.9 meters below sea level (mbsl). We then pumped a "pig" (pipe cleaning device) through the drill

string to remove some of the rust. The drill bit was lowered farther and positioned at the seafloor depth of 3231.3 mbsl, as obtained from the PDR, to spud Hole U1575A. A dressed nonmagnetic RCB core barrel was dropped and pumped down to land in the outer core barrel.

Hole U1575A was spudded at 1015 h on 2 January, and RCB coring began. The PDR water depth appeared to match the driller's tag depth and was used for the official water depth for Hole U1575A. Cores 1R–41R penetrated from the seafloor to a final depth of 332.3 mbsf and recovered 185.2 m (56%) of sediment and igneous rock. The sediment/igneous basement contact was intersected on 3 January while cutting Core 22R at 209.9 mbsf when the drilling rate slowed from ~5 to ~1.25 m/h. We switched to half-length (~4.8 m) advances on Cores 23R–34R because of the slow penetration rate and to improve core recovery. In an attempt to increase the final depth in Hole U1575A, full coring resumed with Core 35R. This approach continued through Core 36R. On Core 37R, the penetration rate again dropped to 0.6 m/h. After almost 6.5 h of cutting Core 37R and with only a 4 m advance, the core barrel was pulled for inspection. The core recovery was exceptional, but the core catchers were damaged and barely managed to prevent the core from dropping out of the core barrel. While cutting the remaining 5.7 m to complete a full advance on Core 38R, the penetration rate increased to the point where full coring was possible again. Thus, the final three cores (39R–41R) were full-advance cores to a final depth of 332.3 mbsf. In total, 220 bbl (34,977 L) of high-viscosity mud were pumped in 20 bbl (3,180 L) sweeps for hole cleaning over the course of coring Hole U1575A. Coring was terminated in Hole U1575A following Core 41R, which was on deck at 0625 h on 7 January. The RCB core barrels were secured, and we started pulling the drill string out of the hole at 0700 h. The top drive was set back at 0745 h, the bit cleared the seafloor at 0842 h, and the top of the BHA reached the rig floor at 1300 h. The four stands of drill collars were racked back in the derrick, and the outer core barrel components were disassembled, inspected, and laid out. The bit arrived at the rig floor at 1430 h on 7 January, ending Hole U1575A. The rig floor was secured for transit at 1445 h, ending Site U1575. The time spent on Hole U1575A was 137.0 h, or 5.7 days (Table **T1**).

Table T1. Core summary, Site U1575. UTC = Coordinated Universal Time, DRF = drilling depth below rig floor, DSF = drilling depth below seafloor, CSF = core depth below seafloor, PDR = precision depth recorder. R = rotary core barrel (RCB). N-Mag = nonmagnetic core barrel. (Continued on next page.) **Download table in CSV format.**

Hole U1575A
Latitude: 21°51.9659′S
Longitude: 6°35.4369′E
Water depth (m): 3231.31
Date started (UTC): 1 January 2022; 1940 h
Date finished (UTC): 7 January 2022; 1245 h
Time on hole (days): 5.71
Seafloor depth DRF (m): 3242.4
Seafloor depth est. method: PDR
Rig floor to sea level (m): 11.09
Penetration DSF (m): 332.3
Cored interval (m): 332.3
Recovered length (m): 185.15
Recovery (%): 55.72
Drilled interval (m): 0
Drilled interval (*N*): 0
Total cores (*N*): 41

Core, type	Date (2022)	Time on deck UTC (h)	Top depth drilled DSF (m)	Bottom depth drilled DSF (m)	Advanced (m)	Recovered length (m)	Curated length (m)	Top depth cored CSF (m)	Bottom depth recovered (m)	Recovery (%)	Sections (*N*)	Comment
391-U1575A-												
1R	2 Jan	0855	0.0	9.5	9.5	9.50	9.50	0.0	9.50	100	8	N-Mag
2R	2 Jan	1015	9.5	19.0	9.5	9.50	9.60	9.5	19.10	100	8	N-Mag
3R	2 Jan	1115	19.0	28.7	9.7	9.61	9.61	19.0	28.61	99	8	N-Mag
4R	2 Jan	1205	28.7	38.3	9.6	4.75	4.75	28.7	33.45	49	5	N-Mag
5R	2 Jan	1300	38.3	47.9	9.6	8.71	8.71	38.3	47.01	91	7	N-Mag
6R	2 Jan	1345	47.9	57.6	9.7	2.78	2.78	47.9	50.68	29	3	N-Mag
7R	2 Jan	1435	57.6	67.3	9.7	4.92	4.92	57.6	62.52	51	5	N-Mag
8R	2 Jan	1525	67.3	77.1	9.8	5.91	5.91	67.3	73.21	60	5	N-Mag
9R	2 Jan	1620	77.1	86.9	9.8	7.27	7.27	77.1	84.37	74	6	N-Mag
10R	2 Jan	1710	86.9	96.6	9.7	8.24	8.24	86.9	95.14	85	7	N-Mag

Table T1 (continued).

Core, type	Date (2022)	Time on deck UTC (h)	Top depth drilled DSF (m)	Bottom depth drilled DSF (m)	Advanced (m)	Recovered length (m)	Curated length (m)	Top depth cored CSF (m)	Bottom depth recovered (m)	Recovery (%)	Sections (*N*)	Comment
11R	2 Jan	1755	96.6	106.4	9.8	4.63	4.63	96.6	101.23	47	4	N-Mag
12R	2 Jan	1900	106.4	116.2	9.8	4.27	4.27	106.4	110.67	44	4	N-Mag
13R	2 Jan	1950	116.2	126.0	9.8	6.39	6.39	116.2	122.59	65	6	N-Mag
14R	2 Jan	2040	126.0	135.7	9.7	3.35	3.35	126.0	129.35	35	4	N-Mag
15R	2 Jan	2125	135.7	145.4	9.7	3.82	3.82	135.7	139.52	39	4	N-Mag
16R	2 Jan	2225	145.4	155.2	9.8	3.09	3.09	145.4	148.49	32	3	N-Mag
17R	2 Jan	2315	155.2	164.9	9.7	1.84	1.84	155.2	157.04	19	3	N-Mag
18R	3 Jan	0005	164.9	174.6	9.7	1.00	1.00	164.9	165.9	10	2	N-Mag
19R	3 Jan	0055	174.6	184.3	9.7	0.40	0.40	174.6	175.00	4	2	N-Mag
20R	3 Jan	0140	184.3	194.1	9.8	2.84	2.84	184.3	187.14	29	3	N-Mag
21R	3 Jan	0245	194.1	203.8	9.7	4.57	4.57	194.1	198.67	47	4	N-Mag
22R	3 Jan	0515	203.8	213.5	9.7	7.09	7.43	203.8	211.23	73	6	N-Mag
23R	3 Jan	1005	213.5	217.7	4.2	4.30	4.89	213.5	218.39	102	4	N-Mag
24R	3 Jan	1555	217.7	223.3	5.6	3.16	4.18	217.7	221.88	56	3	N-Mag
25R	3 Jan	2215	223.3	229.0	5.7	5.70	6.17	223.3	229.47	100	5	N-Mag
26R	4 Jan	0720	229.0	235.0	6.0	5.17	5.49	229.0	234.49	86	5	N-Mag
27R	4 Jan	1045	235.0	239.7	4.7	2.59	2.95	235.0	237.95	55	2	N-Mag
28R	4 Jan	1415	239.7	244.7	5.0	2.75	3.36	239.7	243.06	55	3	N-Mag
29R	4 Jan	1725	244.7	249.5	4.8	3.02	3.19	244.7	247.89	63	3	N-Mag
30R	4 Jan	2245	249.5	254.5	5.0	2.57	2.69	249.5	252.19	51	3	N-Mag
31R	5 Jan	0415	254.5	259.2	4.7	3.45	4.02	254.5	258.52	73	3	N-Mag
32R	5 Jan	0815	259.2	264.2	5.0	2.68	3.11	259.2	262.31	54	3	N-Mag
33R	5 Jan	1140	264.2	268.9	4.7	2.80	3.26	264.2	267.46	60	3	N-Mag
34R	5 Jan	1415	268.9	273.9	5.0	1.52	1.52	268.9	270.42	30	2	N-Mag
35R	5 Jan	2030	273.9	283.7	9.8	5.81	6.87	273.9	280.77	59	5	N-Mag
36R	6 Jan	0350	283.7	293.4	9.7	4.16	5.51	283.7	289.21	43	4	N-Mag
37R	6 Jan	1125	293.4	297.4	4.0	5.07	5.18	293.4	298.58	127	4	N-Mag
38R	6 Jan	1735	297.4	303.1	5.7	4.50	4.62	297.4	302.02	79	4	N-Mag
39R	6 Jan	2245	303.1	312.9	9.8	8.21	9.26	303.1	312.36	84	7	N-Mag
40R	7 Jan	0050	312.9	322.6	9.7	1.02	1.26	312.9	314.16	11	1	N-Mag
41R	7 Jan	0425	322.6	332.3	9.7	2.19	2.92	322.6	325.52	23	2	N-Mag
		Hole U1575A totals:		332.3		185.15					173	

3. Lithostratigraphy

At Site U1575, a thick (~210 m) sedimentary cover lies on top of an igneous basement. The underlying igneous succession consists of eruptive units of varying thickness from massive (several meters) to individual pillow lavas (<1 m) and contains rare sedimentary intervals and minor infillings. Three lithostratigraphic units were recognized in the overlying sedimentary cover based on core and microscopic (smear slide and thin section) observations (Figure **F8**).

3.1. Lithostratigraphic unit descriptions

3.1.1. Unit I

Interval: 391-U1575A-1R-1, 0 cm, to 21R-1, 8 cm
Depth: 0–194.10 mbsf
Age: Pleistocene to late Miocene (Tortonian) (~0.43–9 [12.5?] Ma)

Unit I is an unlithified succession of dominantly white calcareous nannofossil-foraminifera ooze with rare to minor radiolarians (Figure **F9A**). Subtle gray and, more rarely, white-green centimeter-sized banding occurs throughout. $CaCO_3$ content measured in whole-round samples is very similar throughout the unit, ranging 90.5–97.9 wt% (median = 95.2 wt%; n = 37) (see **Sediment geochemistry**). Despite pervasive drilling disturbance due to poor compaction and lithification of the ooze, the sediment locally retains some of its internal structure in the center of the cores. Generally, deeper levels contain less water and are increasingly cohesive; however, consistency is variable even at some deeper levels. The color changes from white to pale brown in the lowermost 10 m of the unit, reflecting a minor increase in the clay content downhole. The base of Unit I is marked by an 8 cm thick semilithified white foraminifera sandstone (interval 391-

U1575A-21R, 0–8 cm), which possibly represents a winnowed lag in the ooze and yields a late Miocene age (see **Biostratigraphy**). The base of the foraminifera sandstone forms a sharp boundary with the distinctively browner and more lithified nannofossil-foraminifera chalk of Unit II. Micropaleontology reveals apparently near-continuous sedimentation throughout Unit I, spanning the Pleistocene to late Miocene, with an average sedimentation rate of approximately 20 m/My (not corrected for sediment compaction).

Diffuse banding of darker gray material results from accumulations of pyrite framboids and microcrystallites (Figure **F10**). Many bands are characterized by a downward fading of intensity over a few centimeters returning to the white uniform color of the ooze. The occurrence of pyrite framboids is typically associated with anoxic conditions during the early diagenesis of the sediment, which can be the result of productivity changes in surface waters. Accordingly, the repetitive but variable spacing of the dark bands may be related to long-term climate controls. Such controls might also explain occurrences of faint white-green bands due to changes in the relative abun-
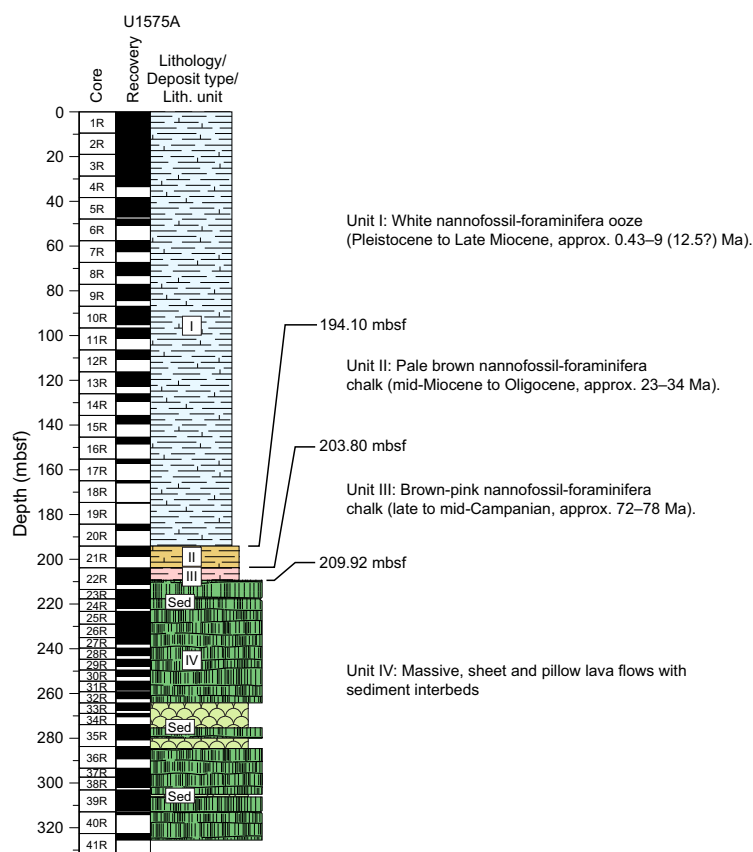
Figure F8. Lithostratigraphic summary, Site U1575.
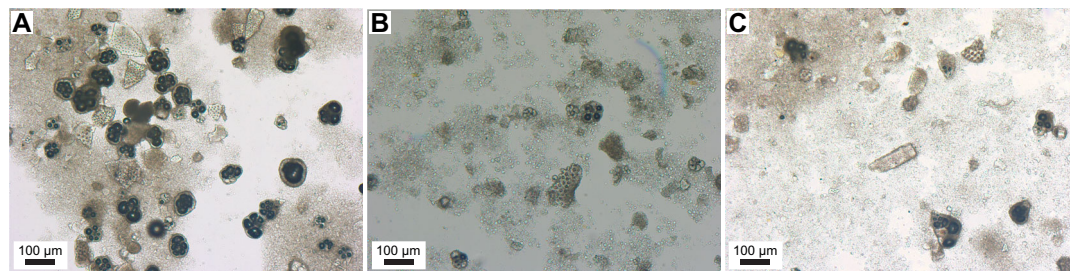
Figure F9. Nannofossil-foraminifera ooze with radiolarians in the sedimentary cover, Hole U1575A. A. Unit I (9R-4, 41 cm). B. Unit II (21R-1, 45 cm). C. Unit III with a fragment of inoceramid shell in the center (22R-4, 49 cm).

dance of calcareous (i.e., nannofossils and foraminifera) and siliceous (i.e., radiolarians) microfossils. No volcanic clasts were found in Unit I.

3.1.2. Unit II

Interval: 391-U1575A-21R-1, 8 cm, to 21R-CC, 5 cm
Depth: 194.10–203.80 mbsf
Age: mid-Miocene to Oligocene (~23–34 Ma)

Unit II is a <10 m thick sequence of poorly lithified pale brown nannofossil-foraminifera chalk with rare to minor radiolarians and clays (Figure **F9B**). One round sample (from interval 391-U1575A-21R-2, 140–150 cm) provided a $CaCO_3$ content of 85.5 wt%, which is consistent with the color change and a minor increase in clay abundance compared to Unit I (see **Sediment geochemistry**). Minor drilling disturbance in this semilithified unit results in excellent retrieval of sedimentary structures, which are outlined by white to pale brown color changes controlled by the relative abundance of nannofossils and clays at the centimeter to subcentimeter scales. The base of the unit was not recovered. However, distinct lithologic characteristics and fossil assemblages between Cores 21R and 22R unambiguously support a unit boundary between these two intervals. Microfossil assemblages suggest a mid-Miocene to Oligocene age of deposition. Determination of younger ages, which may otherwise indicate continuity to Unit I, are undefined due to limited shipboard biostratigraphic data and <50% sediment recovery in Section 21R-3 immediately above the contact with Unit II (see **Biostratigraphy**). Accordingly, the occurrence of significant depositional hiatus(es) cannot be ruled out.

Two main lithofacies were recognized in the unit.

Lithofacies 1 is composed of slightly to heavily burrowed nannofossil-foraminifera chalk, which forms approximately 80% of the unit. The lithofacies exhibits several types of ichnofossils and associated crosscutting relationships. Local infills and inliers of white nannofossil chalk are associated with burrowing (Figure **F11A, F11B**).

Lithofacies 2 is composed of laminated nannofossil-foraminifera clayey siltstone, which forms approximately 20% of the unit. This lithofacies forms 4–47 cm thick intervals that predominantly include moderately dipping planar laminae with rare cross-lamination and burrows (Figure **F11C, F11D**). The lamination is formed by changes in the relative abundance of foraminifera versus finer particles (i.e., nannofossils and clays), thus indicating local winnowing of the finer sedimentary components and reworking of the foraminifera by bottom currents.

Both lithofacies locally include black diffuse centimeter-sized patches and millimeter-sized particles of diagenetic origin (e.g., pyrite or pyrolusite). The alternation of the burrowed and laminated facies within Unit II suggests bottom current fluctuations throughout the deposition of this unit. Volcanic clasts in Unit II are restricted to traces of silt- to fine sand–sized palagonized volcanic glass and volcanic minerals of uncertain origin (Figure **F12**).
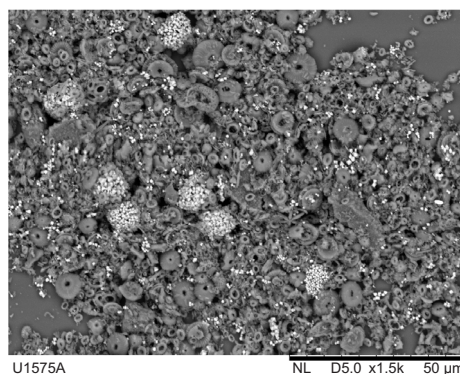
Figure F10. Pyrite framboids and microcrystallites in unconsolidated white nannofossil-foraminifera ooze in Unit I (391-U1575A-8R-4, 5 cm). Foraminifera are absent from the field of view due to preparation of the material.

3.1.3. Unit III

Interval: 391-U1575A-22R-1, 0 cm, to 22R-5, 32 cm
Depth: 203.80–209.92 mbsf
Age: late to mid-Campanian (~72–78 Ma)

Unit III is an approximately >6 m thick consolidated brown-pink nannofossil-foraminifera chalk with rare to minor radiolarians and clays (Figure **F9C**). One round sample (from interval 391-U1575A-22R-3, 140–150 cm) provided a $CaCO_3$ content of 74.1 wt%, which is consistent with the color of the sediment and a minor increase in clay abundance compared to Unit I (see **Sediment geochemistry**). Drilling disturbance (including rotational dislocation of segments) was significant in this unit but not always easy to identify due to an efficient resealing of core pieces after drilling-induced fracturing and rotation; such disturbance is clear, however, where planar laminations and inclined burrows were spliced before and/or during retrieval. The base of the unit and original (stratigraphic) sediment/basement interface was lost during drilling and retrieval; the drilling-induced contact between the sedimentary cover and underlying igneous basement was therefore used as the base of Unit III. A significant distinguishing feature between Units II and III is the occurrence of fragments of inoceramid shells restricted to Unit III. The age of the unit is defined by nannofossil assemblages as late to mid-Campanian (see **Biostratigraphy**). As with Unit II, due to limited shipboard biostratigraphic data and sediment recovery of only 47% and 73% in Units II and III, it is not clear whether the boundaries with overlying and underlying units are continuous or marked by depositional (and/or erosional) hiatus(es).

Five main lithofacies were recognized in the unit.

Lithofacies 1 is composed of brown-pink slightly to heavily burrowed nannofossil-foraminifera chalk and forms approximately 70% of the unit. This lithofacies is very similar to the burrowed facies of Unit II (Figure **F13A**).
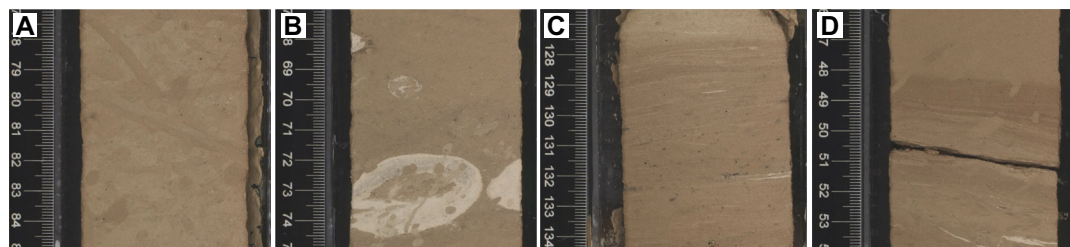
Figure F11. Main sedimentary structures of Unit II, Hole U1575A. A. Pervasive burrowing in nannofossil-foraminifera chalk with minor radiolarians and clays (Lithofacies 1; 21R-3, 77–85 cm). B. Larger burrow in nannofossil-foraminifera chalk with minor radiolarians and clays (Lithofacies 1; 21R-1, 67–75 cm). C. Planar and cross-lamination in nannofossil-foraminifera clayey siltstone with minor radiolarians and clays (Lithofacies 2; 21R-2, 126.5–134.5 cm). D. Planar and cross-lamination in nannofossil-foraminifera clayey siltstone with minor radiolarians and clays (Lithofacies 2; 21R-2, 46–54 cm).
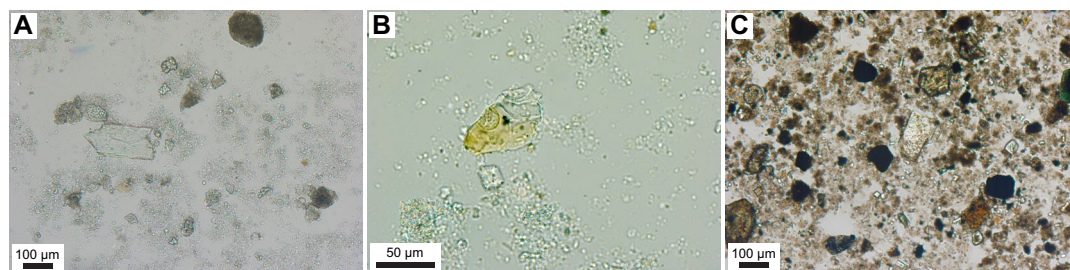

Figure F12. Volcanic clasts in Units II and III, Hole U1575A. A. Feldspar in nannofossil-foraminifera chalk with minor clays and radiolarians in Unit II (Lithofacies 1; 21R-2, 129 cm). B. Vesicular palagonized glass in nannofossil-foraminifera chalk with minor radiolarians and clays in Unit III (Lithofacies 2; 22R-2, 134 cm). C. Ferromagnesian and Fe oxide minerals in a laminated nannofossil-foraminifera silty claystone in Unit III (Lithofacies 5; 22R-4, 68 cm).

Lithofacies 2 is composed of brown laminated nannofossil-foraminifera clayey siltstone to sandstone and forms approximately 15% of the unit. This sediment includes common planar laminae and rarer cross-lamination formed by variable contents in foraminifera and finer components (i.e., nannofossils and clays). In addition, it also includes minor volcanic clasts, but the laminae do not appear to preferentially concentrate heavy minerals. Reverse grading occurs locally, revealed by sorting of the foraminifera (Figure **F13B**). Therefore, as with the laminated lithofacies of Unit II, the lamination in Unit III is interpreted as a result of winnowing and bedload transport by bottom currents. The absence of normal grading and heavy mineral accumulation does not support deposition from turbidites.

Lithofacies 3 is composed of brown-gray nannofossil-foraminifera chalk with convolute/contorted bedding, which forms approximately 15% of the unit. This facies is massive and matrix supported. It commonly includes larger fragments of inoceramid shells and rounded granules of white foraminifera sandstone (Lithofacies 4) (Figure **F13C**). Lithofacies 3 occurs in three intervals (see **Core descriptions**); in two of them, it displays contorted bedding and crosscuts the bedding of other lithofacies. This and the occurrence of rounded granules of sandstone suggest that Lithofacies 3 locally represents injections of fluidized sediments or sedimentary dikes. This facies may also include possible mass transport deposits.

Lithofacies 4 is composed of white bioclast sandstone with foraminifera and forms <1% of the unit. This lithofacies could also be classified as a bioclastic grainstone. It includes dominant angular to subrounded fragments of red algae with abundant benthic and planktonic foraminifera, fragments of mollusk shells, bryozoans, and echinoderms (Figure **F14**). The presence of good sorting, rounded grains, and a low abundance of finer components (e.g., nannofossils or micrite) in this deposit suggest reworking/winnowing by ocean floor (bottom) currents.

Lithofacies 5 is composed of dark brown volcanic siltstone that only occurs as fragments in drilling breccia and forms <1% of the recovered sediment (Figure **F13D**). This siltstone is moderately well
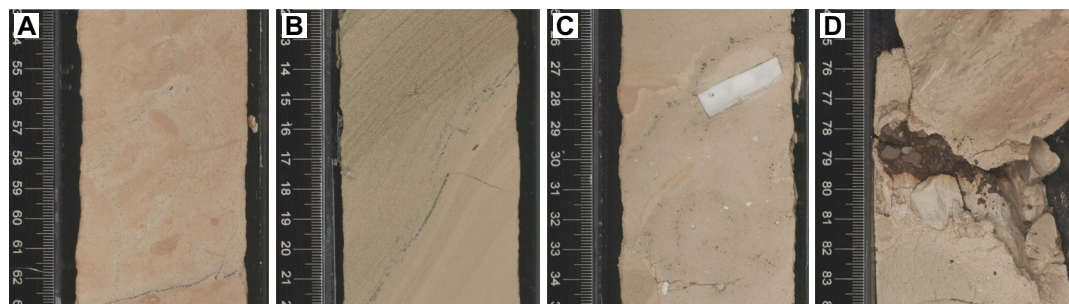
Figure F13. Unit III lithologies, Hole U1575A. A. Brown-pink slightly to heavily burrowed nannofossil-foraminifer chalk (Lithofacies 1; 22R-2, 53–63 cm). B. Brown laminated nannofossil-foraminifera clayey siltstone to sandstone (Lithofacies 2; 22R-3, 12–22 cm). C. Brown-gray nannofossil-foraminifera chalk with convolute/contorted bedding (Lithofacies 3; 22R-4, 25–35 cm). D. Dark brown volcanic siltstone (Lithofacies 5; 22R-4, 74–84 cm).
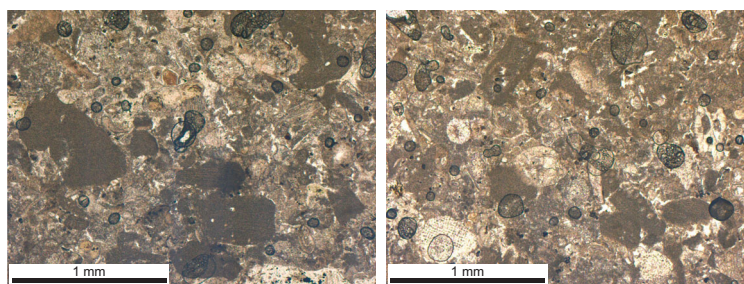
Figure F14. Bioclastic grainstone at the base of Unit III (Lithofacies 4; 391-U1575A-22R-5, 2–4 cm; thin section 2). This sediment includes abundant subrounded red algae and foraminifera, common subrounded fragments of shells and bryozoans, and rare subrounded fragments of echinoderms.

sorted and grain supported and is predominantly composed of heavy minerals of volcanic origin together with palagonized volcanic glass (Figure **F12C**). These characteristics suggest deposition through turbidity currents, although such an interpretation remains speculative due to poor recovery of the material and the absence of distinguishing sedimentary structure(s).

Similar to Unit II, Lithofacies 1–3 locally include black diffuse centimeter-sized patches and millimeter-sized particles and dendritic veins of diagenetic origin (probably pyrolusite). The alternation of burrowed and laminated facies (Lithofacies 1 and 2) suggests fluctuations in the strength of bottom current throughout the deposition of Unit III. Despite proximity to the igneous basement, only rare volcanic clasts were observed in this unit in the form of silt- to fine sand–sized palagonized volcanic glass or ferromagnesian and Fe oxide minerals (Figure **F12B, F12C**). Gravity currents could have led to the transport of the materials found in Lithofacies 5, whereas the remainder of the volcanic clasts were most likely supplied by dilute turbiditic plumes developing in the water column during submarine volcanic eruptions and subsequent mixing with pelagic sediment by bottom currents and burrowing. Sparse tephra deposition and reworking is another possible source for this volcaniclastic component.

Although incomplete core recovery at the sediment/basalt interface limits reconstruction of paleodepths at the end of volcanic activity, the presence of red algae debris in Lithofacies 4 strongly suggests a deposition depth of <300 mbsf. The occurrence of a nearby submarine volcanic shoal is possible, but it seems unlikely because volcaniclastic materials are extremely limited in deposits above the volcanic basement and are entirely absent in the volcanic basement. Nevertheless, material could also have been lost from the top of the basement because the preserved succession offers no indication regarding the completeness of the upper volcanic succession. In summary, the absence of bidirectional current indicators in the laminated sediment and lack of shallow marine fossils (e.g., coral or larger foraminifera) supports deposition below the wave base. Overall, this suggests deposition of Unit III between approximately 300 and 100 mbsf.

3.2. Sedimentary deposits in the igneous basement

The igneous basement (see **Igneous petrology and volcanology**) consists of a thick (~115 m) stack of eruptive units varying from very thick (>10 m) massive flow units to individual sheet flows and flow lobe and pillow lava stacks (<6 m). The tops of major flows often preserve glassy selvage and a chill zone; beneath this sequence, a network of cooling fractures frequently occurs, the upper reaches of which can act as a conduit for ingress and preservation of any sedimentary material deposited on the lava unit surface (i.e., carbonate ooze). Similarly, the eruption of pillow lavas and accumulation of pillow lava stacks onto thin sedimentary deposits has either patchily preserved these layers beneath the stack or interstitially incorporated the ooze within the interstices of the stack during its emplacement onto the ocean floor substrate.

Accordingly, sparse sedimentary rocks occur in the succession of massive and pillow lavas that forms the igneous basement at Site U1575. These sedimentary rocks are carbonates (originally pelagic oozes) and represent ≪1% of this succession; they likely formed during more prolonged hiatuses in volcanic activity and typically occur in <15 cm thick isolated intervals or infills (total cumulative thickness = 51.5 cm). No siliciclastic or volcaniclastic materials occur. Examples of these carbonates are found capping the glassy flow-top selvage of massive flows, and they are associated with pillow lavas where there is evidence of fluidal mixing of the seafloor sediment during pillow stack accumulation. Nannofossil assemblages from these sedimentary intervals yielded a probable Campanian age (see **Biostratigraphy**).

Two main lithofacies were recognized in the volcanic basement at Site U1575; they occur in three distinct intervals:

- 391-U1575A-23R-1, 77 cm, to 24R-1, 34.5 cm (214.27–218.05 mbsf);
- 35R-1, 137–146 cm (275.27–275.36 mbsf); and
- 39R-2, 137.5 cm, to 39R-3, 121 cm (305.85–307.00 mbsf).

Lithofacies 1 is composed of yellow-white burrowed nannofossil limestone found in centimeter-sized cavities and cracks within the tops of massive lava flows (Figure **F15A**). This facies is com-

Figure F15. Sedimentary infills and intervals in the volcanic basement, Hole U1575A. A. Yellow-white burrowed nannofossil limestone (Lithofacies 1; 24R-1, 22–37 cm). B. Yellow-white burrowed nannofossil limestone with foraminifera (Lithofacies 2; 39R-3, 106–123 cm).

monly associated with micrite and sparry calcite. In some instances, several cycles of sediment infill and carbonate mineralization are preserved.

Lithofacies 2 is composed of yellow-white burrowed nannofossil limestone with foraminifera and preferentially occurs in lava interbeds <15 cm thick (Figure **F15B**). This facies locally includes diffuse centimeter-sized layering, rare fragments of inoceramid shells, and black diagenetic patches and minerals (probably pyrolusite).

These lithofacies, together with the occurrence of pillow lavas and an absence of subaerial weathering or paleosols within the volcanic succession (see **Igneous petrology and volcanology**), indicate that this igneous basement developed entirely in submarine conditions. An absence of shallow marine fossils and the occurrence of fragments of inoceramid shells in the interbedded sediment support somewhat deeper marine conditions, perhaps at a water depth similar to that of Unit III (100–300 m). Because of preserved stratigraphic relationships between foraminifera-bearing sedimentary intervals (Lithofacies 1) and the enclosing eruptive units, the probable biostratigraphic Campanian ages are considered contemporaneous with the development of the volcanic succession; thus, there is a good preliminary indication regarding the age of late-stage volcanism prior to the onset of uninterrupted marine sedimentation at this site. However, infills solely resulting from percolation of nannofossil ooze in cracks in the basalts and devoid of foraminifera (Lithofacies 2) could be postvolcanic material significantly younger than the age of volcanism; this is especially the case for those preserved at the top of the uppermost flow upon which the basal sedimentary succession (Unit III) lies.

4. Igneous petrology and volcanology

Igneous rocks were recovered in Hole U1575A (Figure **F16**), which penetrated 122.4 m of igneous basement (interval 391-U1575A-22R-5, 32 cm, to 41R-2, 147 cm) and recovered 70.7 m (57.8%). The top of the igneous basement is an altered glassy flow top underlying almost 210 m of pelagic sediment. The igneous basement at Site U1575 represents Lithostratigraphic Unit IV in the overall

subseafloor succession (see **Lithostratigraphy**). Hole U1575A terminates in a massive sheet flow with a minimum thickness of 13 m; the bottom of this flow was not recovered. The igneous basement at Site U1575 comprises an alternating sequence of submarine lavas including massive flows up to 21 m thick as well as pillow and lobate lava flows (Figure **F17**). The occurrence of such massive flows is noteworthy. It requires an extremely high extrusion rate and a prodigious magma supply. This mode of volcanism is distinct from that occurring at mid-ocean ridges, where pillow lava and thin sheet flows are the dominant mode and massive flows are much less common. The lavas recovered from Hole U1575A are aphanitic to intersertal to holocrystalline basalts with glomerocrysts and phenocrysts of plagioclase (3–15 vol%) and clinopyroxene (1–5 vol%). Olivine is sparse, only intermittently present (0–3 vol%), and almost always altered. The lavas only contain sparse (0–1 vol%), small (~1 mm) vesicles, suggesting a low gas content or that they were fairly degassed.

4.1. Igneous unit descriptions

A total of 10 igneous units were identified in Hole U1575A (Figure **F16**). Many of these comprise one or two massive flows. Unit boundaries were defined by the transition from one eruptive regime to another (e.g., massive lava to pillow lava or vice versa) or by changes in phenocryst abundance (from sparsely to highly phyric or vice versa). Two unit boundaries (1/2 and 9/10) are defined by thin layers of pelagic sediment.

Units 1 and 2 and the top of Unit 3 are characterized by high phenocryst abundance with common absorption textures and other indicators of disequilibrium, suggesting significant magma mixing and/or disaggregation of xenolithic cumulates prior to eruption. Deeper units have lower pheno-
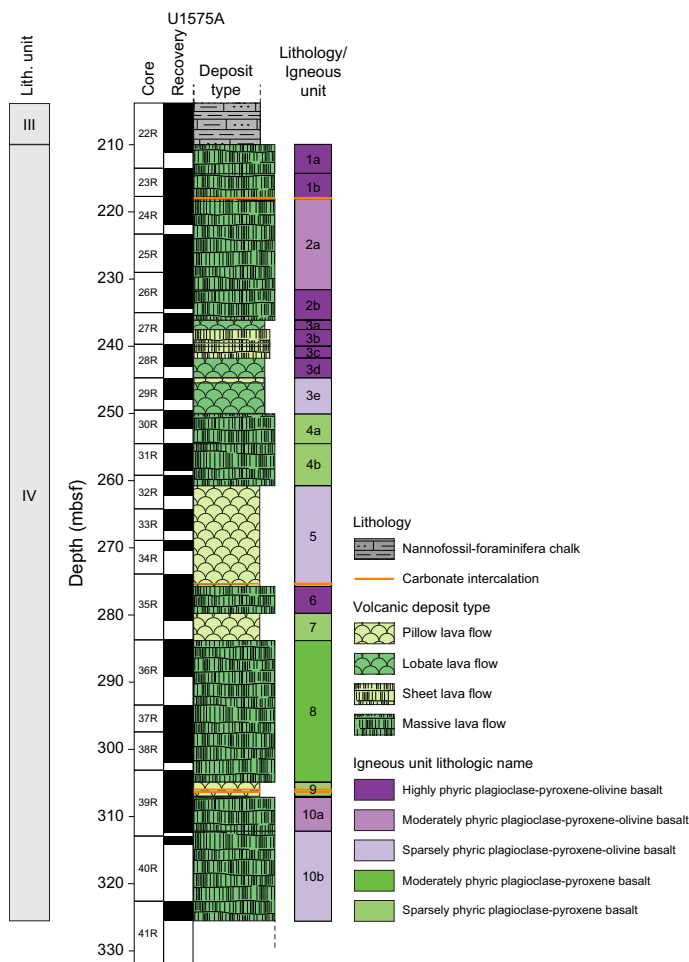
Figure F16. Stratigraphic column showing the volcanic succession in Unit IV, Hole U1575A.
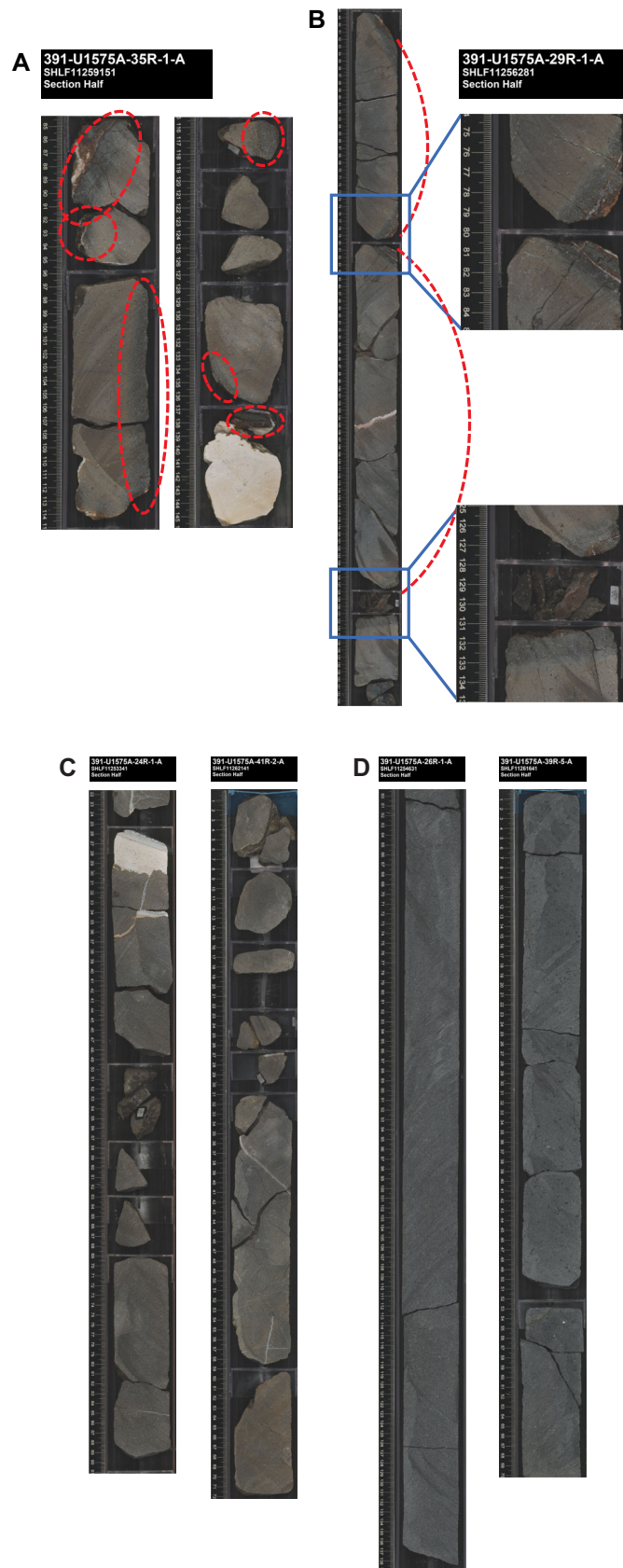
Figure F17. Cut core surfaces showing examples of pillow lavas and massive lava flows, Hole U1575A. A. Small pillow fragments with fresh glassy rims (red dashed ovals) and variably altered interiors. B. More complete pillow basalt stack with red dashed lines extrapolating the pillow tops beyond the recovered section. Close-up photos of the pillow lavas reveal reasonably fresh glass rims. C, D. Massive lava flows: (C) fragmented core and (D) continuous core, 100% recovery.

cryst abundances, and evidence for magma mixing is present but less common. Plagioclase is the dominant phenocryst phase in all units, commonly forming glomerocrysts with clinopyroxene, but plagioclase also occurs as large individual tabular crystals. A handheld portable X-ray fluorescence (pXRF) spectrometer was used to monitor the abundance of the heavier elements during core logging to provide a real-time assessment of chemical variability and to identify chemically distinct units (see **Igneous petrology** in the Expedition 391 methods chapter [Sager et al., 2023] for discussion of calibration and use). Elements that proved particularly useful for chemostratigraphy were TiO_2, Sr, and Zr (see **Igneous geochemistry**; Figure **F36**). We used these data to define three chemical types: high TiO_2 (the dominant, "normal" composition), low TiO_2, and a transitional type that ranges between high and low. Units 1–5 are the dominant, high-TiO_2 chemical type. Units 6–9 are the low-TiO_2 type. Unit 10 is divided into a transitional type (Subunit 10a) and a normal high-TiO_2 chemical type (Subunit 10b).

4.1.1. Unit 1

Interval: 391-U1575A-22R-5, 28 cm, to 24R-1, 25.5 cm
Depth: 209.92–217.96 mbsf
Drilled thickness: 8.04 m

Unit 1 comprises two massive, highly phyric (plagioclase-pyroxene-olivine) basalt flows. The upper contact of both units is defined by a glassy chilled margin. Subunit 1a is overlain by pelagic sediments. The lower contact with Unit 2 is defined by a thin calcareous horizon (5 cm thick).

4.1.1.1. Subunit 1a

Interval: 391-U1575A-22R-5, 28 cm, to 23R-1, 74.5 cm
Depth: 209.92–214.24 mbsf
Drilled thickness: 4.32 m
Recovered thickness: 2.055 m
Rock type: highly phyric plagioclase-pyroxene-olivine basalt
Deposit: massive flow, glass rim on top with fine-grained flow interior
Chem type: high TiO_2

Subunit 1a is a single massive flow with glomeroporphyritic textures and fine-grained, equigranular groundmass. Phenocrysts make up 10%–17% of the subunit, which is dominated by plagioclase (10%–12%) forming large glomerocrysts with pyroxene (2%–3%). Olivine is a minor phenocryst phase (0.5%–3%) and is completely altered, largely to iddingsite. Overall alteration is minor, manifested as patchy light brown discoloration of the groundmass.

4.1.1.2. Subunit 1b

Interval: 391-U1575A-23R-1, 74 cm, to 24R-1, 25.5 cm
Depth: 214.24–217.96 mbsf
Drilled thickness: 3.71 m
Recovered thickness: 4.4 m
Rock type: highly phyric plagioclase-pyroxene-olivine basalt
Deposit: massive flow, glass rim on top with fine-grained flow interior
Chem type: high TiO_2

Subunit 1b is another single massive flow. It has a fine-grained flow interior, which is sparsely vesicular, and the top is defined by a glassy margin. The texture is glomeroporphyritic with fine-grained, equigranular groundmass and 18%–20% phenocrysts (plagioclase = 10%–12%; pyroxene = 5%; olivine = 3%). Olivine is largely altered to iddingsite. Overall alteration is minor, manifested as light brown discoloration of the groundmass.

4.1.2. Sedimentary Subunit S1

Interval: 391-U1575A-24R-1, 25.5 cm, to 24R-1, 30 cm
Depth: 217.96–218.00 mbsf

Sedimentary Subunit S1 is a calcareous rock.

4.1.3. Unit 2

Interval: 391-U1575A-24R-1, 30 cm, to 27R-1, 108 cm
Depth: 218.00–236.08 mbsf
Drilled thickness: 18.08 m

Unit 2 comprises two massive highly phyric (plagioclase-pyroxene-olivine) basalt flows. A thin calcareous horizon (5 cm thick) separates Unit 2 from Unit 1; the lower contact is marked by the transition to pillow and lobate lava flows.

4.1.3.1. Subunit 2a

Interval: 391-U1575A-24R-1, 30 cm, to 26R-2, 116 cm
Depth: 218.00–231.56 mbsf
Drilled thickness: 13.56 m
Recovered thickness: 12.61 m
Rock type: moderately to highly phyric plagioclase-pyroxene-olivine basalt
Deposit: massive flow, glass rim on top with fine-grained flow interior
Chem type: high TiO_2

Subunit 2a is a massive sheet flow, single flow unit separated from Unit 1 by a calcareous layer in interval 391-U1575A-24R-1, 25–30 cm. The texture is glomeroporphyritic with fine-grained, equigranular groundmass. There are 13%–22% phenocrysts (plagioclase = 7%–12%; pyroxene = 2%–5%; olivine = 1%–5%), with plagioclase-pyroxene glomerocrysts dominating. Olivine is altered to iddingsite, but overall alteration is minor, limited to slight oxidation of the upper 1 m of the flow.

4.1.3.2. Subunit 2b

Interval: 391-U1575A-26R-3, 0 cm, to 27R-1, 108 cm
Depth: 231.56–236.08 mbsf
Drilled thickness: 4.52 m
Recovered thickness: 4.01 m
Rock type: highly phyric plagioclase-pyroxene-olivine basalt
Deposit: massive flow, glass rim on top with fine-grained flow interior
Chem type: high TiO_2

Subunit 2b is a massive flow, single flow unit. The texture is porphyritic with fine-grained, equigranular groundmass containing 5%–18% phenocrysts of plagioclase (3%–12%), clinopyroxene (2%–4%), and olivine (1%–3%), with plagioclase-pyroxene glomerocrysts dominating. Olivine is completely altered, largely to iddingsite, but overall alteration is minor, limited to slight oxidation of the upper 80 cm of the flow.

4.1.4. Unit 3

Interval: 391-U1575A-27R-1, 108 cm, to 30R-1, 53 cm
Depth: 236.08–250.03 mbsf
Drilled thickness: 13.95 m

Unit 3 comprises a sequence of lobate, pillow, and sheet flows that range 1.4–5.3 m thick. The upper and lower contacts mark transitions to the massive sheet flows of Unit 2 and Unit 4.

4.1.4.1. Subunit 3a

Interval: 391-U1575A-27R-1, 108 cm, to 27R-2, 98 cm
Depth: 236.08–237.48 mbsf
Drilled thickness: 1.4 m thick
Recovered thickness: 1.4 m
Rock type: highly phyric plagioclase-pyroxene-olivine basalt
Deposit: lobate and pillow lava flows
Chem type: high TiO_2

Subunit 3a consists of alternating pillow and lobate lava flows. Flow tops are marked by glass rims. Texturally, the unit consists of holocrystalline, fine-grained, equigranular groundmass and 12%–13% phenocrysts (plagioclase = 7%–10%; pyroxene = 1%–4%; olivine = 1%–3%) with glomerocrysts of plagioclase and clinopyroxene. Olivine is completely altered, largely to iddingsite, but overall alteration is minor, limited to slight patchy oxidation to light tan.

4.1.4.2. Subunit 3b

Interval: 391-U1575A-27R-2, 98 cm, to 28R-1, 27 cm
Depth: 237.48–239.97 mbsf
Drilled thickness: 2.49 m
Recovered thickness: 0.74 m
Rock type: highly phyric plagioclase-pyroxene-olivine basalt
Deposit: sheet flow, glass rim on top (single flow unit)
Chem type: high TiO_2

Subunit 3b consists of a single sheet flow marked by a glassy flow top. The sheet flow has fine-grained, aphanitic to holocrystalline, equigranular groundmass and 10%–16% phenocrysts (plagioclase = 5%; pyroxene = 5%; olivine = 1%–2%) with glomerophyres of plagioclase and pyroxene. Olivine is replaced by iddingsite, and the entire subunit has slight oxidative alteration (tan discoloration).

4.1.4.3. Subunit 3c

Interval: 391-U1575A-28R-1, 27 cm, to 28R-2, 59 cm
Depth: 239.97–241.74 mbsf
Drilled thickness: 1.77 m
Recovered thickness: 1.77 m
Rock type: highly phyric plagioclase-pyroxene-olivine basalt
Deposit: sheet flow, glass rim on top (single flow unit)
Chem type: high TiO_2

Subunit 3c is another single sheet flow unit. The top of the flow is marked by an intensely altered chilled margin associated with discoloration that fades into the interior over about 10 cm. The sheet flow contains holocrystalline fine-grained, equigranular groundmass and 14%–16% phenocrysts (plagioclase = 7%–10%; clinopyroxene = 3%–5%; olivine = 2%–3%) with glomerophyres of plagioclase and pyroxene. Olivine is replaced by iddingsite. There is slight oxidative alteration (tan discoloration) in patches.

4.1.4.4. Subunit 3d

Interval: 391-U1575A-28R-2, 59 cm, to 28R-3, 41 cm
Depth: 241.74–243.06 mbsf
Drilled thickness: 2.96 m
Recovered thickness: 1.32 m
Rock type: highly phyric plagioclase-pyroxene-olivine basalt
Deposit: lobate lava and pillow lava
Chem type: high TiO_2

Subunit 3d consists of lobate flows that resemble pillows but form lobes >1 m thick. Basalts have fine-grained, equigranular groundmass and 11%–16% phenocrysts (plagioclase = 5%–7%; pyroxene = 5%–7%; olivine = 1%–2%) with glomerophyres of plagioclase and pyroxene. There is slight, patchy oxidative alteration throughout the unit (tan discoloration), but olivine is completely altered.

4.1.4.5. Subunit 3e

Interval: 391-U1575A-29R-1, 0 cm, to 30R-1, 53 cm
Depth: 244.70–250.03 mbsf
Drilled thickness: 5.83 m

Recovered thickness: 3.72 m
Rock type: sparsely to moderately phyric plagioclase-pyroxene-olivine basalt
Deposit: lobate lava and pillow lava
Chem type: high TiO$_2$

Subunit 3e consists of pillow lava and lobate flows. Pillow lavas are 30–50 cm in diameter with 1–2 cm thick glass rims, and lobate lava resembles pillows but forms lobes >1 m thick. Basalts are glomeroporphyritic with fine-grained, equigranular groundmass. Subunit 3e has fewer overall phenocrysts (4%–8%) than higher stratigraphic units, and they consist of plagioclase (3%–5%), pyroxene (1%–2%), and olivine (1%). Olivine is commonly but not always altered to iddingsite, and slight oxidative alteration varies from patchy to pervasive.

4.1.5. Unit 4

Interval: 391-U1575A-30R-1, 53 cm, to 32R-2, 14 cm
Depth: 236.08–260.72 mbsf
Drilled thickness: 10.69 m

Unit 4 comprises two massive, sparsely phyric (plagioclase-pyroxene±olivine) basalt flows. The upper and lower contacts are marked by a transition to pillow and lobate lava flows.

4.1.5.1. Subunit 4a

Interval: 391-U1575A-30R-1, 53 cm, to 30R-3, 60 cm
Depth: 250.03–255.08 mbsf
Drilled thickness: 5.05 m
Recovered thickness: 2.74 m
Rock type: sparsely to moderately phyric plagioclase-pyroxene basalt
Deposit: massive flow (single flow)
Chem type: high TiO$_2$

Subunit 4a is a single massive sheet flow. There is no visible contact preserved with the overlying pillow lavas. The rock texture is porphyritic with aphanitic, microcrystalline groundmass. Phenocrysts (3%–6% total) consist of plagioclase (2%–4%) and pyroxene (0.5%–2%). Rare olivine (<0.5%) is visible macroscopically. This subunit has mild patchy (pale tan) alteration.

4.1.5.2. Subunit 4b

Interval: 391-U1575A-31R-1, 0 cm, to 32R-2, 14 cm
Depth: 255.08–260.72 mbsf
Drilled thickness: 5.64 m
Recovered thickness: 4.96 m
Rock type: sparsely to moderately phyric plagioclase-pyroxene basalt
Deposit: massive flow (single flow unit)
Chem type: high TiO$_2$

Subunit 4b is a single massive sheet flow. The upper contact is marked by a weathered interval about 60 cm thick at the top of the flow. It is porphyritic rock with microcrystalline groundmass. Phenocrysts (3%–6% total) consist of plagioclase (2%–4%) and pyroxene (0.5%–2%). Rare olivine (<1%) is visible macroscopically. This subunit has mild patchy (pale tan) alteration.

4.1.6. Unit 5

Interval: 391-U1575A-32R-2, 14 cm, to 35R-2, 38 cm
Depth: 260.72–275.74 mbsf
Drilled thickness: 15.02 m
Recovered thickness: 8.21 m
Rock type: sparsely to moderately phyric plagioclase-pyroxene-olivine basalt
Deposit: pillow lava, may include thin sheet flows and lobate flows
Chem type: high TiO$_2$

Unit 5 consists dominantly of pillow lava flows that may include thin sheet flows and lobate flows. Glass selvages mark quenched rims of pillows, pillow lobes, and/or thin sheet flows. Just below the quenched rims, pillow textures have aphanitic groundmass with faint pinkish alteration. Farther in the pillow interior, the phenocryst proportions increase modestly and the groundmass grades to fine grained. Pillow lavas are porphyritic with 4%–10% phenocrysts (plagioclase = 3%–5%; pyroxene = 1%–4%; olivine = 0%–2%). Olivine is altered to iddingsite. This unit has mild patchy alteration to pale tan. There is a thin (8 cm) chalk intercalation near the bottom of the unit (interval 35R-1, 136–148 cm).

4.1.7. Unit 6

Interval: 391-U1575A-35R-2, 38 cm, to 35R-5, 43 cm
Depth: 275.74–279.73 mbsf
Drilled thickness: 3.99 m
Recovered thickness: 3.99 m
Rock type: sparsely to highly phyric plagioclase-pyroxene-olivine basalt
Deposit: massive flow, single flow unit
Chem type: low TiO_2

Unit 6 consists of a single massive flow of low-TiO_2 basalt. Glass selvage marks the upper contact with Unit 5. Below the glass rim, the lava is sparsely phyric with microcrystalline groundmass but grades into moderately to highly phyric/glomerophyric with holocrystalline groundmass toward the interior of the flow. Glomerocrysts consist dominantly of plagioclase with sparse pyroxene. Phenocryst totals show a large range (5–14 vol%) consistent with fewer phenocrysts near the top and bottom flow boundaries. Phenocrysts consist of plagioclase (3%–10%), pyroxene (2%–3%), and olivine (0%–1%). Pale tan oxidative alteration is patchy and largely confined to upper and lower margins of the flow.

4.1.8. Unit 7

Interval: 391-U1575A-35R-4, 43 cm, to 36R-1, 7.5 cm
Depth: 279.73–283.78 mbsf
Drilled thickness: 4.05 m
Recovered thickness: 1.12 m
Rock type: sparsely to highly phyric plagioclase-pyroxene basalt with rare olivine
Deposit: pillow lava flows
Chem type: low TiO_2

Unit 7 is a stack of low-TiO_2 pillow basalt. Pillows are marked by an upper glassy rind that grades to altered, sparsely to highly phyric basalt. The lavas are glomerophyric to phyric with fine-grained to microcrystalline, equigranular groundmass. Phenocrysts range 4%–12% (plagioclase= 3%–10%; pyroxene = 1%–2%; olivine = 0%–1%) with variations linked to pillow rims (low phenocryst cargo) to pillow interiors (higher phenocryst cargo). This unit has tan oxidative discoloration.

4.1.9. Unit 8

Interval: 391-U1575A-36R-1, 7.5 cm, to 39R-2, 38.5 cm
Depth: 283.78–304.86 mbsf
Drilled thickness: 21.08 m
Recovered thickness: 16.99 m
Rock type: moderately phyric plagioclase-pyroxene basalt with rare olivine
Deposit: massive flow; single flow unit
Chem type: low TiO_2

Unit 8 consists of a single massive flow of low-TiO_2 lava marked by a quenched and discolored (altered) chilled contact near the top of the flow that grades to fresh material toward the interior. This is a very thick single flow unit with a glassy upper contact and no evidence of additional internal contacts. The texture is glomerophyric with 5%–9% phenocrysts in fine-grained, equigranular groundmass. Plagioclase is the dominant phenocryst phase (4%–7%) with only 1%–2% pyroxene

and rare olivine. The unit has pale tan oxidative alteration in the upper 60 cm of the flow, and the interior is very fresh dark gray-green. A network of calcite-filled veins 2–6 mm thick is found in the upper 60 cm of the altered flow. Calcite veins are rare in the flow interior.

4.1.10. Unit 9

Interval: 391-U1575A-39R-2, 38.5 cm, to 39R-3, 107 cm
Depth: 304.86–306.96 mbsf
Drilled thickness: 2.10 m
Recovered thickness: 1.92 m
Rock type: sparsely to moderately phyric plagioclase-pyroxene basalt with rare olivine (0%–2%)
Deposit: pillow lavas with intermixed calcareous sediment (peperite)
Chem type: low TiO_2

Unit 9 is a sequence of low-TiO_2 pillow lavas intermixed with calcareous sediment. One composite piece of the section shows basalt glass fused to the sediment. This is interpreted to represent pillows that erupted onto and mingled with pelagic ooze. The basalt textures are porphyritic to glomerophyric with fine-grained to microcrystalline, equigranular groundmass. Phenocrysts total 6%–7% with subequal portions of plagioclase, pyroxene, and olivine (2%–3% of each). There is slight Fe oxyhydroxide alteration with patchy tan discoloration, clay mineralization, and alteration of olivine to iddingsite

4.1.11. Sedimentary Subunit S2

Interval: 391-U1575A-39R-3, 107 cm, to 39R-3, 122 cm
Depth: 306.96–307.11 mbsf

Sedimentary Subunit S2 is a thin 15 cm bedded chalk layer that separates Igneous Units 9 and 10.

4.1.12. Unit 10

Interval: 391-U1575A-39R-3, 122 cm, to 41R-2, 147 cm
Depth: 307.11–325.52 mbsf
Drilled thickness: 18.42 m

Unit 10 comprises two massive lava flows with chilled margins at the top and bottom of the upper massive flow.

4.1.12.1. Subunit 10a

Interval: 391-U1575A-39R-3, 122 cm, to 39R-7, 104.5 cm
Depth: 307.11–312.17 mbsf
Drilled thickness: 5.06 m
Recovered thickness: 5.06 m
Rock type: moderately phyric plagioclase-pyroxene-olivine basalt
Deposit: massive lava flow; single flow unit
Chem type: transitional to high TiO_2

Subunit 10a is a single massive lava flow. It is marked by a lower chilled margin separating it from Subunit 10b. The lavas are moderately porphyritic to microporphyritic with 6%–10% phenocrysts in fine-grained, holocrystalline to microcrystalline, equigranular groundmass. Phenocrysts include plagioclase (3%–7%), pyroxene (1%–3%), and olivine (1%–2%). This unit contains rare round vesicles (2%) that are 1–5 mm in diameter and filled with a bluish zeolite. Likewise, the unit as a whole is slightly altered with brownish to bluish discoloration. Subunit 10a is a compositionally transitional unit showing a gradual increase from low-TiO_2 lavas to high (normal)-TiO_2 lavas.

4.1.12.2. Subunit 10b

Interval: 391-U1575A-39R-7, 104.5 cm, to 41R-2, 147 cm
Depth: 312.17–325.52 mbsf
Drilled thickness: 13.36 m
Recovered thickness: 4.38 m

Rock type: sparsely to moderately phyric plagioclase-pyroxene-olivine basalt
Deposit: massive lava flow, single flow unit
Chem type: high TiO_2

Subunit 10b is a single massive lava flow. The upper chilled margin is not preserved. Lava contains 5%–10% phenocrysts (plagioclase = 3%–6%; pyroxene = 1%–3%; olivine = 1%–2%) in holo-crystalline, fine-grained to microcrystalline, equigranular groundmass. As a whole, the unit shows pinkish tan alteration.

4.2. Petrography

Magmatic textures observed in thin section do not appear to correlate with lava composition. They depend on the eruptive style of the lava, which has a direct impact on cooling rates. In general, pillow lavas and lobate flows have quenched or microcrystalline groundmass with distinct phenocrysts. In contrast, massive flows are characterized by seriate groundmass textures that grade into the larger phenocrysts, reflecting slower cooling rates in the massive flows.

4.2.1. Massive flows

Massive lavas are highly to moderately phyric and primarily contain plagioclase and clinopyroxene. Massive lavas exhibit glomeroporphyritic, porphyritic, and intersertal textures (Figure **F18**). Plagioclase and clinopyroxene occur as large glomerocrysts and groundmass phases. Olivine
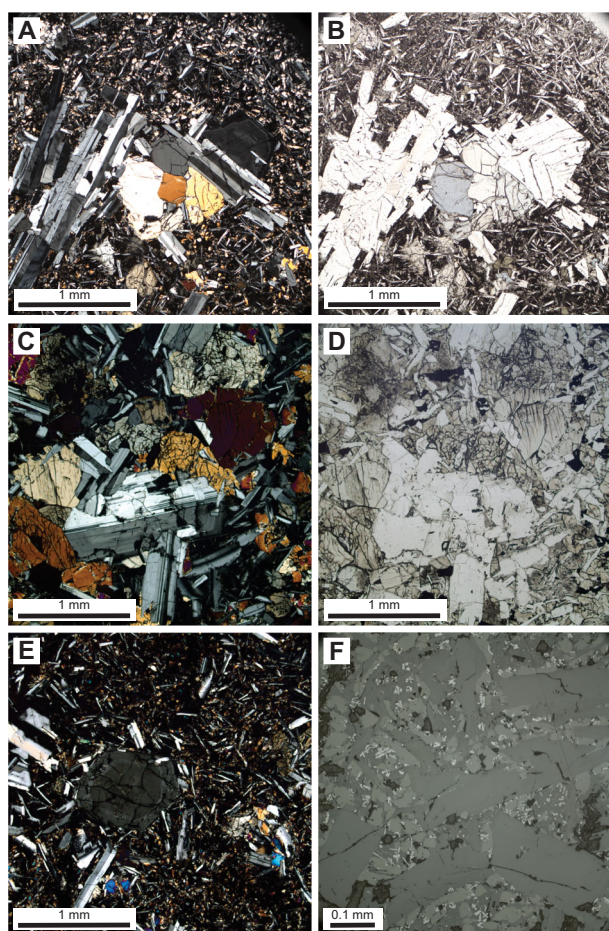
Figure F18. Massive lavas, Hole U1575A. A, B. Massive flow with glomeroporphyritic texture, a clear divide between phenocrysts and groundmass, and zoned plagioclase (30R-2, 6–10 cm; A = cross-polarized light [XPL], B = plane-polarized light [PPL]). C, D. Massive flow with glomeroporphyritic and seriate textures along with plagioclase zoning (26R-2, 22–26 cm; C = XPL, D = PPL). E. Clinopyroxene with patchy zoned core and oscillatory zoning near the rim along with a resorbed contact between the different zoning patterns (25R-4, 7–10 cm; XPL). F. Skeletal groundmass oxides (white crystals) and fresh glass between the phenocrysts (25R-4, 7–10 cm; reflected light).

occurs infrequently and is often observed as altered phenocrysts or groundmass (i.e., iddingsite). Plagioclase in glomerocrysts commonly exhibits oscillatory zoning at its rims and patchy zoning at its core. Some plagioclase crystals also have sieve-textured cores. Clinopyroxene zoning is less common but occurs as hourglass and oscillatory patterns. Plagioclase and pyroxene often contain melt inclusions. Some massive lavas exhibit a clear divide between phenocrysts and groundmass; however, most exhibit seriate texture and continuously grade from small to large crystals. The groundmass often contains plagioclase, clinopyroxene, and skeletal Fe oxide crystals ± olivine. Fresh glass can be found in some samples, but it is more often altered and replaced by clay minerals.

4.2.2. Pillow lava

Pillow lavas contain plagioclase and clinopyroxene phenocrysts and glomerocrysts in the glassy rind and in the interior of the pillows (Figure F19). Olivine is also present in sparse amounts, but it has been completely replaced by iddingsite. Plagioclase phenocrysts and glomerocrysts occasionally exhibit oscillatory zoning and contain melt inclusions. Pyroxenes rarely exhibit zoning but can exhibit oscillatory zoning patterns. The glassy rinds consist of fresh basaltic glass with plagioclase microlites and bands of palagonite. Alteration halos are common around crystals in the glassy rind of the pillow. The pillow interiors have a highly altered matrix of highly oxidized glass with skeletal plagioclase groundmass crystals. Altered olivine is also present in the groundmass along with clinopyroxene and rare Fe oxides.

4.3. Alteration in igneous units

All alteration in the basement igneous succession is due to low-temperature processes or ambient seafloor chemical weathering. Alteration intensity of the eruptive units is typically slight to occasionally moderate throughout with larger flow interiors presenting near-fresh materials except for olivine, which is commonly entirely replaced by iddingsite (i.e., a mixture of clay minerals and Fe oxyhydroxides). Other primary igneous minerals are typically retained, and only minor replacement is observed in feldspar (kaolinite) and occasional oxidative Fe oxyhydroxide films around pyroxenes. Fresh glass occurs at the margins of the pillow lavas and as remnants of glassy selvages at the tops of aphanitic chilled margins in the upper edges of some of the massive flows and rarely at the bases of massive flows. Otherwise, the glass is frequently altered to palagonite.
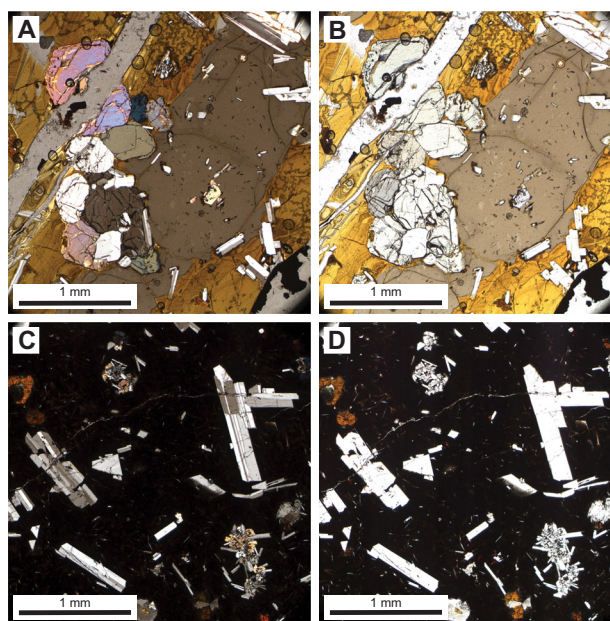
Figure F19. Pillow lavas, Hole U1575A. A, B. Pillow lava rim with fresh glass in center of photomicrograph, altered glass (palagonite) near fractures on both sides of band of fresh glass; glomerocryst of clinopyroxene and plagioclase cut by a vein, and olivine microlites altered to iddingsite (29R-1, 43–46 cm; A = XPL, B = PPL). C, D. Pillow lava interior with large euhedral plagioclase phenocrysts, small clinopyroxene-plagioclase glomerocrysts, and olivine microphenocrysts altered to iddingsite (29R-1, 43–46 cm; C = XPL, D = PPL).

In effect, there are negligible quantities of secondary minerals throughout the volcanic sequence, but those that do occur are disseminated as within-crystal alteration (e.g., plagioclase) or oxidative films around crystals (e.g., pyroxene), and these changes impart minor color changes from unaltered blue-gray flow interiors to a light brown typical of upper margins and, to a lesser extent, the lower contacts of larger units. In the smaller sheet and lobate flow units, this brown alteration is more pervasive, extending over 70% of the flow interior. Pillow lavas typically display concentric alteration color extending from the outer glassy margin inward, and only larger pillows (>1 m) retain relatively unaltered interiors. The brown colors throughout the different units are likely the result of oxidation of primary ferromagnesian minerals, notably olivine when present (to iddingsite) and to a lesser extent pyroxene. Formation of small quantities of secondary Fe oxyhydroxides imparts an increasingly brown cast as alteration progresses.

It is probable that the greater part of the oxidative alteration occurred shortly after eruption as the rapidly cooling lava unit interacted with seawater, often further facilitated by the development of cooling fractures in the brittle outer flow crust. Fracturing allowed ingress of fluids and likely accounts for the broader oxidation zones in the upper parts of larger flows to a depth of 0.1–1 m depending on flow size compared with somewhat thinner alteration zones in the unit base. Where cooling fractures are absent in the flow interiors, discoloration and, hence, alteration are at a minimum.

In the major massive flows, cooling fractures commonly extend into a finer, anastomosing vein network in the uppermost third of the unit. Calcite infilling is typical in the upper parts of these networks, and Fe oxyhydroxide fillings are associated with the lower networks and impinge into the upper interior region of the larger flows. Rarely, alteration has liberated silica from the primary silicates, which were redeposited as vein infillings or, in one exceptional instance, as a large geode with euhedral calcite crystals within a void (interval 391-U1575A-31R-1, 83–88 cm); the origin of the void is unclear, but it may have been a gas-filled cavity (Figure **F20**). Pillow lavas contain radial fractures that penetrate the center of the unit, enabling pervasive moderate alteration throughout the pillow.

Vesicles are rare, typically occurring as round isolated voids (<1 mm), rare vesicle segregations, or pipe vesicle zones in the interior regions of the largest flows. Vesicle infill is typically calcite or microcrystalline silica (chalcedony). The latter can be observed with a binocular microscope occurring as coalescing botryoidal growths in larger vesicles and voids.

In places, the igneous sequence is associated with pelagic carbonate deposits, which occur on top of the uppermost massive flow, and associated materials that percolated into the flow interior via jointing. Elsewhere, pillow lavas interacted with thin sedimentary layers. Here, the carbonate was fluidized and thermally altered (i.e., marbleized) (see fragments in interval 391-U1575A-39R-3, 0–50 cm). Where the eruptive units are associated with carbonate cover calcite veining, sparry calcite commonly occurs (e.g., intervals 391-U1575A-22R-6, 70–80 cm, and 39R-4, 36–70 cm) (Figure **F20**).

**Figure F20.** Sparry calcite crystals in gas blister vug (391-U1575A-34R1, 82–88 cm).

4.4. Discussion

The lavas in Hole U1575A reveal remarkable textural and mineralogical consistency with subtle variations in groundmass grain size and moderate changes in phenocryst abundance, often (but not always) associated with proximity to flow boundaries. The upper units at Site U1575 are defined mostly by changing eruptive styles of basaltic lavas rather than compositional differences. However, beginning with Section 391-U1575A-35R-2, a notable difference in chemistry accompanies the volcanological boundary within the upper units. The low-TiO_2 lavas are mineralogically distinct in that they are dominantly olivine free and consistently contain lower plagioclase and clinopyroxene abundances. These low-TiO_2 lavas may indicate a shift from mildly alkaline to more tholeiitic compositions. Transitional to high-TiO_2 lavas mark a return to phenocryst proportions similar to the upper, high-TiO_2 units and, therefore, possibly a return to mildly alkaline lavas.

A major break in phenocryst distribution occurs in Hole U1575A at ~245 mbsf between Igneous Subunits 3d and 3e (Figure F21). Above this depth, the basalts are generally highly phyric with more than 10% phenocrysts (plagioclase-pyroxene-olivine). In contrast, below this depth the basalts range from aphyric to sparsely or moderately phyric with less than 10% total phenocrysts. This is not simply a function of the cooling rate because the transition occurs within a unit comprising pillow and sheet lava flows, and massive flows are found above and below. Furthermore, the phenocryst abundance does not correlate with composition. Units with low phenocryst abundances include all three TiO_2 chem types: low TiO_2, high TiO_2, and transitional.

The change in phenocryst abundance most likely reflects storage and eruption dynamics of the magmatic systems, with high crystal loads resulting from longer residence times in shallow magma chambers or from eruption of crystal mushes.
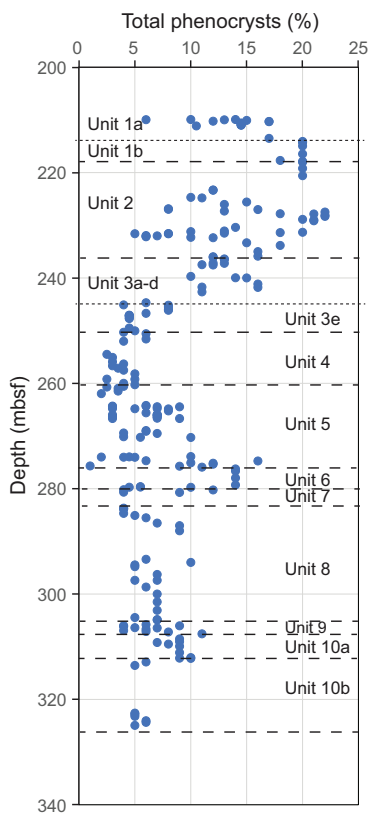
Figure F21. Phenocryst loads, Site U1575. Phenocryst abundances are largely controlled by plagioclase abundance. Total phenocryst content is generally 10%–20% above 245 mbsf and 2%–8% below. This change in phenocryst load occurs within the high-TiO_2 chemical type (Igneous Units 1–5).
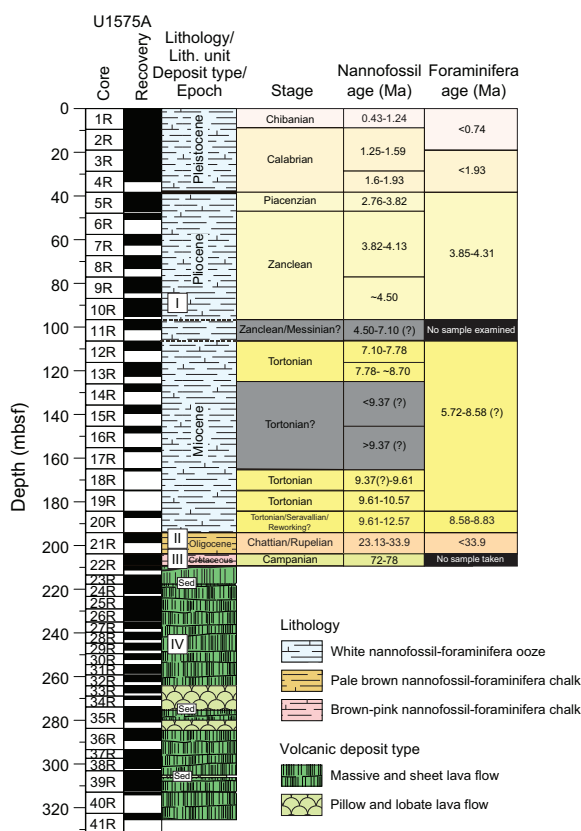
5. Biostratigraphy

Calcareous nannofossils and planktonic foraminifera provided preliminary zonal and stage assignments for sediments recovered at Site U1575. A 210 m thick succession of sediments was recovered, ranging in age from the Pleistocene through the Upper Cretaceous (Campanian). For shipboard analyses, we considered first occurrence (FO) and last occurrence (LO) datums for planktonic foraminifera and calcareous nannofossils.

Figure **F22** shows calcareous nannofossil and planktonic foraminifera biohorizon ages (see **Lithostratigraphy**). The age-depth model (Figure **F23**) was obtained by plotting biostratigraphic data against depth (mbsf scale). Chronostratigraphic boundaries are from the 2020 geologic timescale (GTS; Gradstein et al., 2020). Biostratigraphic zonations for calcareous nannofossils and planktonic foraminifera can be found in Tables **T2** and **T3**, respectively.

5.1. Calcareous nannofossils

Calcareous nannofossil assemblages were examined in core catcher samples from Hole U1575A. A total of 21 core catcher samples were studied, and additional toothpick samples were taken where possible for increased biostratigraphic rigor. Ages and depths of key biostratigraphic markers are provided below on a preliminary basis. Core 22R recovered the transition from sediment to basement. No sediment was recovered in the core catcher. Two toothpick samples were taken (22R-1, 11−12 cm, and 22R-5, 27−28 cm) to provide an age range from the top of Core 22R to the sediment just above the basement.

Nannofossil abundance is extremely high throughout the hole, and almost every sample is considered a flood (for abundance scale, see **Biostratigraphy** in the Expedition 391 methods chapter [Sager et al., 2023]). Preservation is moderate to good in every sample, with varying degrees of

Figure F22. Correlated lithostratigraphy and biostratigraphy, Hole U1575A. Preliminary age determinations are indicated. ? = uncertainty that requires more detailed examination and more samples to increase accuracy and resolution.

overgrowth and etching throughout. Assemblages are moderately diverse except for Sections 391-U1575A-15R-CC through 17R-CC, where assemblages decrease sharply in diversity. This coincides with an inability to confidently assign ages to these samples, which are discussed below.
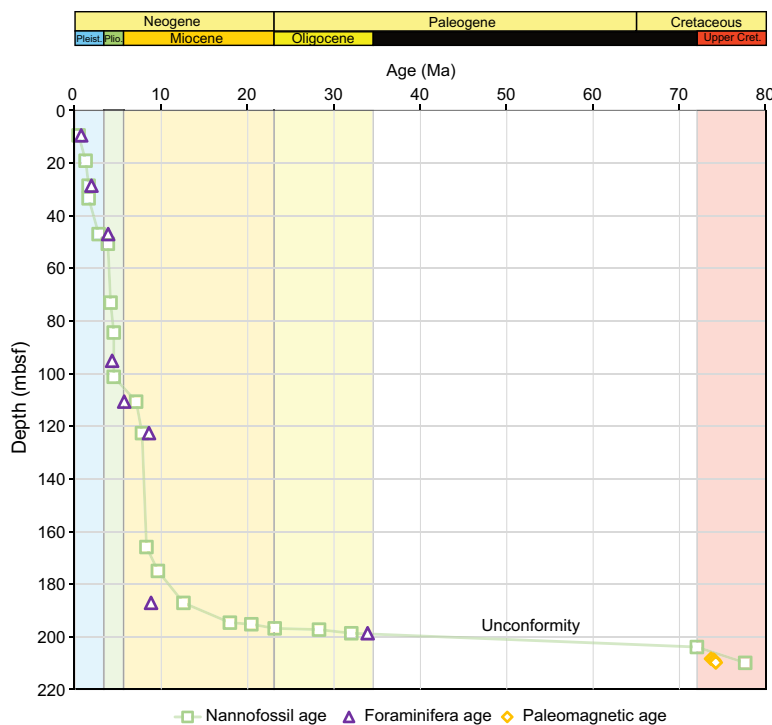

Figure F23. Age-depth model, Hole U1575A.

Table T2. Summary of calcareous nannofossil biozonation, Hole U1575A. T = top, B = bottom. GTS2020 = 2020 geologic timescale (Gradstein et al., 2020), GTS2012 = 2012 geologic timescale (Gradstein et al., 2012). SA = estimate based on shipboard analysis. **Download table in CSV format.**

Core, section, interval (cm)	Epoch	Stage	Stage/age (Ma)	Martini, 1971	Okada Bukry, 1980	Roth, 1978	Marker/age (Ma)	Reference
391-U1575A-								
1R-CC		Ionian	0.129–0.774	NN19/NN20	CN14a/CN14b		T *Pseudoemiliania lacunosa* 0.43	GTS2020
2R-CC	Pleistocene				CN13b		T *Gephyrocapsa* spp. (>5.5 µm) 1.25	GTS2020
3R-CC		Calabrian	0.774–1.806	NN19				
4R-CC					CN13a		T *Calcidiscus macintyrei* 1.60	GTS2020
5R-CC		Piacenzian	2.588–3.600	NN16	CN12a/CN12b		T *Discoaster tamalis* 2.76	GTS2020
6R-CC								
7R-CC				NN15/NN16	CN12a/CN11b		T *Reticulofenestra pseudoumbilicus* 3.82	GTS2020
8R-CC	Pliocene	Zanclean	3.600–5.333					
9R-CC				NN13	CN10c/CN11a		T *Amaurolithus primus* 4.50	GTS2020
10R-CC								
11R-CC		Zanclean/Messinian	4.50*–7.10	NN13-NN11	CN10c/CN9b		Above T absence *R. pseudoumbilicus* 7.10 (?)	SA
12R-CC	Pliocene/Miocene			NN11	CN9b		T absence *R. pseudoumbilicus* 7.10	GTS2020
13R-CC		Tortonian			CN9a		T *Minylitha convallis* 7.78	GTS2020
14R-CC				NN10 (?)	CN8 (?)		Above B common *D. pentaradiatus* <9.37 (?)	SA
15R-CC		Tortonian (?)	7.246–11.608					
16R-CC				NN9/NN10-NN9	CN7/CN8-CN7 (?)		Below B common *D. pentaradiatus* >9.37 (?)	SA
17R-CC								
18R-CC	Miocene	Tortonian		NN9/NN10	CN7/CN8		Between base of common *D. pentaradiatus* and *D. hamatus* 9.37–9.61	GTS2020
19R-CC							T *Discoaster hamatus* 9.61	GTS2020
20R-CC		Tortonian/Serravalian/ Reworked (?)	7.246–13.82	???	???		Possibly mixed; detailed analysis required	Observation
21R-CC	Oligocene	Rupelian	28.09–33.89	CP17/CP16c	NP23/NP22		T *Reticulofenestra umbilicus* 32.02	GTS2012
22R, 1–11	Upper Cretaceous	Campanian	72.05–83.64		CC23	NC20	T *Broinsonia parca parca* 74.59	GTS2012
22R-5, 27–28					CC23/CC22	NC19	T *Eiffellithus eximius* 77.00	GTS2020

5.1.1. Pleistocene to Pliocene

Unit: Lithostratigraphic Unit I
Depth: 0–101.23 mbsf

A fairly continuous succession of Pleistocene through Pliocene sediments is recorded in Sections 391-U1575A-1R-CC through 11R-CC. Trace Cretaceous reworking is observed at the top of this depth interval (Sample 1R-CC) and is easily discernible from in situ assemblages during this period. Sample 1R-CC is bounded by the occurrence of *Pseudoemiliania lacunosa* and the absence of *Helicosphaera sellii*, giving it an age range of 0.43–1.24 Ma. Samples 2R-CC and 3R-CC are constrained by the occurrence of *Gephyrocapsa* spp. (>5.5 μm) with *H. sellii* and the absence of *Calcidiscus macintyrei*, giving it an age range of 1.25–1.60 Ma. Sample 4R-CC is constrained by the occurrence of *C. macintyrei* and the absence of *Discoaster brouweri*, providing an age range of 1.60–1.93 Ma. Sample 5R-CC is constrained by the occurrence of *Discoaster tamalis* and the absence of *Reticulofenestra pseudoumbilicus*, providing an age range of 2.76–3.82 Ma. Samples 6R-CC to 8R-CC are constrained by the occurrence of *R. pseudoumbilicus* and *D. tamalis*, giving an age range of 3.82–4.13 Ma. The presence of *R. pseudoumbilicus* in Sample 6R-CC indicates that the Pleistocene/Pliocene boundary is likely contained in Core 5R or Section 6R-CC. Sample 9R-CC is defined by the highest observed specimen of *Amaurolithus primus*, providing an age of ~4.50 Ma. Samples 10R-CC and 11R-CC provide no new age diagnostic markers. Typical upper Messinian markers such as *Discoaster quinqueramus* are not observed; therefore, these samples are considered to be lower Pliocene (i.e., Zanclean) in age.

5.1.2. Miocene to Oligocene

Unit: Lithostratigraphic Units I and II
Depth: 110.67–198.67 mbsf

The calcareous nannofossil assemblages (Sections 391-U1575A-12R-CC through 21R-CC) proved to be much more complicated than the younger succession. Characterized by possibly large hiatuses, poor recovery, and mixed assemblages, many age determinations are provided with low confidence. High-resolution examination of core sections will be required to discern the best age framework of this section. Even with high-resolution study, the drilling disturbance from rotary coring will provide immense challenges in separating in situ and reworked assemblages. With that in mind, nannofossil assemblages in several core catchers provided remarkably well preserved assemblages of upper Miocene (Tortonian) and Oligocene nannofossils and yield a decent starting age constraint for the bottom half of the sediments at Site U1575.

Sample 391-U1575A-12R-CC is constrained by the disappearance of *R. pseudoumbilicus* and the absence of *Mynilitha convallis*, providing an upper Miocene age range of 7.10–7.78 Ma. Although

Table T3. Summary of foraminifera zonation, Hole U1575A. GTS2020 = 2020 geologic timescale (Gradstein et al., 2020). **Download table in CSV format.**

Core	Epoch	Stage	Stage/age (Ma)	Foraminifera zonation		Reference
				Wade et al., 2011 (with emended M14)	Marker/age (Ma)	
391-U1575A-						
1R	Pleistocene	Chibanian	0.129–0.774	PT1b/PT1a	<0.74	GTS2020
2R						GTS2020
3R	Pleistocene/Pliocene	Chibanian/Gelasian	0.129–2.58	PT1a/PL6	>0.74–<1.93	GTS2020
4R						GTS2020
5R						GTS2020
6R						GTS2020
7R	Pliocene	Zanclean	3.600–5.333	PL2	>3.85–<4.31	GTS2020
9R						GTS2020
10R						GTS2020
12R						Wei, 1994
14R	Miocene	Messinian/Tortonian	5.333–11.608	M14/M13b–M13a	>5.72–<8.58	Wei, 1994
20R				M13a	>8.58–<8.83	GTS2020
21R	Miocene/Oligocene	Aquitanian/Rupelian	20.44–33.89	M2/O1	>22.96–<33.90	Wade et al., 2018

R. pseudoumbilicus disappears in the lowest part of the Messinian (Gradstein et al., 2020), this sample has been assigned to the uppermost Tortonian based on an assemblage that lacks typical Messinian 5-ray discoasters and contains characteristic Tortonian discoasters, namely *Discoaster loeblichii* and *Discoaster calcaris*. The latter taxon is widely used in Gulf of Mexico biostratigraphy for oil drilling operations as a Tortonian bioevent. It is not used as a bioevent here because it lacks context within the 2020 GTS (Gradstein et al., 2020). Sample 13R-CC is constrained by the occurrence of *M. convallis* and is assigned an age of 7.78 to ~8.70 Ma.

Samples 391-U1575A-14R-CC to 17R-CC contain an assemblage change from the previous two core catchers in that many of the discoaster species drop out with an influx of Tortonian biomarker *Reticulofenestra rotaria*, which was not observed above. It is difficult to determine whether this age should be assigned as younger than Samples 12R-CC and 13R-CC, which would require that the first Tortonian ages must be from slumped sediments or some other mass transport. The succession of nannofossil/foraminiferal ooze makes it likely that such a depositional feature would not be picked up in seismic profiles or in depositional features in cores (which are almost completely obscured in this hole throughout the succession of calcareous ooze). However, the persistence of common *Discoaster pentaradiatus* enables us to assign a tentative age of <9.37 Ma for Samples 14R-CC and 15R-CC. *D. pentaradiatus* abundance sharply decreases in Samples 16R-CC and 17R-CC, suggesting that these samples are older than 9.37 Ma, which is an age assigned to the base of common *D. pentaradiatus* (Gradstein et al., 2020).

Sample 391-U1575A-18R-CC contains the stratigraphically highest observed *Discoaster prepentaradiatus* and is constrained by the absence of *Discoaster hamatus*. This sample is tentatively assigned an age of 8.29–9.61 Ma. Sample 19R-CC contains the highest observed *D. hamatus* and is constrained by its entire range of 9.61–10.57 Ma.

It is difficult to assign a confident age to Sample 391-U1575A-20R-CC. Its assemblage still contains *D. hamatus*, but there is an influx of Serravallian fossils such as *Coronocyclus nitescens* and *Cyclicargolithus floridanus*, which should not overlap in typical stratigraphic succession. It is possible that the older taxa are reworked or that a sharp unconformity has brought these assemblages together through time averaging. More samples are needed to properly assess the nature of the complexity.

Sample 391-U1575A-21R-CC contains a large gap in time from the aforementioned late Miocene to the lowest Oligocene (Rupelian), characterized by the occurrence of *Reticulofenestra umbilicus* with an excellently preserved assemblage of typical lower Oligocene nannofossils. Higher sample resolution between Samples 20R-CC and 21R-CC is needed to determine whether there is a condensed or missing section between the samples.

5.1.3. Cretaceous (Campanian)

Unit: Lithostratigraphic Unit III
Depth: 203.8–209.88 mbsf

A small section of pink chalk was recovered from the basal sediments in the deepest core that recovered sediment. Two toothpick samples were analyzed to determine the age of this sediment. Sample 391-U1575A-22R-1, 11 cm, contains a typical late Campanian assemblage, including *Broinsonia parca constricta*, *Broinsonia parca parca*, *Uniplanarius gothicus*, *Uniplanarius trifidus*, and diverse Upper Cretaceous *Prediscosphaera* spp. and *Eiffelithus* spp. (not including *Eiffelithus eximius*). The presence of *B. parca parca* and the absence of *E. eximius* give this sample an age of 74.59–77 Ma. Sample 22R-5, 27–28 cm, contains the stratigraphically highest observed *E. eximius*. The presence of *Uniplanarius sissinghi* and the absence of *U. trifidus* allows this sample to be tentatively constrained between 77 and 78 Ma, making the oldest age of sediment just above basement approximately middle Campanian.

5.2. Planktonic foraminifera

Planktonic foraminifera were examined in a total of 13 core catcher samples. Planktonic foraminifera dominate assemblages in all samples, whereas benthic foraminifera are rare. Very rare

ostracod shells were also observed. Foraminifera range in age from Pleistocene to (possibly) Oligocene. Preservation is generally good, with planktonic individuals exhibiting very low evidence of dissolution and overgrowth. Pleistocene and Pliocene samples contain a low number of test fragments. Fragmentation increases in Sample 391-U1575A-21R-CC, in which most specimen tests were broken.

5.2.1. Pleistocene to Pliocene

Unit: Lithostratigraphic Unit I
Depth: 9.45–95.14 mbsf

Pleistocene fauna were recovered from Samples 391-U1575A-1R-CC and 2R-CC. Planktonic foraminifera assemblages in the aforementioned samples consist of subtropical and temperate forms with abundant *Globoconella inflata* and common *Globorotalia crassaformis*, *Globigerina bulloides*, and *Globorotalia truncatulinoides*. *Globigerinella siphonifera*, *Globorotalia hessi*, *Globorotalia scitula*, *Globigerinoides ruber*, *Neogloboquadrina dutertrei*, and *Trilobatus* spp. occur in lower abundances. Very rare species include *Globorotalia ungulata*, *Pulleniatina finalis*, *Pulleniatina obliquiloculata*, and *Sphaeroidinella dehiscens*. Sediments from Samples 1R-CC and 2R-CC are younger than 0.74 Ma and assigned to Zones PT1b and PT1a based on the presence of *G. hessi* (FO = 0.74 Ma; Gradstein et al., 2020). *Globorotalia tosaensis* was not recovered in Hole U1575A. The Pleistocene/Pliocene boundary was not recognizable due to the absence of the index taxon *Globigerinoidesella fistulosa*.

Planktonic foraminifera in Samples 391-U1575A-3R-CC and 4R-CC include abundant to common *G. inflata* and *G. crassaformis*. Samples also contain a low amount of *G. siphonifera*, *G. scitula*, *P. obliquiloculata*, *G. ruber*, and *Trilobatus* spp. Samples 3R-CC and 4R-CC are dated older than 0.74 Ma but younger than 1.93 Ma based on the absence of *G. hessi* (FO = 0.74 Ma; Gradstein et al., 2020) and the presence of *G. truncatulinoides* (FO = 1.93 Ma; Gradstein et al., 2020).

Samples 391-U1575A-5R-CC to 10R-CC contain lower Pliocene (Zanclean) planktonic foraminifera. *Globoconella puncticulata* and *G. crassaformis* are common components of the assemblage, whereas *Globorotalia margaritae*, *G. scitula*, *G. ruber*, and *Trilobatus* spp. show lower abundances. Few specimens of *Globoconella miotumida* and *Sphaeroidinellopsis kochi* in Samples 6R-CC to 10R-CC were also found in the assemblages. The presence of the aforementioned taxa was considered reworked based on poorer preservation compared with the rest of the assemblage. Index taxa *G. margaritae* and *G. crassaformis* constrain the age of Samples 5R-CC to 10R-CC to between 3.85 Ma (LO *G. margaritae*; Gradstein et al., 2020) and 4.31 Ma (FO *G. crassaformis* sensu lato; Gradstein et al., 2020). Tropical/subtropical index taxa useful to divide the Pliocene–Miocene interval were not recorded at Site U1575.

5.2.2. Miocene

Unit: Lithostratigraphic Unit I
Depth: 110.62–187.14 mbsf

The late Miocene (Messinian–Tortonian) was detected in Samples 391-U1575A-12R-CC, 14R-CC, and 20R-CC. Planktonic foraminifer assemblages in Samples 12R-CC and 14R-CC contain common *G. miotumida*. The identified fauna also include *Globoconella conomiozea*, *Globorotalia* cf. *merotumida*, *Neogloboquadrina acostaensis*, *Globoturborotalita nepenthes*, *Sphaeroidinella seminulina*, and *Globigerinoides extremus*. *G. conomiozea* was tentatively used to provide age constraints for Samples 12R-CC and 14R-CC. Specifically, the sediment was dated older than the FO of *G. conomiozea* (5.72 Ma; Wei, 1994) and younger than its LO (8.58 Ma; Wei, 1994). Planktonic foraminifera in Sample 20R-CC include common *G. miotumida*, *N. acostaensis*, *G. nepenthes*, *S. seminulina*, and *G. extremus*. The core catcher material was dated older than 8.58 Ma (LO *G. conomiozea*) and younger than 8.83 Ma (FO *G. extremus*; Gradstein et al., 2020).

5.2.3. Oligocene

Unit: Lithostratigraphic Unit II
Depth: 198.62–198.67 mbsf

The planktonic foraminifera assemblage in Sample 391-U1575A-21R-CC is highly fragmented and dominated by specimens belonging to the dissolution-resistant genus *Dentoglobigerina* (e.g., *Dentoglobigerina tripartita*, *Dentoglobigerina venezuelana*, and *Dentoglobigerina tapuriensis*). Other species include *Ciperoella anguliofficinalis*, *Globigerinella obesa*, and *Paragloborotalia nana*. The absence of a clear index taxon made it difficult to constrain the age of sediments. The FO (33.90 Ma; Wade et al., 2018) and LO (22.90 Ma; Wade et al., 2018) of *D. tapuriensis* were tentatively used to provide a chronostratigraphic framework for Sample 21R-CC. Calcareous nannofossils provide a better evaluation for the same sample, constraining it to the early Oligocene (Rupelian).

6. Paleomagnetism

6.1. Sediments

6.1.1. Archive-half measurements

Paleomagnetic measurements of the archive halves of sediment RCB cores recovered from Hole U1575A (1R–21R) were conducted using the pass-through superconducting rock magnetometer (SRM) on board the ship. Natural remanent magnetization (NRM) was measured for all sediment cores. The uppermost cores (1R–19R) consist almost entirely of unconsolidated calcareous nannofossil ooze. Because of the soft nature of the ooze and the associated rapid core recovery, we applied a truncated alternating field (AF) demagnetization protocol to these cores, consisting of a single AF demagnetization step (10 mT) following the initial NRM measurements. More consolidated rocks from the base of the sedimentary section (Cores 21R and 22R) were demagnetized at AF levels of 5, 10, 15, and 20 mT after the initial NRM measurements. In all, 75 archive-half sections were measured.

6.1.2. Discrete sample measurements

Discrete samples were collected from unconsolidated sediments using plastic 7 cm^3 Japanese-style sediment cubes, whereas cubic discrete samples from more lithified sediments were prepared using a dual-bladed circular saw. We collected 10 discrete samples from the upper calcareous ooze and 5 discrete samples from the more lithified basal sediments (totaling 15 sedimentary discrete samples). NRM values for cores dominated by calcareous ooze ranged in intensity from 10^{-6} to 10^{-3} A/m. Nearly all of these samples were generally too weak to be successfully measured using the shipboard AGICO JR-6A spinner magnetometer, although such measurements and AF demagnetization were attempted. Unconsolidated sediments from Site U1575 typically had weak magnetizations, often similar to the sample holder intensity of the SRM.

The NRMs of the five lithified basal sediment samples were successfully measured using the spinner magnetometer and ranged 10^{-3} to 10^1 A/m. These samples were subsequently AF demagnetized to at least 60 mT to remove overprints and reveal characteristic remanent magnetizations (ChRMs). The five discrete basal sediment samples generally contained low coercivity overprints that were removed by AF cleaning at 10 mT, which is consistent with being drilling induced (e.g., Acton et al., 2002). Demagnetization to higher AF levels revealed a single underlying magnetization component in each sample, but most of the higher coercivity components were unstable (i.e., maximum angular deviation values obtained from principal component analysis [PCA] were >15°) and not origin trending (although it is unclear whether this means these are not the primary components in the samples or whether a spurious remanence was acquired during AF demagnetization). We could obtain unconstrained best-fit directions for the highest coercivity magnetization component present in two discrete samples (Figure **F24**). We identified both positive and negative inclination characteristic magnetizations, which may be indicative of magnetic polarities if these magnetizations represent primary detrital remanence.

6.1.3. Magnetostratigraphy

Magnetic polarity was interpreted from paleomagnetic inclinations measured after the 10 mT AF demagnetization step for unconsolidated sediments, the 20 mT AF demagnetization step for consolidated basal sediments, and the PCA fit directions obtained from characteristic magnetization components for discrete samples when possible. Only magnetic measurements with intensities

$>10^{-3}$ A/m were included in our magnetostratigraphic analyses to ensure that only high-fidelity magnetization directions were considered.

Because of the weak magnetization intensity of the unconsolidated sediments and the fact that they were only partially demagnetized to 10 mT (which may not have been sufficient to remove drilling-induced magnetization overprints), it was not possible to construct a robust magneto-stratigraphy for Cores 391-U1575A-1R through 19R. Basal sediments provided higher quality magnetic measurements, and we were more confidently able to assign polarity zones within Cores 20R and 21R (Figure **F25**). Although we did not assign any chron labels to Core 21R, the first two sections exhibited normal polarity and the third section displayed reversed polarity. The top of Core 22R contains steeply tilted beds, which suggests that the low (within ~10° of zero) inclinations observed in Sections 22R-1 through 22R-3 are spurious. However, based on correlation with nannofossils constraining the base of Core 22R to the mid-Campanian (see **Biostratigraphy**), we interpret the reversed polarity interval in Sections 22R-4 and 22R-5 as Chron C32r. Just prior to the sediment/basement contact, there is a shift from Chron C32r toward what is likely Chron C33n.

6.1.4. Magnetic properties

Bulk susceptibility and anisotropy of magnetic susceptibility (AMS) measurements were attempted for six discrete samples collected from Cores 391-U1575A-20R through 22R using an AGICO Kappabridge KLY 4 magnetic susceptibility (MS) meter. Measured susceptibility values ranged 1.9×10^{-5} SI to 4.1×10^{-4} SI, although these specific values are unlikely to be robust for two reasons. First, the standard deviation associated with the susceptibility measurements during the AMS experiment was higher than the bulk susceptibility. Second, bulk susceptibility values did not agree between repeated measurements. Therefore, we do not discuss sediment MS values obtained using the KLY 4 susceptibility meter here.

Partial anhysteretic remanent magnetization (pARM) acquisition experiments were conducted on a subset of representative discrete samples that had previously been used for AF demagnetization. pARM was acquired using 5 mT steps up to 60 or 70 mT (Figure **F26**). The pARM acquisition
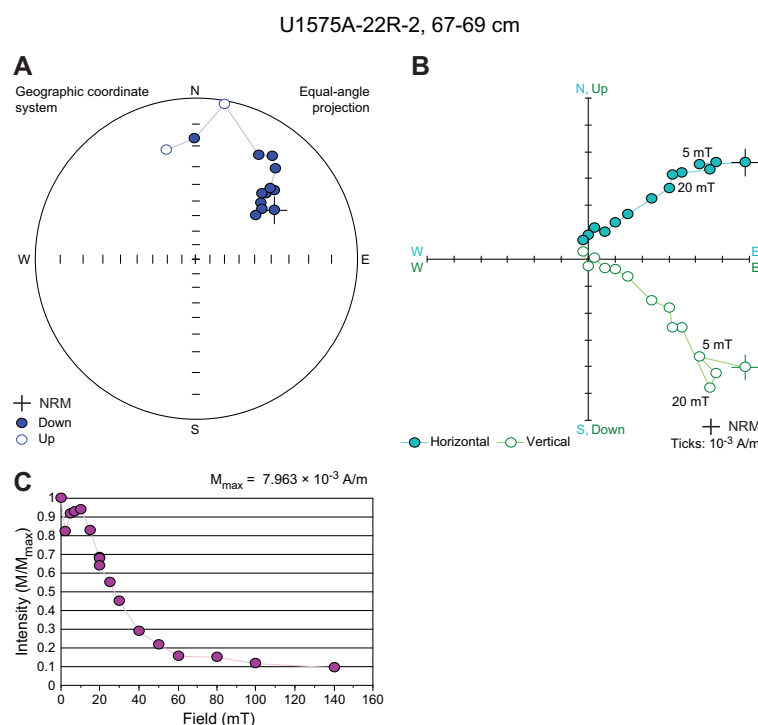

Figure F24. AF demagnetization for a representative sediment sample, Hole U1575A. A. Equal area stereographic projection with direction of magnetization vector at different AF steps. B. Orthogonal vector (Zijderveld) plot with magnetization endpoints plotted on two orthogonal planes. C. Normalized magnetization strength, *M*, at a given AF field demagnetization, normalized by the maximum magnetization strength, M_{max}.

peaks lie between fields of 10 and 15 mT. Our peak values are consistent with those of synthetic magnetite with grain sizes of 3–5 µm for the consolidated sediment and less than 1 µm for the unconsolidated sample (Jackson et al., 1988). Isothermal remanent magnetization acquisition up
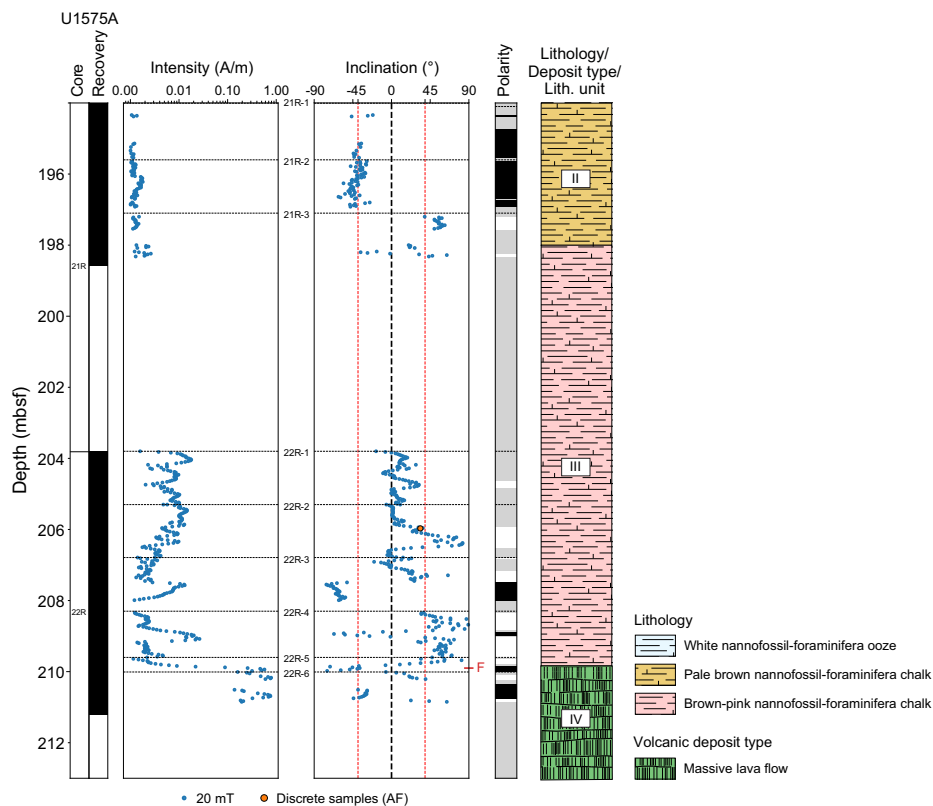
Figure F25. Magnetization intensity and inclination for sedimentary units, Hole U1575A. Inclinations and intensity data for the SRM are shown for the highest demagnetization step of 20 mT, and discrete sample data points show the ChRM inclinations from PCA. Red dashed lines = expected normal and reversed GAD inclination for the current location of the site. Interpreted polarity: black = normal (inclinations >20°), white = reversed (inclinations <20°), gray = inability to assign polarity (for inclinations between ±20° and regions in which no core was recovered). F = contact between basal sediments and the top of the first lava flow.
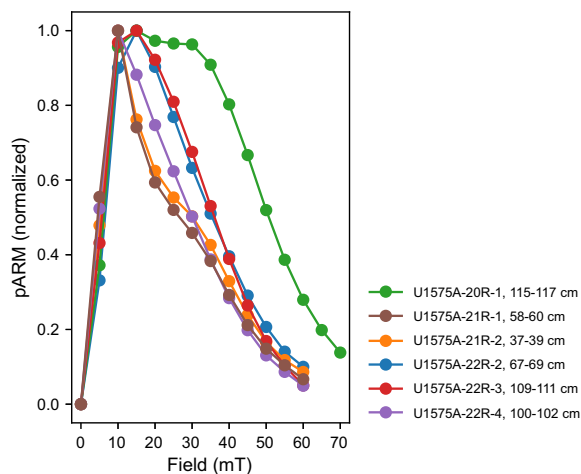
Figure F26. Partial ARM acquisition of six representative consolidated sediment samples, Hole U1575A. Samples were measured with a sliding window of 5 mT in a direct current field of 0.2 mT superimposed on an AF maximum field of 70 mT. Field (mT) = highest field in the interval in which ARM was applied (Jackson et al., 1988). For example, the point at 20 mT is the pARM acquired in the 15–20 mT interval.

to 1 T was measured on two samples from the unconsolidated sediments. Isothermal remanent magnetization saturates by 0.3 T, which suggests that the main magnetic carriers in these samples are dominantly titanomagnetite or titanomaghemite.

6.2. Igneous rocks

6.2.1. Archive-half measurements

Paleomagnetic measurements of the archive halves of igneous cores (391-U1575A-23R through 41R) were conducted using the pass-through SRM on board the ship. In all, 70 archive-half sections were measured.

Most basalts contained low-coercivity overprints that may be drilling induced (e.g., Acton et al., 2002). After AF cleaning to 20 mT, basalts typically exhibited a normal polarity magnetization with an average inclination of −34.7°, only slightly shallower than the expected geocentric axial dipole (GAD) inclination of −38.8°. However, this shallower average inclination may be due in part to a partially remaining drill string overprint, which would bias the samples toward positive inclinations.

6.2.2. Discrete sample measurements

A total of 58 discrete sample cubes (7 cm^3) were taken from the basalts at a frequency of approximately one sample per core section using a dual-bladed circular saw. A total of 37 cubes were subjected to AF demagnetization, and the remaining 21 cubes were subjected to thermal demagnetization. Basalt AF demagnetization spectra of samples from Cores 391-U1575A-22R through 35R are characterized by very high median destructive field (MDF) values (between ~40 and 125 mT), with a few exceptions, suggesting the presence of very high-coercivity magnetic minerals (Figure **F27**). Such high coercivity could be caused by the presence of dendritic iron oxides, which can exhibit a strong magnetic anisotropy due to elongation of individual magnetic grains (Shaar and Feinberg, 2013). Dendritic iron oxides were observed in scanning electron microscopy images of basalts from Hole U1575A (see **Igneous petrology and volcanology**). Sam-
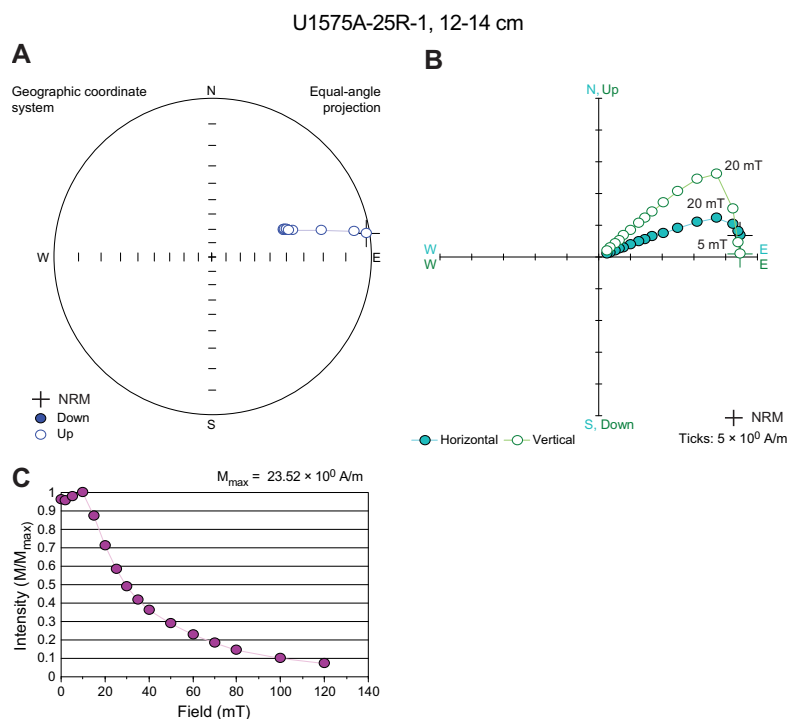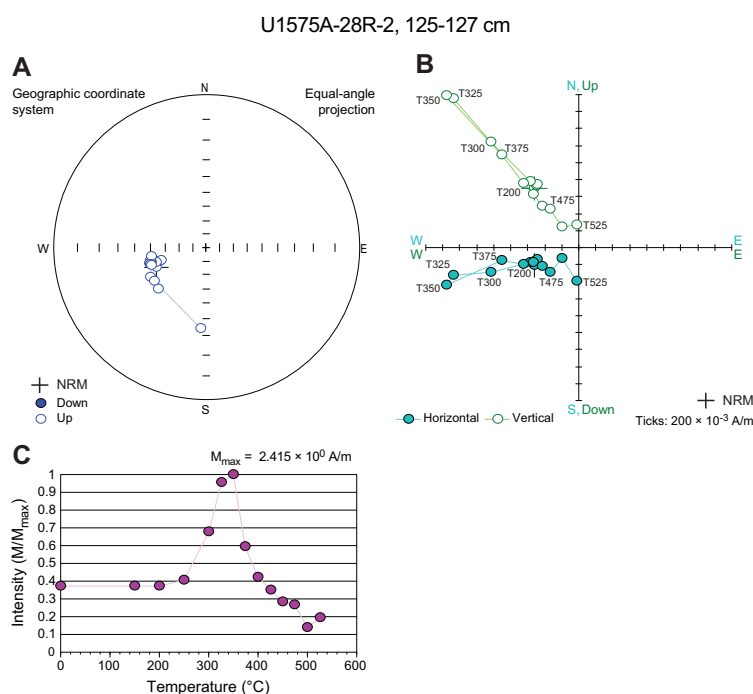

Figure F27. AF demagnetization for a representative basalt sample, Hole U1575A. A. Equal area stereographic projection with direction of magnetization vector at different AF steps. B. Orthogonal vector (Zijderveld) plot with magnetization endpoints plotted on two orthogonal planes. C. Normalized magnetization strength, *M*, at a given AF field demagnetization, normalized by the maximum magnetization strength, M_{max}.

ples from Cores 36R–38R have much lower MDF values (around 5 mT), and those from Cores 39R–41R have MDF values between 25 and 45 mT. After the removal of an overprint (typically by ~20 mT), Zijderveld diagrams for 35 of the 37 samples show a clear unidirectional component trending toward the origin, allowing calculation of a reliable inclination value.

Thermal demagnetization procedures were less successful. Three main behaviors were observed: seven samples were characterized by very low unblocking temperatures (around 150°–200°C), and eight samples (from Cores 391-U1575A-23R through 33R) showed the presence of potential partial self-reversal of magnetization (Figure **F28**). The remaining six samples (from Cores 37R–41R) had unblocking temperatures between about 300° and 450°C. Three thermal demagnetization specimens showed erratic behavior that precluded determination of a ChRM. Good-quality directions (i.e., those with maximum angular deviation values <15° and N > 4 demagnetization steps) were obtained from PCA for 11 samples, whereas for the remaining 7 samples, the PCA fit was of poor quality.

Characteristic components from 51 basalt samples had negative inclinations indicative of normal geomagnetic polarity in the Southern Hemisphere (Figure **F29**). Three samples showed positive inclinations, but two of these inclinations were calculated from poor-quality PCA from thermal demagnetizations. In general, the discrete sample inclinations are in good agreement with the archive-half measurements of inclination after the 20 mT AF demagnetization step (Figure **F29**). The distribution of inclinations calculated from discrete AF and thermal demagnetizations is similar and comparable with the 20 mT AF step measured on archive halves (Figure **F30**). Indeed, most of the discrete AF demagnetizations are of such good quality that the 20 mT AF step already gives the characteristic inclination. Characteristic inclinations were nominally shallower for Cores 391-U1575A-22R through 36R (average inclination = ~38°) than for Cores 37R–41R (average inclination = ~45°); all average inclinations were calculated using the protocol of McFadden and Reid (1982). Inclination characteristic component directions with maximum angular deviation values <15° and N > 4 were used to calculate an overall site mean inclination of 40.0°. Because we did not estimate cooling units, we do not report an uncertainty on this number, calculate a paleolatitude, or estimate the degree to which secular variation is averaged downhole.
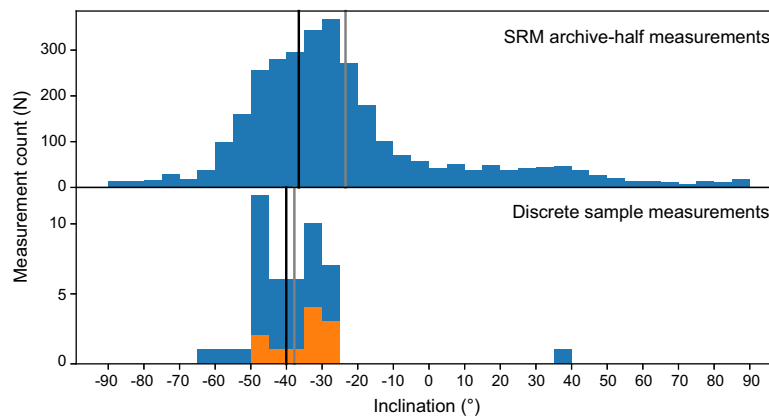

Figure F28. Thermal demagnetization demonstrating partial self-reversal for a representative basalt sample, Hole U1575A. A. Equal area stereonet with direction of magnetization vector at different temperature steps. B. Orthogonal vector (Zijderveld) plot with magnetization endpoints plotted on two orthogonal planes. C. Normalized magnetization strength, M, at a given thermal demagnetization step, normalized by the maximum magnetization strength, M_{max}.

6.2.3. Magnetostratigraphy

All igneous rocks returned directions indicative of normal polarity. As such, magnetostratigraphic division could not be established within the basement. Based on the magnetostratigraphy of the overlying sediment, which makes contact with basement in Chron C33n, it is unclear whether the normal polarity in the igneous rocks is a continuation of Chron C33n or a hiatus occurred at the sediment/basement contact and the basement records Chron C34n (i.e., the Cretaceous Normal Superchron).
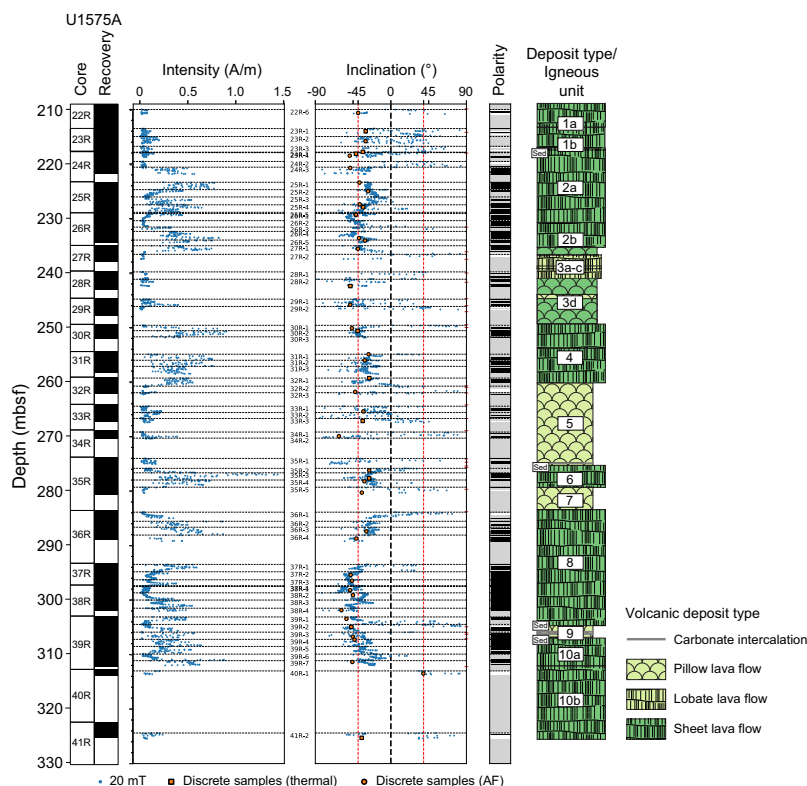
Figure F29. Magnetic intensity and inclination of volcanic units, Hole U1575A. Inclinations and intensity for the SRM data are shown for the highest demagnetization step of 20 mT, and discrete sample data points show ChRM inclinations from PCA. Red dashed lines = expected normal and reversed GAD inclination for the current location of the site. Interpreted polarity: black = normal (inclinations >20°), white = reversed (inclinations <20°), gray = inability to assign polarity (for inclinations between ±20° and regions in which no core was recovered).

Figure F30. Distributions of inclination values for SRM 20 mT data (top) and discrete PCA data (bottom). Blue and orange bars = inclination values from AF and thermal demagnetization data, respectively. Black line = average inclination from the method of McFadden and Reid (1982), gray line = Gaussian average.

6.2.4. Magnetic properties

Bulk MS and AMS were measured on 36 discrete basalt AF demagnetization specimens. Bulk susceptibility values range 1.40×10^{-3} to 7.33×10^{-2} SI. Corrected degree of anisotropy (P') ranges 1.00–1.08. Shape factors (T) range −0.92–0.94. Of 36 basalt specimens, 21 have $0 < T < 1$, indicating that the anisotropy in these specimens is largely controlled by foliation. The remaining 15 specimens have $-1 < T < 0$, indicating that their anisotropy was lineation dominated.

7. Sediment and pore water geochemistry

7.1. Interstitial water chemistry

Interstitial water (IW) was obtained from 32 samples from Site U1575 (1.46–208.19 mbsf) for shipboard analyses. Chemical compositions of these samples were measured according to procedures outlined in **Sediment and pore water geochemistry** in the Expedition 391 methods chapter (Sager et al., 2023). All results are presented in Table **T4** and Figure **F31**.

7.1.1. pH, alkalinity, chloride, and sodium

The pH value of IW at Site U1575 ranges 7.4–7.7. pH is nearly constant with an average of 7.64 ± 0.06 (1σ standard deviation). pH is scattered from the seafloor to ~30 mbsf and appears to be related to calcite dissolution and reprecipitation over the same interval. Excluding one potential outlier at 139 mbsf, pH shows a weak, decreasing trend below ~30 mbsf. IW alkalinity increases from 2.8 mM at 1.5 mbsf to a maximum of 3.0 mM at 12.5 mbsf. Below this maximum, alkalinity gradually decreases to 2.0 mM at 121 mbsf. Farther downhole, alkalinity varies between 1.8 and 2.0 mM. Bicarbonate dissolved in IW may originate from organic matter remineralization and carbonate diagenesis. Using the C/N value range of organic matter found in deep-sea sediment

Table T4. Concentrations of chemical constituents in IW, Hole U1575A. **Download table in CSV format.**
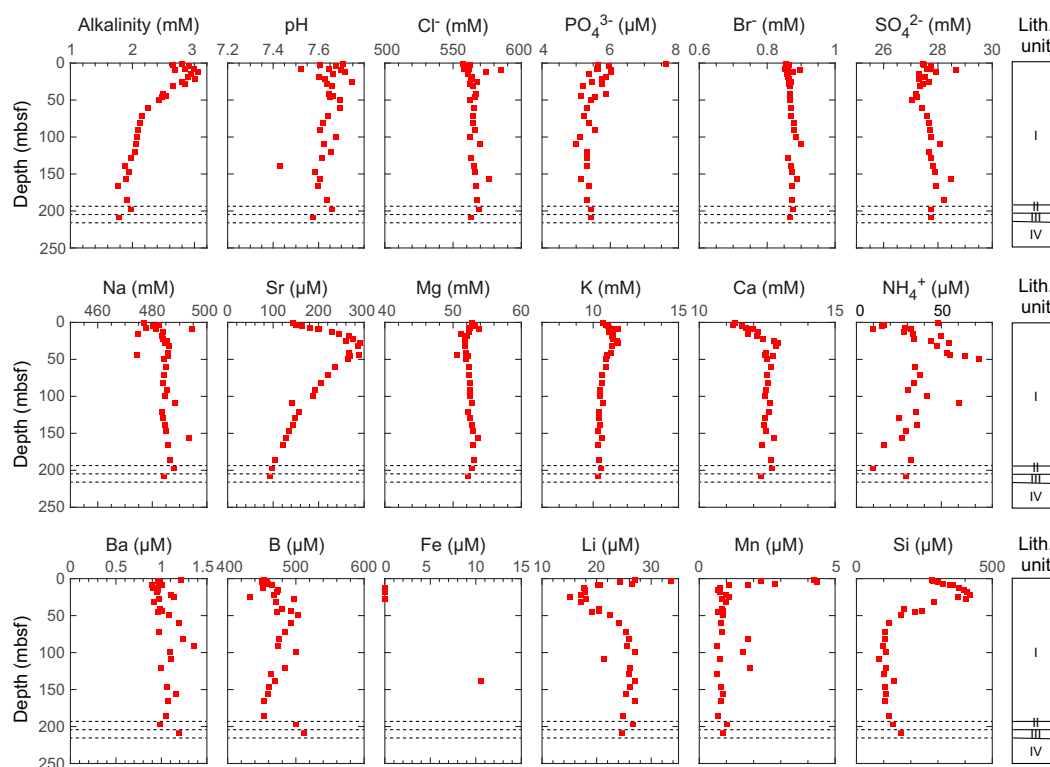
Figure F31. IW alkalinity, pH, chloride, phosphate, bromine, sulfate, sodium, strontium, magnesium, potassium, calcium, ammonium, barium, boron, iron, lithium, manganese, and silicon, Hole U1575A. Unit IV represents the igneous basement.

(11–17) (Baudin et al., 2017) and concentrations of ammonium in the IW, the amount of bicarbonate generated by organic matter diagenesis can be estimated. A 36.3 µM ammonium average concentration for all samples indicates that 396–612 µM of bicarbonate can be generated by organic matter remineralization. Given this value, most bicarbonate appears to originate from carbonate diagenesis, in agreement with the sediment lithology.

IW chloride concentration is nearly constant at Site U1575, varying between 551 and 596 mM. With two potential outliers rejected (at 44.3 and 121 mbsf), the average chloride concentration is 565 ± 5 mM. IW sodium concentration is virtually uniform, ranging 474–494 mM with an average value of 484 ± 4 mM. Average chloride and sodium concentrations are close to average concentrations in the modern ocean (chloride = 559.5 mM; sodium = 480.7 mM) (Quinby-Hunt and Turekian, 1983).

7.1.2. Calcium, magnesium, and strontium

IW calcium concentration increases from 11.3 mM at the seafloor to a maximum of 12.9 mM at 27.8 mbsf. Below this maximum, calcium concentration is relatively uniform with an average of 12.5 ± 0.1 mM. IW magnesium concentration decreases from 52.8 mM at the seafloor to a minimum of 51.7 mM at 27.8 mbsf. Below this depth, IW magnesium concentration shows a gentle increasing trend to a maximum of 53.0 mM toward the base of Lithostratigraphic Unit I, excluding two potential outliers at 44.3 and 156 mbsf. IW magnesium concentration in Units II and III seems to decline based on the only two data points generated, possibly indicating that magnesium deportment is affected by interaction with the basalt basement below Unit III (Gieskes, 1981). The maximum of calcium and the minimum of magnesium at 27.8 mbsf are ~10 m below the alkalinity maximum, suggesting that an increasing trend of calcium and a decreasing trend of magnesium are related to diagenetic calcite formation. Although several hypotheses have been suggested, formation of high-magnesium calcite could be the reason that nearly the same amount of calcium and magnesium was released and consumed. Calcium and magnesium contents decrease in the last two cores above the bottom of the sedimentary sequence, suggesting that these elements might be affected by the basalt basement (Gieskes, 1981).

IW strontium concentration increases from 143 µM just beneath the seafloor to a peak of 290 µM at 27.8 mbsf. Below this depth, strontium concentration steadily decreases to 93.8 µM at 208 mbsf. The strontium maximum at 27.8 mbsf, which coincides with a magnesium minimum observed at Site U1575, could be attributable to biogenic carbonate (likely aragonite) dissolution and the subsequent reprecipitation of inorganic diagenetic high-Mg calcite, a process that rejects strontium (Baker et al., 1982).

7.1.3. Silicon, manganese, sulfate, iron, ammonium, and phosphate

IW silicon concentration at Site U1575 ranges 81.2–418 µM. It increases from 277 µM at the seafloor to 418 mM at 21.9 mbsf and then sharply decreases to 105 µM at 71.8 mbsf. Below this depth to 186 mbsf, silicon concentration is consistent and has a mean of 107 ± 14 µM. Silicon concentration increases in the last two cores above the sediment/basalt contact, possibly due to the release from the basalt basement. The increasing trend of silicon from the seafloor to 21.9 mbsf could be caused by dissolution of biogenic silica, identified in the form of radiolarians in Lithostratigraphic Unit I (see **Lithostratigraphy**). When compared to the dissolved silica concentrations (600–1000 µM) found in other pelagic sediments (Gieskes, 1981), dissolved silica concentrations at Site U1575 are relatively low. This can be explained by the dominance of biogenic calcite at Site U1575.

Manganese concentration rapidly decreases from 4.24 µM near the seafloor to 0.70 µM at 15.5 mbsf. The sharp peak of manganese at shallow depths suggests that Mn(IV)-reducing microbes oxidize organic matter using manganese oxide as electron acceptors under reducing conditions. The manganese peak is shallower than the silica peak, although they are often found at the same depth in pelagic sediment. This offset could be related to the early precipitation of manganese carbonate in the calcite sediment. A manganese reduction interval is followed by a sulfate reduction interval observed at 10–50 mbsf. Iron concentration in IW is lower than the instrumental detection limit in most of the sediment samples. The peaks of phosphate and ammonium are located at 1.5 and 50 mbsf, respectively, in line with the manganese and sulfate reduction zone. A molar ratio of ammonium to phosphate in IW is 7:1.

7.1.4. Lithium, potassium, bromide, boron, and barium

The downhole profile of lithium concentration shows a rapid decrease from 27.0 µM just beneath the seafloor to 15.1 µM at 25.0 mbsf and then an increase to 27.1 mM at 99.6 mbsf. Below this depth, lithium concentrations display a slightly decreasing vertical trend toward the bottom of Unit III and the entire lithium profile mirrors the IW silicon trend. IW potassium concentration is 10.6 mM just beneath the seafloor and increases slightly to 11.5 mM at 27.8 mbsf. The decreasing trend below this depth indicates the interaction of IW potassium with sediment. IW bromide, boron, and barium concentrations show relatively constant depth profiles over the entire sediment succession, with the exception that boron and barium show an increase in the last sample above the basement contact (sampled depth = 208 mbsf), perhaps due to the release of these elements from the underlying basalt lava succession.

7.2. Hydrocarbons in gas phase

Analysis of gas-phase samples was performed for C1–C6 (methane, ethane, propane, butane, pentene, and hexane) for routine safety monitoring in Hole U1575A. Headspace gas, produced by oven heating (at 50°C) ~10 g of sediment in a serum vial, was analyzed per 9.6 m core. The concentration of methane (C1) in 22 headspace samples from Site U1575 was lower than 2.0 µL/L, which corresponds to the atmospheric background level. No hydrocarbon gases higher than C1 were detected.

7.3. Sediment geochemistry

7.3.1. Total carbon, inorganic carbon, and organic carbon

Sediment samples were analyzed to determine the weight percent content of $CaCO_3$, total carbon (TC), total organic carbon (TOC), total nitrogen (TN), and total sulfur (TS). In Hole U1575A, the sampling frequency was approximately two samples per core for Cores 1R–17R, and for deeper cores, one sample was analyzed per core. From 4.5 to 185 mbsf (Lithostratigraphic Unit I), the sediment mainly consists of calcareous ooze and $CaCO_3$ contents that range 92.6–97.9 wt% (mean = 94.9 ± 1.5 wt%). The sample for Unit II in Core 21R and the sample for Unit III in Core 22R have $CaCO_3$ contents of 85 and 74 wt%, respectively. TC values are also consistent from 4.5 to 185 mbsf and range 11.0–11.8 wt% (mean = 11.6 ± 0.2 wt%). Then they rapidly decrease to 10.4 wt% at 197 mbsf (Core 21R) and 9.0 wt% at 208 mbsf (Core 22R) as sediment lithology changes from white nannofossil-foraminifera ooze to pale brown nannofossil-foraminifera chalk with clay. TOC contents vary between 0 and 0.33 wt% (downhole average = 0.17 ± 0.11 wt%) except for the 0.62 wt% found in Core 13R (~123 mbsf). The low TOC contents found in most sediment samples are due to the carbonate-rich lithology of Site U1575. For the same reason, TS and TN contents are below the instrument detection limits for all samples. All results are presented in Table **T5** and Figure **F32**.

Table T5. $CaCO_3$, TOC, and TC contents, Hole U1575A. **Download table in CSV format.**
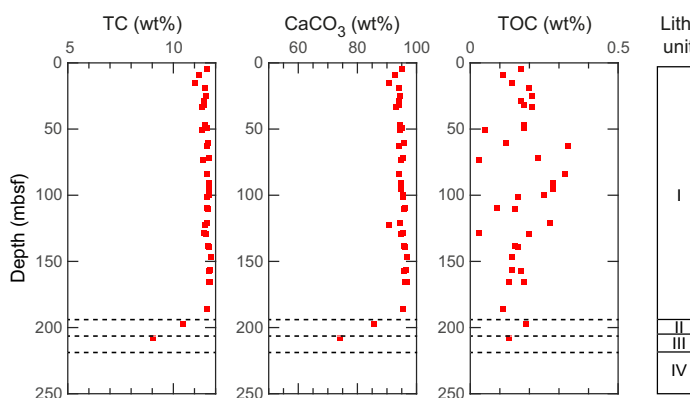
Figure F32. TC, $CaCO_3$, and TOC, Hole U1575A. Unit IV represents the igneous basement.

8. Igneous geochemistry

A set of samples from Site U1575 was chosen for shipboard geochemical analysis to determine major and trace element composition using inductively coupled plasma–atomic emission spectroscopy (ICP-AES). Sample selection was based on lithostratigraphic position, pXRF measurements along the core, and alteration extent (see **Igneous petrology and volcanology**). In total, 33 samples were analyzed using ICP-AES, covering the depth range from 210.22 mbsf (Sample 391-U1575A-24R-2, 101–103 cm) to 324.52 mbsf (Sample 41R-2, 46.8–48 cm). The selected samples provide a representative overview of the recovered lithologies from Hole U1575A, which can be briefly summarized as follows:

- Igneous Subunits 1a and 1b: three basaltic samples from highly phyric plagioclase-pyroxene-olivine massive lava flows.
- Igneous Subunits 2a and 2b: 10 basaltic samples from moderately to highly phyric plagioclase-pyroxene-olivine massive flows.
- Igneous Subunits 3c and 3d: two samples from a sequence of alternating pillow, lobate, and sheet lava flows with sparsely to highly phyric plagioclase-pyroxene-olivine basalts.
- Igneous Subunits 4a and 4b: four sparsely phyric plagioclase-pyroxene-olivine basaltic samples from massive flows.
- Igneous Unit 5: four sparsely to moderately phyric plagioclase-pyroxene basalts from pillow, sheet, and lobate flows.
- Igneous Units 6–9: seven samples from an alternating sequence of massive and pillow lava flows with sparsely to highly phyric plagioclase-pyroxene-olivine basalts.
- Igneous Subunits 10a and 10b: three basaltic samples from the moderately to highly phyric plagioclase-pyroxene-olivine massive lava flow.

For all samples, major and trace element compositions were analyzed using ICP-AES and pXRF. Detailed sample preparation, analytical procedures, standard analyses, calibration, and drift corrections are reported for both methods in **Igneous geochemistry** in the Expedition 391 methods chapter (Sager et al., 2023). The total sums of the major element oxides in weight percentages acquired using ICP-AES range 97.14–102.32 wt% except for six samples that have unusually low values from 90.40–95.42 wt% (Table **T6**). The reason only some samples have low totals is unclear, but it is most likely due to sample preparation issues and problems with the bead sampler (see **Igneous geochemistry** in the Expedition 391 methods chapter [Sager et al., 2023]). In the following sections, we do not consider these samples further, but we do display them as small crosses (or yellow dots) on the figures.

The major element oxide concentrations measured using ICP-AES were normalized to 100% on a volatile-free basis, and total iron was recalculated as $Fe_2O_3^t$ (Table **T6**). The normalized values, omitting effects of variable alteration on major elements, are used for an improved comparison between the Site U1575 data and literature data from previous drill and dredge sites along the submarine TGW hotspot track (e.g., Le Maitre, 1962; Richardson et al., 1984; Weaver et al., 1987; Le Roex et al., 1990; Cliff et al., 1991; Willbold and Stracke, 2006; Class and le Roex, 2008; Salters and Sachi-Kocher, 2010; Rohde et al., 2013; Hoernle et al., 2015; Homrighausen et al., 2018, 2019).

A total of 128 pXRF measurements were conducted on archive-half sections of the basalt lava succession in Hole U1575A (Table **T7**). In general, each point was analyzed twice to account for analytical error. ICP-AES powders were also analyzed using pXRF with the same methodology as applied to the section-half measurements (Table **T8**). Drift was monitored by running the BHVO-2 standard intermittently throughout the analytical process, and no instrumental drift was detected (see Table **T10** in the Expedition 391 methods chapter [Sager et al., 2023]).

Table T6. Major and trace element abundances determined by ICP-AES, Hole U1575A. **Download table in CSV format.**

Table T7. Major and trace element abundances determined by pXRF on archive halves, Hole U1575A. **Download table in CSV format.**

8.1. Comparison of ICP-AES and pXRF results

The ICP-AES and pXRF results display good to excellent linear correlation coefficients between the two methods (Figure **F33**), with R^2 = 0.92–0.96 for TiO_2, K_2O, $Fe_2O_3^t$, Y, and Zr and moderate values of R^2 = 0.84 for Ni. The weaker correlation for Ni is most likely related to a high relative standard deviation of ICP-AES measurements. The difference between the two methods is relatively small, with less than ±10% for K_2O, Ni, Y, and Zr. In contrast, pXRF results are systematically higher for TiO_2 by ~16% and lower for $Fe_2O_3^t$ by ~18% than those obtained from ICP-AES. This discrepancy is probably due to the secondary fluorescence effect in pXRF caused by Fe atoms, which decreases the $Fe_2O_3^t$ value compared to the actual value and increases the value of elements with masses lower than iron. V values obtained using pXRF are not considered because the V concentration of the samples is close to the detection limit of pXRF. For elements lighter than K, absorption and scattering have a significant effect on pXRF measurements, so data for these elements are not discussed here. There was no difference in the measured values of powders correlating with the amount of powder used for pXRF analysis (Figure **F33**).

8.2. Alteration

Loss on ignition (LOI) is an indicator of the degree of alteration. For the Site U1575 samples, 26 of 27 samples have relatively low LOI values of <1.51 wt% (LOI = 2.62 wt% for the remaining sample). Samples with petrographic evidence for alteration, compared to less altered samples in the same unit, have overall higher fluid mobile element concentrations, such as K_2O and Sr (Table **T6**), which is a common effect of seawater alteration (e.g., Jochum and Verma, 1996). Overall weaker correlations of Zr versus K_2O and Sr (R^2 = 0.17 and 0.74, respectively) compared to Zr versus TiO_2

Table T8. Major and trace element abundances determined by pXRF on working halves, Hole U1575A. **Download table in CSV format.**
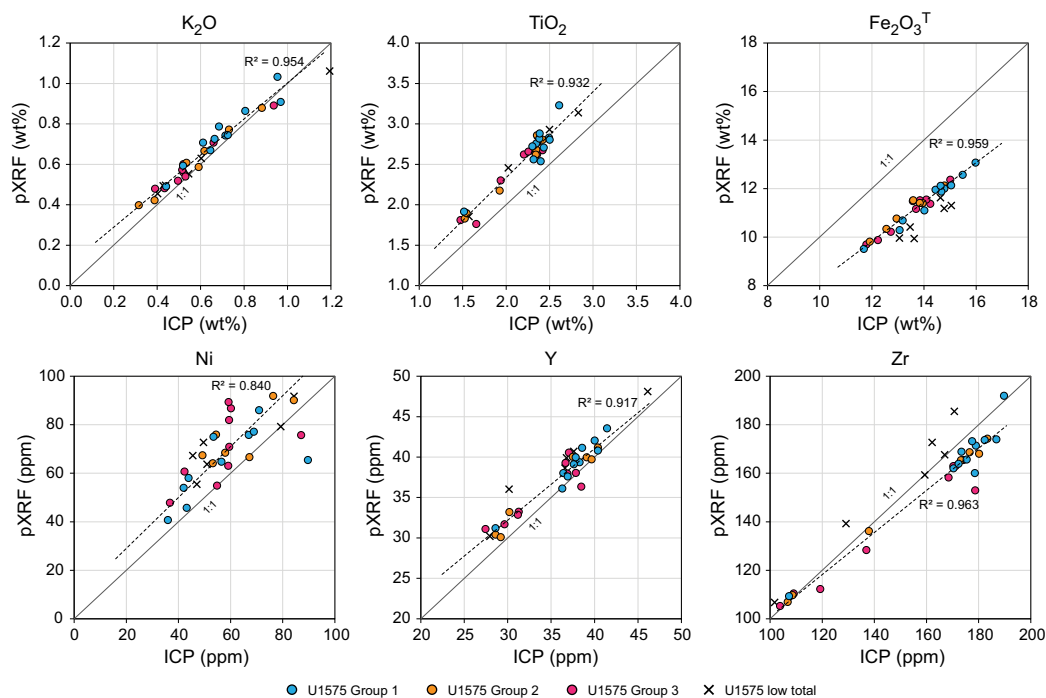
Figure F33. pXRF and ICP-AES results obtained on the same sample powder, Hole U1575A. Data were divided into four groups based on the amount of powder used for pXRF measurement or the measured totals: Group 1 (1 cm thick powder), Group 2 (0.3–1 cm thick powder), Group 3 (<0.3 cm thick powder), and Group 4 (totals < 96 wt%). Black dotted line = regression line for samples, excluding those with low totals. Gray line is the y = x line. Samples plot on this line if ICP-AES and pXRF contents are identical. Regardless of the sample amount, pXRF and ICP-AES data for both major and trace elements form positive trends with good correlation. ppm = µg/g.

or Y (R^2 = 0.94 and 0.99, respectively) could support this assumption. Because LOI (<1.5 wt%) and K_2O values (<1 wt%) are overall low, enrichment of K_2O is likely to be relatively small. Therefore, the total alkali versus silica classification after Le Bas et al. (1986) can be used to give an idea of the sampled rock type.
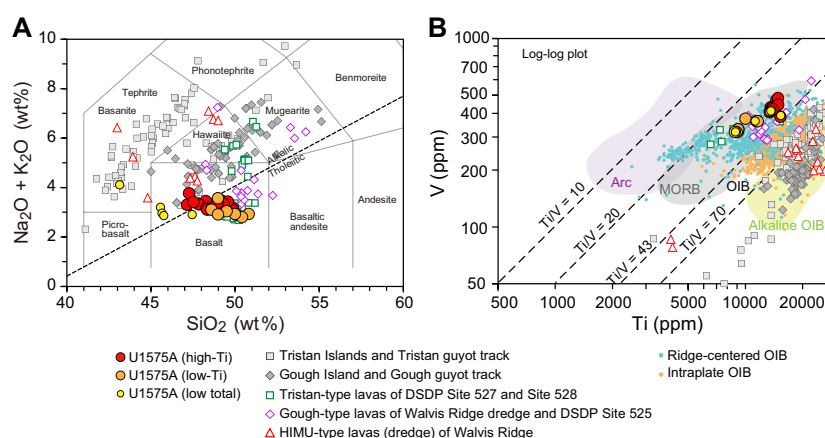
8.3. Classification

According to the total alkali versus silica classification, all recovered samples are basalts (Figure **F34A**) and lie within the compositional range of previously reported rocks from Walvis Ridge (Richardson et al., 1984; Salters and Sachi-Kocher, 2010; Hoernle et al., 2015; Homrighausen et al., 2019). Site U1575 samples straddle the alkalic/tholeiitic boundary, with the low-TiO_2 lavas plotting in the tholeiite field and the high-TiO_2 lavas trending from the tholeiite field into the alkali basalt field (Figure **F34A**). Other samples from the same plume system from Gough Island, Gough guyot track, other Walvis Ridge dredge sites, and DSDP sites are variably fractionated from basalt to hawaiite to mugearite (Le Maitre, 1962; Richardson et al., 1984; Weaver et al., 1987; Willbold and Stracke, 2006; Salters and Sachi-Kocher, 2010; Rohde et al., 2013; Hoernle et al., 2015; Homrighausen et al., 2019). In contrast, samples from the Tristan Island group are dominantly basanites fractionated to phonotephrites and phonolites (le Roex et al., 1990; Cliff et al., 1991; Willbold and Stracke, 2006).

On the Ti versus V classification diagram after Shervais (2022), all basalt lavas from Site U1575 lie within the mid-ocean ridge basalt (MORB) array and overlap the field of ridge-centered ocean island basalt (OIB) (Figure **F34B**). The intermediate Ti/V values between 27 and 40 are similar to the previously reported tholeiitic EMI-type (Zindler and Hart, 1986) lavas from Walvis Ridge and Walvis Ridge DSDP drill sites, which are interpreted to result from plume-ridge interaction (e.g., Richardson et al., 1984; Gibson et al., 2005; Hoernle et al., 2015; Homrighausen et al., 2019). In contrast, the late-stage or rejuvenated high μ (HIMU), or high time-integrated $^{238}U/^{204}Pb$ mantle with radiogenic Pb isotope ratios (Zindler and Hart, 1986), rocks from Walvis Ridge and EMI-type samples from the islands and Guyot Province have overall higher Ti/V values and lie within the OIB array or intraplate setting.

8.4. Bivariate element plots

Basaltic rocks from Site U1575 have normalized SiO_2 values of 47.1–50.8 wt% and MgO contents of 4.98–7.15 wt% (Table **T6**). On bivariate diagrams of MgO (or Mg#) versus other major and trace


Figure F34. A. Total alkali vs. silica classification (Le Bas et al., 1986) showing that all Hole U1575A samples measured using ICP-AES are basalts straddling the alkalic/tholeiitic boundary (MacDonald and Katsura, 1964). B. Ti vs. V classification after Shervais (2022) showing that all basaltic lavas from Hole U1575A lie within the MORB field and overlapping field of ridge-centered OIB similar to EMI-type samples from Walvis Ridge. In contrast, all island and Guyot Province samples and late-stage HIMU-type samples fall in the OIB and alkaline OIB fields. ppm = μg/g. Data sources: Le Maitre, 1962; Richardson et al., 1984; Weaver et al., 1987; Le Roex et al., 1990; Cliff et al., 1991; Gibson et al., 2005; Willbold and Stracke, 2006; Class and le Roex, 2008; Salters and Sachi-Kocher, 2010; Class and Lehnert, 2012; Rohde et al., 2013; Hoernle et al., 2015; Homrighausen et al., 2018, 2019.

elements, the samples from Site U1575 form clusters that overlap with previous data from Walvis Ridge and Guyot Province (Figure **F35**). The only good correlation is a negative trend between MgO and K_2O with $R^2 = 0.63$, whereas the remaining elements have best-fit lines of $R^2 < 0.40$. $Fe_2O_3{}^t$ seems to increase with decreasing MgO, however, as is expected for fractional crystallization of the major ferromagnesian phenocryst phases olivine and clinopyroxene (observed in the majority of igneous units) (see **Igneous petrology and volcanology**). The olivine fractionation trend is not confirmed in the MgO versus Ni plot (Figure **F35**), possibly due to the high relative standard deviation values of ICP measurements. Plots of Mg# versus Ti, Zr, Sr, and V (not shown) show curvilinear trends consistent with fractional crystallization, although the offset of high- and low-TiO_2 lavas indicates differences in primary magma compositions.
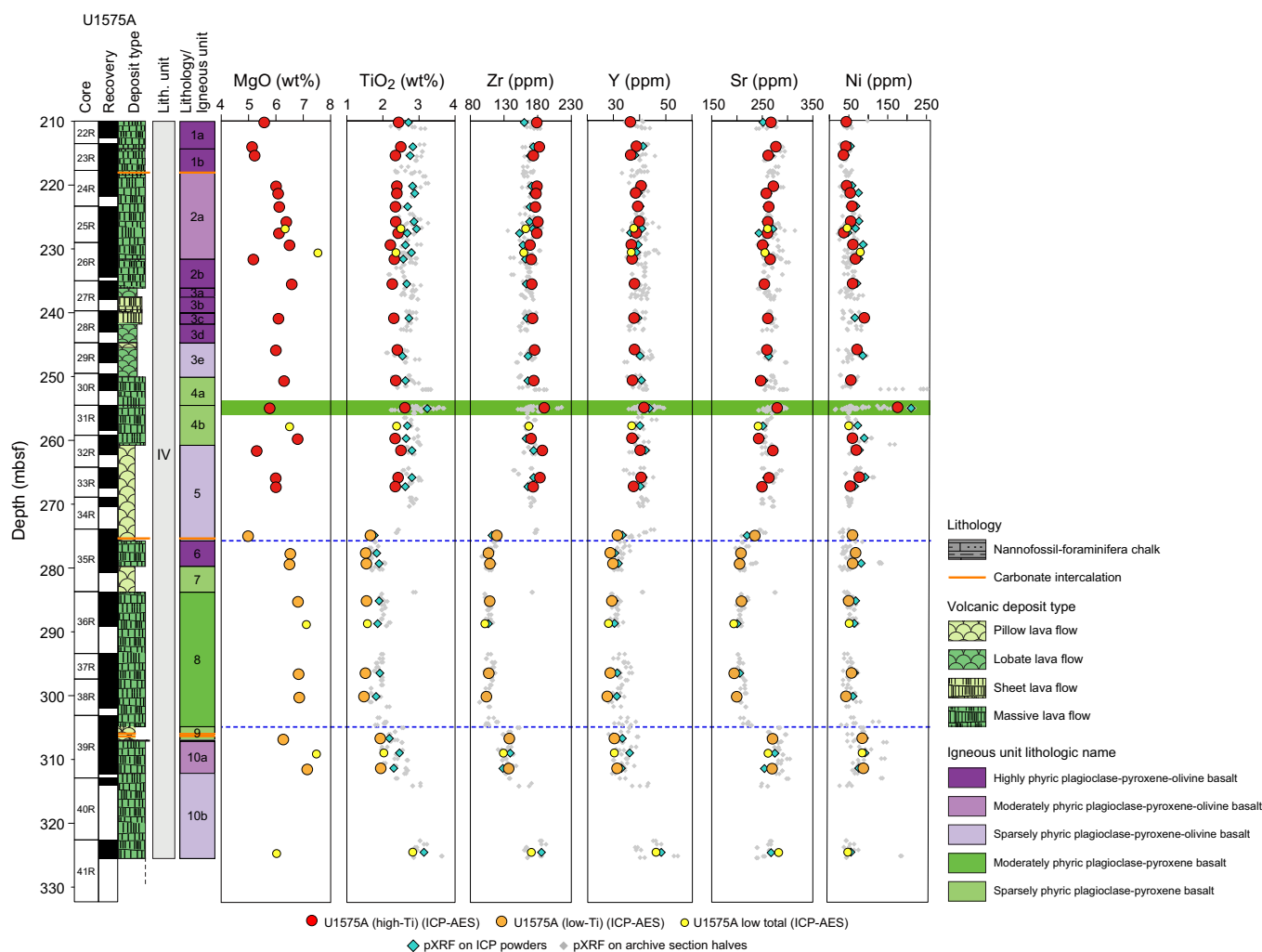
8.5. Downhole variations

The geochemical data display some remarkable characteristics downhole. MgO content seems to increase slightly as depth increases (Figure **F36**), whereas SiO_2 values display a relatively broad scattered array (not shown), possibly related to the lower accuracy of SiO_2 compared to MgO. These same systematics are also observed within some igneous units. In Igneous Unit 2, for example, MgO contents seem to systematically increase with depth (apart from slightly altered Sample 391-U1575-26R-3, 9–11 cm, which has low MgO [5.17 wt%] at 231.65 mbsf), whereas SiO_2 content displays a scattered array (not shown). A similar trend could be observed in Igneous Units 6–10 with a correlated increase of MgO and slight decrease of SiO_2 with depth, which could reflect derivation through time from an evolving magma body.

The most pronounced downhole variation, however, occurs at ~274 mbsf at the bottom of Igneous Unit 5 (~1.5 m above the transition between Igneous Units 5 and 6). Although TiO_2 content remains relatively constant between 2.20 and 2.50 wt% in the upper part of the recovered core (<274 mbsf), the TiO_2 value suddenly drops to 1.66 wt% in the lower portion of Unit 5 (Figure **F36**). This low-Ti signature remains relatively constant, with TiO_2 values between 1.48 and 1.54 wt% throughout Units 6–8, and then it slowly increases again through Unit 9 to contents similar to Units 1–5. This downhole Ti variation is clearly mirrored by a similar pattern in Zr, Sr, and Y concentrations and possibly to a lesser extent in $Fe_2O_3{}^t$, K_2O, P_2O_5, Cu, and Zn contents (Figure **F36**; Table **T6**). The significant geochemical transition at ~274 mbsf also seems to be coupled with a sudden increase in Mg# and, to a lesser extent, CaO (Table **T6**). It is important to note that the low-Ti signature starts within Unit 5 (Sample 391-U1575A-35R-1, 98.5–99.5 cm, at 274.89 mbsf) and not at the interface between lithologically distinct units. Interestingly, the low-Ti signature is coupled with a mineralogical change to dominantly olivine free and consistently lower plagioclase and clinopyroxene phenocryst proportions (see **Igneous petrology and volcanology**). Mineralogical variations in other core sections, however, cannot be clearly correlated with other geochemical variabilities, such as the MgO increase in Unit 2.
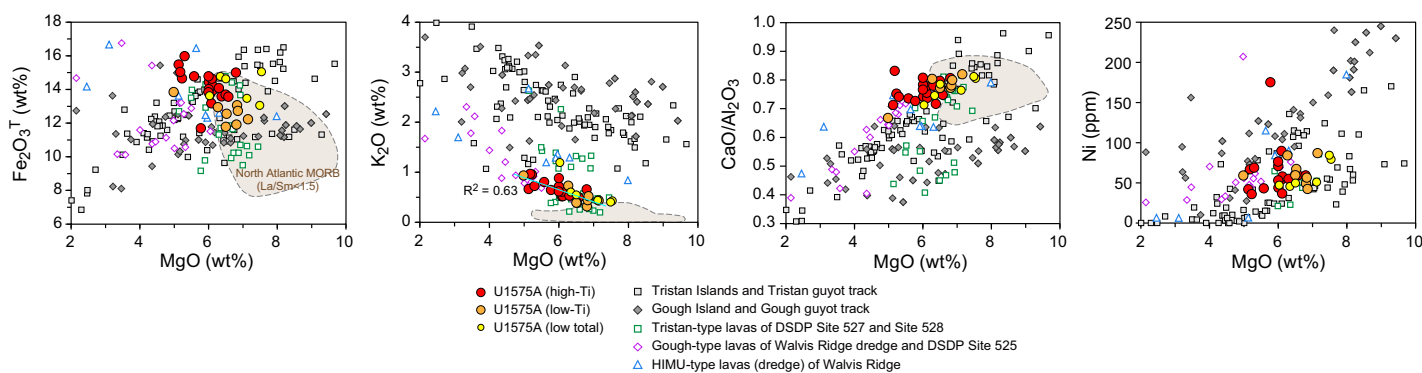
Figure F35. MgO vs. $Fe_2O_3{}^t$, K_2O, CaO/Al_2O_3, and Ni for data from basalts from Hole U1575A. Major element compositions are normalized to 100 wt% totals. Brown area = range of North Atlantic MORB compositions with La/Sm < 1.5. Samples overlap with previous samples. Only K_2O correlates well with MgO ($R^2 = 0.63$), whereas other major oxides (e.g., $Fe_2O_3{}^t$) and ratios of major oxides (e.g., CaO/Al_2O_3) form weak correlations or clusters. ppm = µg/g. Data sources: Le Maitre, 1962; Richardson et al., 1984; Weaver et al., 1987; Le Roex et al., 1990; Cliff et al., 1991; Gibson et al., 2005; Willbold and Stracke, 2006; Class and le Roex, 2008; Salters and Sachi-Kocher, 2010; Class and Lehnert, 2012; Rohde et al., 2013; Hoernle et al., 2015; Homrighausen et al., 2018, 2019.

Figure F36. Downhole chemical variations, Hole U1575A. Select elements measured using ICP-AES in comparison to pXRF data on the same powders and on archive-half sections. Superimposed on a broad increase in MgO is an excursion to high TiO_2-Ni-Cu in Igneous Unit 4 (green band), as well as abrupt changes in composition toward the bottom of Unit 5 and, less pronounced, at the top of Unit 9 (dashed lines). ppm = μg/g.

Another remarkable geochemical signature is observed at the bottom of a single massive (~5 m) flow (Igneous Subunit 4a) at ~255 mbsf (Figure **F36**), which is characterized by a sudden increase in TiO_2, CaO, Mg#, Ni, Cu, and Sc coupled with a drop in $Fe_2O_3^t$ content recorded by the pXRF surface data and confirmed by a single sample (391-U1575A-31R-1, 40–42 cm) using pXRF on powder and ICP-AES (Tables **T6**, **T7**). Less pronounced but still significant is a change in composition at the top of Unit 9, which is gradual for most elements, but Sr and Zr show a clear increase, possibly coupled with a small increase in TiO_2, Y, and Ni, although to a lesser extent.

At Site U1575, the first 17 samples were measured for S content using the CHNS analyzer. The S content in these basalt samples, however, is below the detection limit of the CHNS analyzer. An additional experiment was conducted with a sample of 100 mg, seven times the initial measurement, but again no S was detected. Going forward, we decided not to measure S content at the other sites.

9. Physical properties

Physical properties measurements were made on recovered whole-round sections, section halves, and discrete cube and wedge samples from Site U1575 in the core laboratory. Hole U1575A was cored to ~325 mbsf. Based on physical properties measurements, the recovered interval is initially

described as three distinct lithostratigraphic units: calcareous ooze, chalk, and igneous basement. Abrupt shifts in gamma ray attenuation (GRA), moisture and density (MAD) bulk density, and natural gamma ray (NGR) data indicate the sedimentary/igneous contact at ~210 mbsf. Within the sedimentary package, NGR and MS peaks at ~194 mbsf correlate to the calcareous ooze/chalk contact (Figure **F37**). Physical properties measurements do not appear to distinguish the lithologic boundary between chalk Lithostratigraphic Units II and III at ~199 mbsf (see **Lithostratigraphy**).

At several intervals in the igneous basement (from ~210 mbsf to the bottom of the hole), NGR values and a decrease in GRA bulk density indicate the presence of highly fractured and/or rubbly intervals versus coherent basalts (>20 cm in length). Because submarine-inflated pahoehoe flows do not share the same morphological characteristics as their subaerial equivalents (e.g., highly vesicular, fractured, and shelly flow tops), it is likely that rubbly zones indicate drilling disturbance rather than contacts between individual basalt flows. However, at several depth intervals, MS data appear to correlate to geochemical variations, notably a shift from high to low TiO_2 concentrations in basalts at ~270 mbsf made evident by decreases in MS at the same depth.

9.1. Data acquisition

Each whole-round core was measured for GRA bulk density, *P*-wave velocity (*x*- and *y*-axis), and MS on the Whole-Round Multisensor Logger (WRMSL) and NGR on the Natural Gamma Radiation Logger (NGRL). Thermal conductivity measurements were obtained from whole-round sediment cores containing ooze, and point magnetic susceptibility (MSP) measurements of section halves were obtained using the Section Half Multisensor Logger (SHMSL). More localized measurements (thermal conductivity, MAD, *P*-wave logger, and *P*-wave caliper [PWC]) of section halves and discrete samples were taken within each representative sedimentary and igneous unit, often multiple samples per core. The higher resolution sampling plan was implemented to identify and track variations in physical properties with depth for correlation to lithologic, magnetic, and chemical characteristics (see **Lithostratigraphy** and **Igneous petrology and volcanology**).

For Hole U1575A, a subset of measurements was conducted on paleomagnetic cube saw residue wedges to determine the effects of high-temperature (>500°C) thermal demagnetization experiments on physical properties measurements such as MAD and *P*-wave velocity. Following heating, hard rock paleomagnetic cube samples and saw residue wedges from the same offset depth were
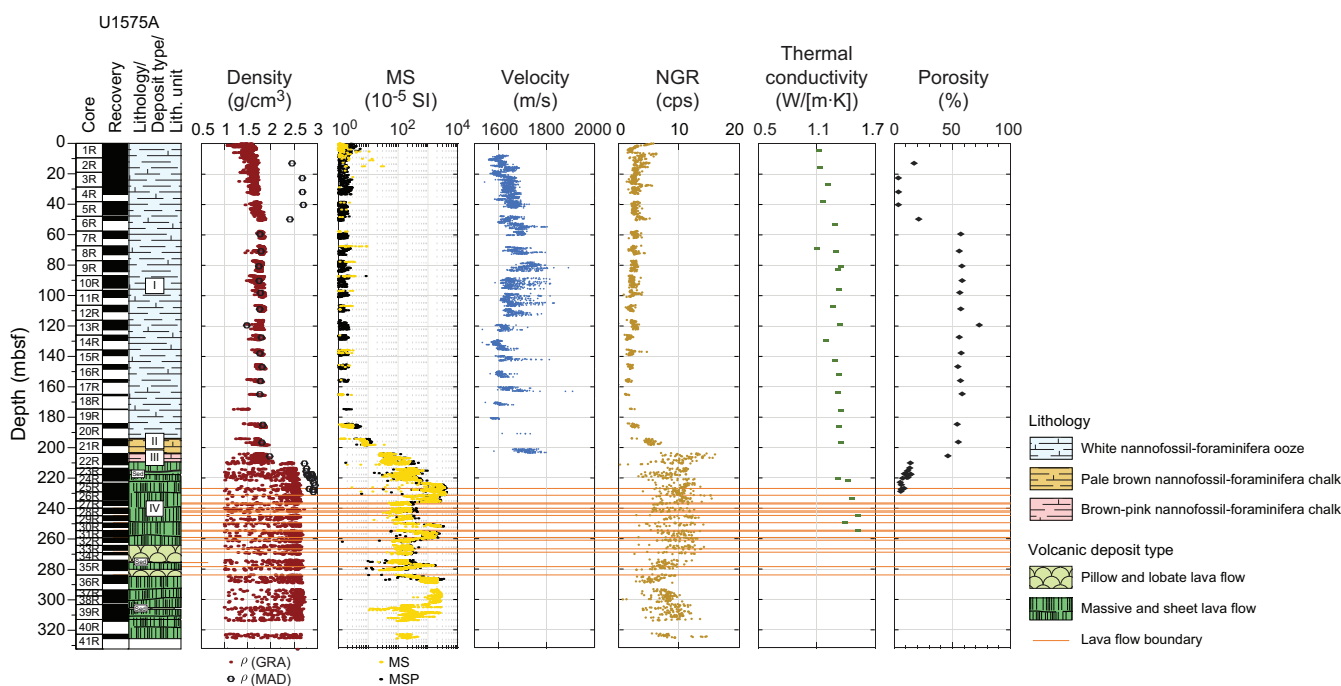

Figure F37. Physical properties, Hole U1575A.

prepared using standard physical properties methods (see **Physical properties** in the Expedition 391 methods chapter [Sager et al., 2023]). MAD and PWC measurements were collected for the thermal demagnetization cube samples (PWC for the *x*-, *y*-, and *z*-axes) and the control wedges (PWC for the *z*-axis) to determine whether thermal demagnetization changes these properties. At the time of this publication, this experiment is in progress.

9.2. Thermal conductivity

Within the sedimentary units, mean thermal conductivity for Hole U1575A varies between ~1.10 and ~1.53 W/(m·K) with a mean of 1.31 ± 0.11 W/(m·K) (1σ standard deviation, used throughout) (Figure **F37**; see **Lithostratigraphy**). Values are fairly consistent over the entire section but increase gradually downward through the sediments. Across the sediment/basement interface, mean thermal conductivity increases slightly from ~1.40 to ~1.53 W/(m·K), a change that likely reflects variations in mineralogy, compaction, and porosity across the unit boundary. From ~210 mbsf to the bottom of the hole, measurements of igneous basement yield thermal conductivity values of ~1.48 to ~1.76 W/(m·K) with a mean of 1.58 ± 0.09 W/(m·K) and exhibit greater variation than the sediment section above. The range in values is attributed to varying degrees of vesicularity and alteration in basalt flows, as well as observed differences agree with other physical properties measurements at the same depth intervals (e.g., NGR and MS).

9.3. Density and porosity

Measurements of MAD bulk density generally agree with GRA bulk density data (Figure **F37**). Both MAD and GRA bulk density values are consistent in the uppermost ~194 mbsf, with average values of ~1.98 ± 0.39 g/cm^3 and 1.71 ± 0.10 g/cm^3, respectively. Below this interval, GRA bulk density values increase to a mean of ~2.58 g/cm^3 ± 0.046 g/cm^3 with a much larger range (2.50–2.73 g/cm^3). The increase in density and associated scatter are attributed to lithologic variations (rubbly versus coherent basalt) and align with other physical properties trends, such as NGR values.

Porosity calculations derived from MAD measurements are fairly consistent in the calcareous ooze unit between ~58 and ~197 mbsf, with a mean value of 55.9 ± 12.5 vol%. The uppermost five porosity measurements, from the seafloor to ~47 mbsf, were disregarded due to experimental error. Below 197 mbsf, porosity decreases slightly to a mean of 49.2 ± 6.6 vol% within the chalk. From ~210 mbsf to the bottom of the hole, porosity values significantly decrease to a mean of 8.58 ± 9.5 vol%, consistent with slightly to moderately vesicular basalts (see **Lithostratigraphy**). Porosity variations below ~210 mbsf may be related to vein fillings or alteration in massive basalt intervals.

9.4. Magnetic susceptibility

MS pass-through and MSP values measured using the SHMSL are in good agreement along the entire interval of Hole U1575A. MSP measurements plotted by depth show the same overall trends. Both data sets, recorded in instrument units, increase very gradually from the seafloor to ~223 mbsf. Above this depth, both sets of MS measurements are relatively constant and are rather low (average = 67.0 × 10^{-5} ± 0.31 × 10^{-5} SI). Below ~223 mbsf, MS and MSP values increase sharply from ~200 × 10^{-5} to ~3000 × 10^{-5} SI and appear to correlate with fragmented basalt in the uppermost igneous section of the hole. Interestingly, the rapid increase in MS and MSP values does not occur at the sediment/igneous contact at ~210 mbsf; it instead occurs ~13 m below that. From ~223 mbsf to the bottom of the hole, MS values show further variation. The highest recordings, ~3000 to ~3600 × 10^{-5} SI, are found between ~229 and ~231 mbsf in Sections 26R-1 and 26R-2. This interval of higher magnetism is also represented in SRM measurements, which increase from ~1−5 A/m to ~9−13 A/m in the same interval (see **Paleomagnetism**). Zones of low MS and MSP values appear to correlate with intervals of highly fragmented basalt, whereas higher values (~1000 to ~3000 × 10^{-5} SI) appear to be associated with intervals of coherent basalt. These trends are consistent with GRA bulk density and NGR recordings from the same intervals and generally appear to be the result of poor-quality or absent data. Preliminary observations suggest two exceptions to this trend; relatively rubbly intervals (~7−11 cm basalt fragments) at ~277−279 mbsf and

~286–288 mbsf display higher MS and SRM values. pXRF measurements of Fe do not appear to exceed background levels within this interval, but Ti and K appear to decrease beginning at ~250 mbsf and are lower than average to the bottom of the hole (see **Igneous petrology and volcanology**). Rubbly basalt intervals appear to be associated with drilling disturbance and not individual basalt flows; therefore, we caution against using MS and MSP data (or any single physical properties data set) for detailed correlations in igneous units.

9.5. Sonic velocities

P-wave velocities in the *x*- and *y*-directions for whole-round core sections, the *x*-direction for half sections, and the *x*-, *y*-, and *z*-directions for discrete cubes are consistent through sedimentary and igneous cores recovered from Site U1575.

WRMSL and Section Half Measurement Gantry (SHMG) *P*-wave measurements are close to mean seawater velocity (1500 m/s; Chen and Millero, 1977) in the calcareous ooze, which has a mean value of 1585 ± 29.1 m/s. Between the seafloor and ~206 mbsf, WRMSL *P*-wave measurements, SHMG caliper values, and discrete samples fall within a relatively narrow range (1510–1751 m/s). In the chalk below this interval, at ~206 mbsf, *P*-wave velocity appears to decrease slightly to ~1607 m/s before increasing to ~2600 to ~3200 m/s in the basalt below.

From seafloor to ~194 mbsf, the upper calcareous ooze has a mean *x*- and *y*-axis *P*-wave velocity of ~1586 ± 29 m/s. In the chalk interval, from ~194 to ~210 mbsf, *x*-axis *P*-wave velocity values range 1461–1607 m/s with a mean of ~1534 m/s. Discrete basalt samples below ~210 mbsf to the bottom of the hole show the highest *P*-wave velocities, ranging ~2663 to ~3177 m/s with a mean of ~2937 ± 37.9 m/s. Higher *P*-wave velocities appear to correlate well with lower porosities and higher bulk densities in massive and sheet basalt flows (Figure **F37**).

9.6. Natural gamma radiation

NGR measurements are summarized in plots of total counts per second versus depth (Figure **F37**). NGR recordings are dependent on lithologic characteristics such as composition and porosity. Consequently, highly fragmented and vesicular material results in lower NGR counts than more massive crystalline material, and wide-ranging NGR values are associated with intervals of low and fragmented material (de Ronde et al., 2019). To avoid spurious correlations, NGR values are compared in intervals with high recovery that contain coherent pieces with lengths >20 cm.

NGR recordings also reveal stratigraphic details that can aid in lithologic and geochemical correlations. Higher potassium concentrations in clay- or ash-rich sediments in drilled core yield significantly higher NGR counts, and high NGR counts have been correlated to relatively high potassium concentrations (K_2O = >1.8 wt%) in Snake River Plain basalts (Potter et al., 2019). In Hole U1575A, an interval of low NGR and accompanying high MS at 277–279 mbsf appears to correlate with the beginning of a relatively low-TiO_2 (1.6–2 wt% versus ~3 wt%) basalt flow identified using pXRF data (see **Igneous petrology and volcanology**).

At the calcareous ooze/chalk contact at ~194 mbsf, mean NGR values increase from 3.33 ± 1.31 counts/s to 16.0 ± 0.867 counts/s. Across the chalk/igneous basement interface at ~210 mbsf, mean NGR values decrease slightly to 15.4 ± 0.242 counts/s. The sediment units in Hole U1575A yield mean NGR values of 2.60 ± 0.34 counts/s (calcareous ooze) and 4.51 ± 1.06 counts/s (chalk).

9.7. Rheology

Sediment shear strength was measured with the automated vane shear (AVS) system on soft-sediment cores recovered from Hole U1575A. The interval of soft sediment extends from the seafloor to 185 mbsf. AVS measurements were not taken below this depth because of the increasing lithification of sediments. AVS increases from 0.466 to 10.3 kN/m^2 in the soft-sediment interval, which is consistent with increasing density and compaction at greater depths.

9.8. Data integration and lithology correlation

Physical properties measurements closely align with the depths of the three stratigraphic subdivisions at Site U1575: calcareous ooze, chalk, and basalt. The calcareous ooze/chalk and chalk/basalt contacts are recorded as sharp increases in *P*-wave velocity, MS, and bulk density (WRMSL and MAD); as more gradual increases in thermal conductivity and *P*-wave velocity with depth; and as abrupt decreases in porosity. The basalt unit uniformly displays the highest values of *P*-wave velocity, MS, bulk density (WRMSL and MAD), and thermal conductivity, and it displays the lowest porosity. In particular, measurements of NGR, GRA bulk density, and MS record both rubbly and coherent intervals and appear to broadly correlate to basalt flow boundaries (Figure **F37**). Most notably, these data also align with pXRF analyses and demonstrate the presence of chemically anomalous (e.g., low TiO_2, K, and Zr) basalts in Hole U1575A between ~270 and ~315 mbsf.

References

Acton, G.D., Okada, M., Clement, B.M., Lund, S.P., and Williams, T., 2002. Paleomagnetic overprints in ocean sediment cores and their relationship to shear deformation caused by piston coring. Journal of Geophysical Research: Solid Earth, 107:2067–2081. **https://doi.org/10.1029/2001JB000518**

Baker, P.A., Gieskes, J.M., and Elderfield, H., 1982. Diagenesis of carbonates in deep-sea sediments; evidence from Sr/Ca ratios and interstitial dissolved Sr (super 2+) data. Journal of Sedimentary Research, 52(1):71–82. **https://doi.org/10.1306/212F7EE1-2B24-11D7-8648000102C1865D**

Baudin, F., Martinez, P., Dennielou, B., Charlier, K., Marsset, T., Droz, L., and Rabouille, C., 2017. Organic carbon accumulation in modern sediments of the Angola Basin influenced by the Congo deep-sea fan. Deep Sea Research Part II: Topical Studies in Oceanography, 142:64-74. **https://doi.org/10.1016/j.dsr2.2017.01.009**

Chave, A.D., 1984. Lower Paleocene-Upper Cretaceous magnetostratigraphy, Sites 525, 527, 528, and 529, Deep Sea Drilling Project Leg 74. In Moore, T.C., Jr., Rabinowitz, P.D., et al., Initial Reports of the Deep Sea Drilling Project, 74: Washington, DC (US Government Printing Office), 525–531. **https://doi.org/10.2973/dsdp.proc.74.110.1984**

Chen, C.T., and Millero, F.J., 1977. Speed of sound in seawater at high pressures. The Journal of the Acoustical Society of America, 62(5):1129–1135. **https://doi.org/10.1121/1.381646**

Class, C., and Lehnert, K., 2012. PetDB Expert MORB (Mid-Ocean Ridge Basalt) Compilation, Version 1.0. Interdisciplinary Earth Data Alliance (IEDA). **https://doi.org/10.1594/IEDA/100060**

Class, C., and le Roex, A.P., 2008. Ce anomalies in Gough Island lavas — trace element characteristics of a recycled sediment component. Earth and Planetary Science Letters, 265(3):475-486. **https://doi.org/10.1016/j.epsl.2007.10.030**

Cliff, R.A., Baker, P.E., and Mateer, N.J., 1991. Geochemistry of inaccessible island volcanics. Chemical Geology, 92(4):251–260. **https://doi.org/10.1016/0009-2541(91)90073-Z**

de Ronde, C.E.J., Humphris, S.E., Höfig, T.W., Brandl, P.A., Cai, L., Cai, Y., Caratori Tontini, F., Deans, J.R., Farough, A., Jamieson, J.W., Kolandaivelu, K.P., Kutovaya, A., Labonté, J.M., Martin, A.J., Massiot, C., McDermott, J.M., McIntosh, I.M., Nozaki, T., Pellizari, V.H., Reyes, A.G., Roberts, S., Rouxel, O., Schlicht, L.E.M., Seo, J.H., Straub, S.M., Strehlow, K., Takai, K., Tanner, D., Tepley III, F.J., and Zhang, C., 2019. Expedition 376 methods. In de Ronde, C.E.J., Humphris, S.E., Höfig, T.W., and the Expedition 376 Scientists, Brothers Arc Flux. Proceedings of the International Ocean Discovery Program, 376: College Station, TX (International Ocean Discovery Program). **https://doi.org/10.14379/iodp.proc.376.102.2019**

Doubrovine, P.V., Steinberger, B., and Torsvik, T.H., 2012. Absolute plate motions in a reference frame defined by moving hot spots in the Pacific, Atlantic, and Indian oceans. Journal of Geophysical Research: Solid Earth, 117(B9):B09101. **https://doi.org/10.1029/2011JB009072**

Ernesto, M., Pacca, I.G., Hiodo, F.Y., and Nardy, A.J.R., 1990. Palaeomagnetism of the Mesozoic Serra Geral Formation, southern Brazil. Physics of the Earth and Planetary Interiors, 64(2):153–175. **https://doi.org/10.1016/0031-9201(90)90035-V**

Ernesto, M., Raposo, M.I.B., Marques, L.S., Renne, P.R., Diogo, L.A., and de Min, A., 1999. Paleomagnetism, geochemistry and $^{40}Ar/^{39}Ar$ dating of the north-eastern Paraná Magmatic Province: tectonic implications. Journal of Geodynamics, 28(4):321–340. **https://doi.org/10.1016/S0264-3707(99)00013-7**

Gibson, S.A., Thompson, R.N., Day, J.A., Humphris, S.E., and Dickin, A.P., 2005. Melt-generation processes associated with the Tristan mantle plume: constraints on the origin of EM-1. Earth and Planetary Science Letters, 237(3–4):744–767. **https://doi.org/10.1016/j.epsl.2005.06.015**

Gieskes, J.M., 1981. Deep-sea drilling interstitial water studies: implications for chemical alteration of the oceanic crust, Layers I and II. In Warme, J.E., Douglas, R.G., and Winterer, E.L. (Eds.), Deep Sea Drilling Project: A Decade of Progress. Special Publication - SEPM (Society for Sedimentary Geology), 32: 149–168.

Gradstein, F.M., Ogg, J.G., Schmitz, M.D., and Ogg, G.M. (Eds.), 2020. The Geologic Time Scale 2020: Amsterdam (Elsevier BV). **https://doi.org/10.1016/C2020-1-02369-3**

Hoernle, K., Rohde, J., Hauff, F., Garbe-Schönberg, D., Homrighausen, S., Werner, R., and Morgan, J.P., 2015. How and when plume zonation appeared during the 132 Myr evolution of the Tristan Hotspot. Nature Communications, 6(1):7799. **https://doi.org/10.1038/ncomms8799**

Homrighausen, S., Hoernle, K., Geldmacher, J., Wartho, J.A., Hauff, F., Portnyagin, M., Werner, R., van den Bogaard, P., and Garbe-Schönberg, D., 2018. Unexpected HIMU-type late-stage volcanism on the Walvis Ridge. Earth and Planetary Science Letters, 492:251–263. **https://doi.org/10.1016/j.epsl.2018.03.049**

Homrighausen, S., Hoernle, K., Hauff, F., Wartho, J.A., van den Bogaard, P., and Garbe-Schönberg, D., 2019. New age and geochemical data from the Walvis Ridge: the temporal and spatial diversity of South Atlantic intraplate volcanism and its possible origin. Geochimica et Cosmochimica Acta, 245:16–34. **https://doi.org/10.1016/j.gca.2018.09.002**

Homrighausen, S., Hoernle, K., Zhou, H., Geldmacher, J., Wartho, J.-A., Hauff, F., Werner, R., Jung, S., and Morgan, J.P., 2020. Paired EMI-HIMU hotspots in the South Atlantic—starting plume heads trigger compositionally distinct secondary plumes? Science Advances, 6(28):eaba0282. **https://doi.org/10.1126/sciadv.aba0282**

Inoue, H., Coffin, M.F., Nakamura, Y., Mochizuki, K., and Kroenke, L.W., 2008. Intrabasement reflections of the Ontong Java Plateau: implications for plateau construction. Geochemistry, Geophysics, Geosystems, 9(4):Q0401. **https://doi.org/10.1029/2007GC001780**

Jackson, M., Gruber, W., Marvin, J., and Banerjee, S.K., 1988. Partial anhysteretic remanence and its anisotropy: applications and grainsize-dependence. Geophysical Research Letters, 15(5):440–443. **https://doi.org/10.1029/GL015i005p00440**

Jochum, K.P., and Verma, S.P., 1996. Extreme enrichment of Sb, Tl and other trace elements in altered MORB. Chemical Geology, 130(3–4):289–299. **https://doi.org/10.1016/0009-2541(96)00014-9**

Le Bas, M.J., Le Maitre, R. W., Streickeisen, A., Zanettin, B., the IUGS Subcommission on the Systematics of Igneous Rocks, 1986. A chemical classification of volcanic rocks based on the total alkali-silica diagram. Journal of Petrology, 27(3):745–750. **https://doi.org/10.1093/petrology/27.3.745**

Le Maitre, R.W., 1962. Petrology of volcanic rocks, Gough Island, South Atlantic. Geological Society of America Bulletin, 73(11):1309–1340. **https://doi.org/10.1130/0016-7606(1962)73[1309:POVRGI]2.0.CO;2**

Le Roex, A.P., Cliff, R.A., and Adair, B.J.I., 1990. Tristan da Cunha, South Atlantic: geochemistry and petrogenesis of a basanite-phonolite lava series. Journal of Petrology, 31(4):779–812. **https://doi.org/10.1093/petrology/31.4.779**

MacDonald, G.A., and Katsura, T., 1964. Chemical composition of Hawaiian lavas. Journal of Petrology, 5(1):82–133. **https://doi.org/10.1093/petrology/5.1.82**

McFadden, P.L., and Reid, A.B., 1982. Analysis of palaeomagnetic inclination data. Geophysical Journal International, 69(2):307–319. **https://doi.org/10.1111/j.1365-246X.1982.tb04950.x**

O'Connor, J.M., and le Roex, A.P., 1992. South Atlantic hot spot-plume systems: 1. Distribution of volcanism in time and space. Earth and Planetary Science Letters, 113(3):343–364. **https://doi.org/10.1016/0012-821X(92)90138-L**

Potter, K.E., Champion, D.E., Duncan, R.A., and Shervais, J.W., 2019. Volcanic stratigraphy and age model of the Kimama deep borehole (Project Hotspot): evidence for 5.8 million years of continuous basalt volcanism, central Snake River Plain, Idaho. Geosphere, 15(3):736–758. **https://doi.org/10.1130/GES01679.1**

Quinby-Hunt, M.S., and Turekian, K.K., 1983. Distribution of elements in sea water. Eos, Transactions of the American Geophysical Union, 64(14):130. **https://doi.org/10.1029/EO064i014p00130**

Renne, P.R., Scott, G.R., Glen, J.M.G., and Feinberg, J.M., 2002. Oriented inclusions of magnetite in clinopyroxene: source of stable remanent magnetization in gabbros of the Messum Complex, Namibia. Geochemistry, Geophysics, Geosystems, 3(12):1–11. **https://doi.org/10.1029/2002GC000319**

Richardson, S.H., Erlank, A.J., Reid, D.L., and Duncan, A.R., 1984. Major and trace element and Nd and Sr isotope geochemistry of basalts from the Deep Sea Drilling Project Leg 74 Walvis Ridge transect. In Moore, T.C., Jr., Rabinowitz, P. D., et al., Initial Reports of the Deep Sea Drilling Project, 74: Washington, DC (US Government Printing Office), 739–754. **https://doi.org/10.2973/dsdp.proc.74.125.1984**

Rohde, J., Hoernle, K., Hauff, F., Werner, R., O'Connor, J., Class, C., Garbe-Schönberg, D., and Jokat, W., 2013. 70 Ma chemical zonation of the Tristan-Gough hotspot track. Geology, 41(3):335–338. **https://doi.org/10.1130/G33790.1**

Sager, W., Hoernle, K., Höfig, T.W., Avery, A.J., Bhutani, R., Buchs, D.M., Carvallo, C.A., Class, C., Dai, Y., Dalla Valle, G., Del Gaudio, A.V., Fielding, S., Gaastra, K.M., Han, S., Homrighausen, S., Kubota, Y., Li, C.-F., Nelson, W.R., Petrou, E., Potter, K.E., Pujatti, S., Scholpp, J., Shervais, J.W., Thoram, S., Tikoo-Schantz, S.M., Tshiningayamwe, M., Wang, X.-J., and Widdowson, M., 2023. Expedition 391 methods. In Sager, W., Hoernle, K., Höfig, T.W., Blum, P., and the Expedition 391 Scientists, Walvis Ridge Hotspot. Proceedings of the International Ocean Discovery Program, 391: College Station, TX (International Ocean Discovery Program). **https://doi.org/10.14379/iodp.proc.391.102.2023**

Sager, W.W., Zhang, J., Korenaga, J., Sano, T., Koppers, A.A.P., Widdowson, M., and Mahoney, J.J., 2013. An immense shield volcano within the Shatsky Rise oceanic plateau, northwest Pacific Ocean. Nature Geoscience, 6(11):976–981. **https://doi.org/10.1038/ngeo1934**

Salters, V.J.M., and Sachi-Kocher, A., 2010. An ancient metasomatic source for the Walvis Ridge basalts. Chemical Geology, 273(3–4):151–167. **https://doi.org/10.1016/j.chemgeo.2010.02.010**

Shaar, R., and Feinberg, J.M., 2013. Rock magnetic properties of dendrites: insights from MFM imaging and implications for paleomagnetic studies. Geochemistry, Geophysics, Geosystems, 14(2):407–421. **https://doi.org/10.1002/ggge.20053**

Shervais, J.W., 2022. The petrogenesis of modern and ophiolitic lavas reconsidered: Ti-V and Nb-Th. Geoscience Frontiers, 13(2):101319. **https://doi.org/10.1016/j.gsf.2021.101319**

Smith, W.H.F., and Sandwell, D.T., 1997. Global sea floor topography from satellite altimetry and ship depth soundings. Science, 277(5334):1956–1962. **https://doi.org/10.1126/science.277.5334.1956**

Summerhayes, C.P., Kroon, D., Rosell-Melé, A., Jordan, R.W., Schrader, H.J., Hearn, R., Villanueva, J., Grimalt, J.O., and Eglinton, G., 1995. Variability in the Benguela Current upwelling system over the past 70,000 years. Progress in Oceanography, 35(3):207–251. **https://doi.org/10.1016/0079-6611(95)00008-5**

Torsvik, T.H., Müller, R.D., Van der Voo, R., Steinberger, B., and Gaina, C., 2008. Global plate motion frames: toward a unified model. Reviews of Geophysics, 46(3):RG3004. **https://doi.org/10.1029/2007RG000227**

Tozer, B., Sandwell, D.T., Smith, W.H.F., Olson, C., Beale, J.R., and Wessel, P., 2019. Global bathymetry and topography at 15 arc sec: SRTM15+. Earth and Space Science, 6(10):1847–1864. **https://doi.org/10.1029/2019EA000658**

Van Fossen, M.C., and Kent, D.V., 1992. Paleomagnetism of 122 Ma plutons in New England and the mid-Cretaceous paleomagnetic field in North America: true polar wander or large-scale differential mantle motion? Journal of Geophysical Research: Solid Earth, 97(B13):19651–19661. **https://doi.org/10.1029/92JB01466**

Verosub, K.L., 1977. Depositional and postdepositional processes in the magnetization of sediments. Reviews of Geophysics, 15(2):129–143. **https://doi.org/10.1029/RG015i002p00129**

Wade, B.S., Pearson, P.N., Olsson, R.K., Fraass, A.J., Leckie, R.M., and Hemleben, C., 2018. Taxonomy, biostratigraphy, and phylogeny of Oligocene and lower Miocene Dentoglobigerina and Globoquadrina. In Wade, B.S., Olsson, R.K., Pearson, P.N., Huber, B.T., and Berggren, W.A. (Eds.), Atlas of Oligocene Planktonic Foraminifera. Cushman Foundation Special Publication, 46: 331–384.
https://www.ucl.ac.uk/earth-sciences/sites/earth-sciences/files/Chapter_11.pdf

Weaver, B.L., Wood, D.A., Tarney, J., and Joron, J.L., 1987. Geochemistry of ocean island basalts from the South Atlantic: Ascension, Bouvet, St. Helena, Gough and Tristan da Cunha. In Fitton, J.G., and Upton, B.G.J. (Eds.), Alkaline Igneous Rocks. Geological Society Special Publication, 30:253–267.
https://doi.org/10.1144/GSL.SP.1987.030.01.11

Wei, K.-Y., 1994. Stratophenetic tracing of phylogeny using SIMCA pattern recognition technique: a case study of the late Neogene planktonic foraminifera Globoconella clade. Paleobiology, 20(1):52–65.
https://www.jstor.org/stable/2401150

Willbold, M., and Stracke, A., 2006. Trace element composition of mantle end-members: implications for recycling of oceanic and upper and lower continental crust. Geochemistry, Geophysics, Geosystems, 7(4):Q04004.
https://doi.org/10.1029/2005GC001005

Zhou, H., Hoernle, K., Geldmacher, J., Hauff, F., Homrighausen, S., Garbe-Schönberg, D., and Jung, S., 2020. Geochemistry of Etendeka magmatism: spatial heterogeneity in the Tristan-Gough plume head. Earth and Planetary Science Letters, 535:116123. **https://doi.org/10.1016/j.epsl.2020.116123**

Zindler, A., and Hart, S., 1986. Chemical geodynamics. Annual Review of Earth and Planetary Sciences, 14:493–570.
https://doi.org/10.1146/annurev.ea.14.050186.002425